Measurement of the Multi-pion neutrino interaction cross section with the K2K Scintillating-bars detector

PhD on Physics

by

Gabriel Vicent Jover Mañas

supervised by

Federico Sánchez Nieto

IFAE
Universitat Autònoma de Barcelona
Barcelona (Spain)
July, 2008

Gabriel Vicent Jover Mañas
IFAE
Universitat Autònoma de Barcelona
E-08291 Ripollet (BARCELONA)
gabrielj@IFAE.es

Contents

Chapter 1

Overview

One of the most exciting discoveries in the last years on particle physics has been the discovery of neutrino oscillation. This discovery has promoted several experiments to measure with high precision the neutrino oscillation parameters.

For that purpose a good knowledge of neutrino-nucleus interactions is crucial and this is the main motivation of this study. The measurement of neutrino interaction cross sections in the neutrino energy regime of a few GeV is complicated since in that region the interaction processes are so similar that they overlap on kinematic observables.

In this dissertation a method to measure the multi-pion cross section with the K2K experiment data will be explained and the results of the measurement will be presented. The measurement is based on likelihood distributions that are used to fit MC to data and extract the multi-pion contribution to the inclusive cross section.

In chapter 2 an introduction to neutrino oscillation is presented as well as the motivation on doing neutrino cross section measurements.
In chapter 3 the K2K experiment is described. The setup of the different detectors and the experimental technique to measure neutrino oscillations is presented. Then, chapter 4 describes the Scintillating-bars detector (SciBar) and the tracking method in detail and chapter 5 the different steps of the simulation.

In chapter 6 the method to measure multi-pion relative cross sections with the SciBar data is explained. The data selection is described and the different observables are introduced. Then the method to construct the multi-pion likelihood is described an its behaviour is evaluated. It is explained how the MC likelihood distributions are fitted to data and how the fit information is used to get the measurement of multi-pion relative cross section.

In chapter 7 the source of systematic effects in the measurement is discussed and the calculation of the systematic errors is presented. In chapter 8 we show and discuss

the final result of the measurement. Finally, in chapter 8 conclusions of this work are drawn.

Chapter 2

Introduction to neutrinos

2.1 Historical Introduction

In the years 1911 to 1914, scientists exploring the new field of nuclear physics were confronted with a troubling mystery. Measurements of the ^{210}Bi (Ra E) beta decay showed a continuous spectrum instead of the well defined energy that folds from energy conservation in a two body reaction. Had the scientists to throw away the sacred energy conservation law? Some dared to believe it.

In the twenties the study of nucleus composition pointed to the existence of a new neutral particles. Motivated by the idea of a new particle, Pauli tried to combine this problem with the problem of the continuous beta spectrum. The 4th December 1930 he wrote his famous letter proposing the existence of a rare particle that would solve the beta decay problem ([Win91] p. 4) :

> Dear Radioactive Ladies and Gentlemen,
>
> As the bearer of these lines, to whom I graciously ask you to listen, will explain to you in more detail, how because of the "wrong" statistics of the N and ^{6}Li nuclei and the continuous β-spectrum, I have hit upon a desperate remedy to save the "exchange theorem" of statistics and the law of conservation of energy. Namely, the possibility that there could exist in the nuclei electrically neutral particles, that I wish to call neutrons, which have spin 1/2 and obey the exclusion principle and which further differ from light quanta in that they do not travel with the velocity of light. The mass of the neutrons should be of the same order of magnitude as the electron mass and in any event not larger than 0.01 proton masses. – The continuous β-spectrum would then become understandable by the assumption that in β-decay, a neutron is emitted in addition to the electron such that the sum of the energies of the neutron and electron is constant. ...
>
> For the moment, however, I do not dare to publish anything on this idea and I put to you, dear Radioactives, the question of what the situation

would be if one such neutron were detected experimentally, if it would have a penetrating power similar to, or about 10 times larger than, a γ-ray.

I admit that on a first look my way out might seem to be unlikely, since one would certainly have seen the neutrons by now if they existed. But nothing ventured nothing gained, and the seriousness of the matter with the continuous β-spectrum is illustrated by a quotation of my honored predecessor in office, Mr Debye, who told me recently in Brussels: "Oh, It is best not to think about it, like the new taxes." Therefore one should earnestly discuss each way of salvation. – So, dear Radiactives, examine and judge it. – Unfortunately I cannot appear in Tübingen personally, since I am indispensable here in Zürich because of a ball on the night of 6/7 December. – With my best regards to you, and also to Mr. Back, your humble servant,

W. Pauli

A neutral particle was discovered in 1932 by Chadwick with one proton mass, the neutron, but it was too heavy to be the Pauli's particle.

In 1933 Fermi reported on his theory of β-decay based on the neutral particle postulated by Pauli. This particle was called *neutrino* by Fermi, to distinguish it from the neutron. He also presented some conclusions on the beta spectrum. One of the conclusion was that, based on the β-decay tail shape, the neutrino mass was compatible with 0. As a matter of fact, the best upper limit on neutrino mass we have nowadays is based on the ${}^3_1H$ β-decay spectrum [K$^+$05].

Despite of the success of Fermi's neutrino theory to explain the β-decay, part of the scientific community was not convinced on the validity of this theory since the neutrino was not been detected.

From 1939 to 1945, the second world war made nuclear physicist to focus on nuclear reactions. Scientists throughout the world began to study reaction chains and self-sustaining chain reactions. In these reaction chains, many β-decaying elements are produced, becoming a good source of neutrinos. However these investigations were secret and the access to the investigation areas restricted.

Finally, in 1956 F. Reines and C. L. Cowan, Jr. presented a clear direct detection of the neutrino [CRH$^+$56, RC59]. They where allowed to place their experiment near the fission reactor at the Savannah River Plant (South California). The experiment consisted out of a sandwich arrangement of tree scintillation counters and two target tanks (Fig. 2.1). The scintillation counter were a tank filled with liquid scintillator and read with 110 photomultipliers each. The target was a water dissolution of $CdCl_2$. When a neutrino interacts with a proton in the target tank, a positron and a neutron are produced. The photon pair produced by the positron annihilation were measured by the counters next to the target tank. In less than 25 μs, the dissolved cadmium

capture the neutron also producing photons. To identify the neutrino signal, they expected that they will get a coincidence signal of the positron and the neutron within a precise time window, energy window and in anti-coincidence with the third counter. They toke a lot of care to reduce the cosmic ray background. As a result they got the first clear direct detection of the neutrino, and they even measured a neutrino cross section of $6.3 \times 10^{-44} cm^2 \pm 25\%$ [CRH$^+$56].

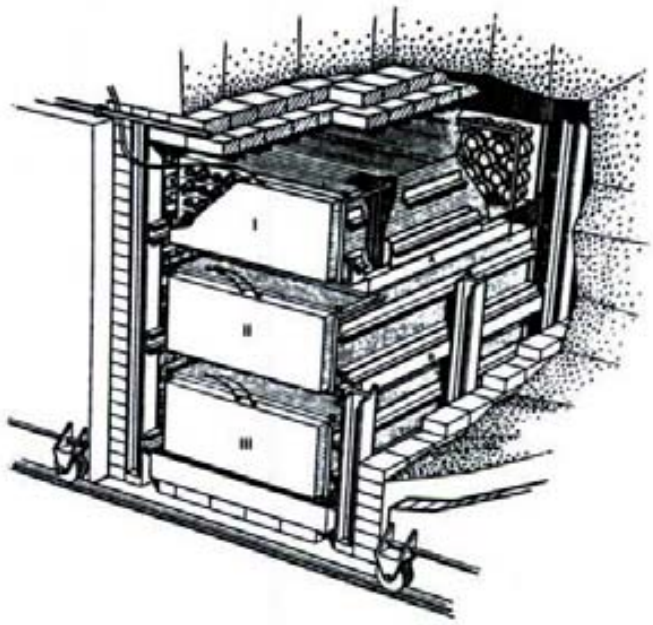

Figure 2.1: Concept picture of the Reines and Cowan detector. The big boxes I, II and III are the scintillation counters and the two small boxes A and B between the counters are the target tanks.

This discovery solved the beta decay problem and open many questions on the neutrino. In beta decay the neutrino is emitted together with an electron, but is it emitted in weak interactions that involve other lepton as the muon? is the same neutrino or has one to identify them as electron neutrino and muon neutrino?

In 1962 the muon neutrino was discovered at the Brookhaven AGS[1] [D$^+$62]. This was the first experiment done with neutrinos from an accelerator. Neutrinos were produced in the decays of pions produced in interactions of 15 GeV protons with a beryllium target. Charged particles were absorbed in 13.5 m iron shield. After the shield a spark chamber detector was constructed (Fig. 2.2). When the neutrino interacts producing a particle, this particle flight through the chamber ionizing the gas on its path. Then

[1] Alternating Gradient Synchrotron

the layer, loaded with high voltage, produce sparks on the ionized gas, showing the particle path.

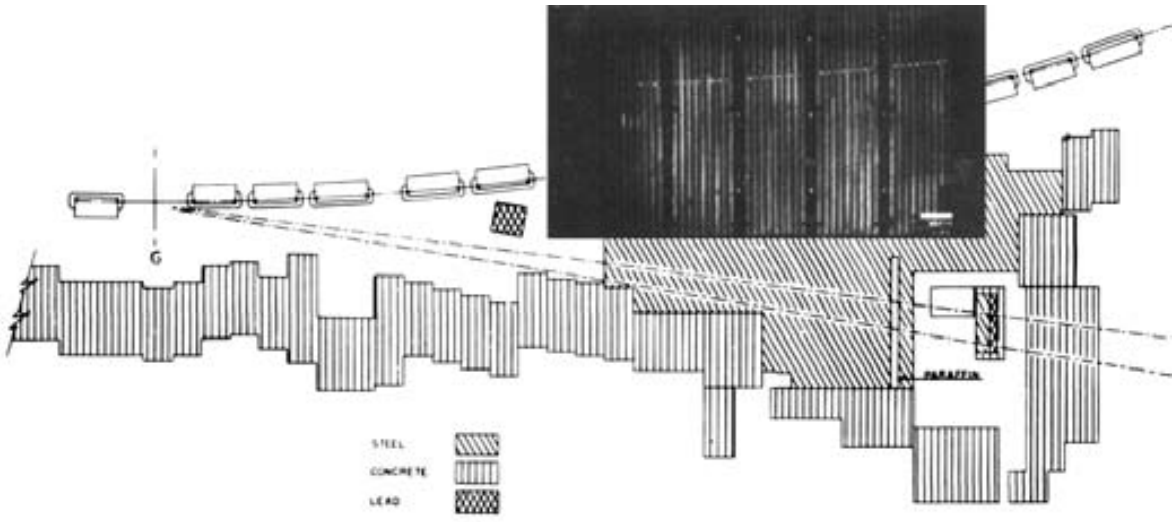

Figure 2.2: Plan view of the AGS neutrino experiment and a muon event in the spark chamber detector.

If ν_μ and ν_e were thought to be the same particles then about the same amount of muons and electrons should have appeared in the detector, since they would interact in the same way. But they observed 29 muons and only 6 electrons candidates that could be explained as background events. It was proved that the process $\nu_\mu + N \rightarrow e^- + X$ is forbidden and that muon and electron neutrinos are different particles.

At that time the study of nuclear reactions that produce the sun energy was quite detailed. This was explained with the CNO cycle, an exothermic chain of nuclear reactions that capture protons and produce helium, photons, positrons and neutrinos.

To check the model a measurement of the solar neutrino flux was proposed and in 1968 Raymond Davis published the first measurement of solar neutrino flux [DHH68]. The detector was made of 520 tons of liquid C_2Cl_4 in a horizontal cylindrical tank located in an 1480 m underground laboratory to reduce cosmic ray background. The detection is based on the interaction $\nu + {}^{37}Cl \rightarrow e^- + {}^{37}Ar$. This argon isotope is radioactive, so one can measure the amount of argon by detecting it's decay. The measurement show a deficit in the number of neutrinos that the sun was expected to emit. This was called the solar neutrino problem. Is our particle physics theory wrong? Is our model of the solar interior wrong? Is it just because an experimental error?

In the following year, Gribov and Pontecorvo published how $\nu_e \leftrightarrow \nu_\mu$ may oscillate and its relation with a decrease in the number of detectable solar neutrinos at the earth surface [GP69]. An electron neutrino could spontaneously change into a muon neutrino

and, since the solar neutrino detector was not designed to detect muon neutrinos, the deficit could be explained taking into account electron neutrino disappearance. This new effect pointed to the need of new neutrino detectors to measure the solar neutrino deficit and oscillation. But one had to wait many years until the neutrino oscillation parameters were measured.

Before that, in the seventies and eighties numerous experiments and breakthroughs about quarks and leptons, came one after an other. The three family of quarks where discovered as well as the tau lepton. Different neutrino cross sections where measured. And the weak interaction bosons (W,Z) were discovered. The first measurement of the Z boson at CERN in 1989 showed that the number of neutrinos with a mass lower than half the Z mass is be 3.27 ± 0.30 [D$^+$89]. All this point to the existence of the tau neutrino.

In the eighties also started the construction of big underground detectors like IMB and Kamiokande designed to measure the proton decay and to be used as neutrino observatories.

Kamiokande is an underground experiment consisting of a 3 kiloton pure water tank that measure the Čerenkov radiation produced by the charged particles from neutrino interactions. This allows to get neutrino direction and energy and to distinguish electron and muon neutrino interactions.

In 1988 the Kamiokande collaboration published the result for atmospheric neutrinos [H$^+$88]. When a high energetic particle interacts with the atmosphere it may produce pions. Pions decay to muon and muons to electrons, producing muon and electron neutrinos. They measured that only $59 \pm 7\%$ of the expected muon neutrinos reach the detector. In 1989 they published the result for solar neutrino [H$^+$89] that confirmed that solar neutrinos actually come from the sun and only $46 \pm 15(stat.) \pm 8(sys.)\%$ reach the detector.

In 1990 began the excavation for a new detector in Canada, SNO[2] and in 1991 the excavation for SuperKamiokande (SK).

SK is a water Čerenkov detector like Kamiokande but with 50 kilotons of water. This huge detector is also used in the K2K experiment and will be described in section 3.1. One of its purposes was to observe the atmospheric neutrino disappearance and in 1998 the result was published [F$^+$98]. SK showed a zenith angle dependence on the amount of ν_μ atmospheric neutrinos that could not be explained by detector systematic effects but assuming neutrino oscillation. The measurement was a clear evidence for $\nu_\mu \rightarrow \nu_\tau$ oscillation and they also calculated the neutrino oscillation parameters.

The SNO detector was turned on in 1999. It consists of one kiloton of heavy water contained in an spherical acrylic vessel of 6 m in diameter. The heavy water is

[2]Sudbury Neutrino Observatory

shielded with pure water in a 8.5 m spherical vessel. The walls are equipped with 9438 photo-multiplier tubes (PMT) (Fig. 2.3). The PMTs measure the Čerenkov light from charged leptons produced in neutrino interactions and the gamma radiation produced by neutron absorption in ^2H. These two methods can measure the ν_e exclusive interaction $\nu_e + d \rightarrow e^- + p + p$ and the ν_x inclusive interactions $\nu_x + e^- \rightarrow \nu_x + e^-$ and $\nu_x + d \rightarrow \nu_x + n + p$. This measurement was crucial since it was able to measure the total neutrino flux from the sun and the fraction of electron neutrino, instead of just to measure a ν_e deficit that may be due to a problem in the standard solar model. In 2002 they published their result showing that the total neutrino flux coming from the sun is compatible with the solar standard model and the electron neutrino flux coming from the sun is only 1/3, providing an strong evidence of neutrino oscillation [A$^+$02]. After this phase of the experiment, SNO measured these interactions improving the neutron capture by doping the heavy water with $MgCl_2$ [A$^+$04a] and in the next phase they used ^3He proportional counter tubes hanging in a grid within the pure heavy water [Bro99].

In 1999 also started the K2K experiment which measured the $\nu_\mu \rightarrow \nu_\tau$ oscillation parameters. But this will be explained in next chapter.

2.2 Neutrino oscillations theory

The three neutrinos flavours are electronic, muonic, and tauonic. Based on quantum mechanical principles, if neutrinos have a nonzero mass and the mass eigenstates do not correspond to the flavor eigenstates, neutrinos can mix. This is analogous to the mixing in the quark sector. The flavor states $|\nu_\alpha\rangle$ can be writed in terms of the mass states $|\nu_i\rangle$ as

$$|\nu_\alpha\rangle = \sum_i \mathbb{U}^*_{\alpha i} |\nu_i\rangle \tag{2.1}$$

where $\alpha = e, \mu, \tau$, $i = 1, 2, 3$ and $\mathbb{U}_{\alpha i}$ is a unitary mixing matrix. Let's assume that a neutrino ν_α is produced by a weak interaction in a flavor eigenstate. To understand how the state evolves in time, we apply the time dependent Schrödinger equation to each ν_i component of ν_α in the rest frame of that component. This gives us

$$|\nu_i(\tau_i)\rangle = e^{-im_i\tau_i} |\nu_i(0)\rangle \tag{2.2}$$

where m_i is the mass of ν_i, τ_i is the time in the ν_i rest frame and natural units ($\hbar = c = 1$) are used. The phase factor is Lorentz-invariant and thus may be written in terms of laboratory frame time t and position L,

$$|\nu_i(t, L)\rangle = e^{-i(E_i t - p_i L)} |\nu_i\rangle \tag{2.3}$$

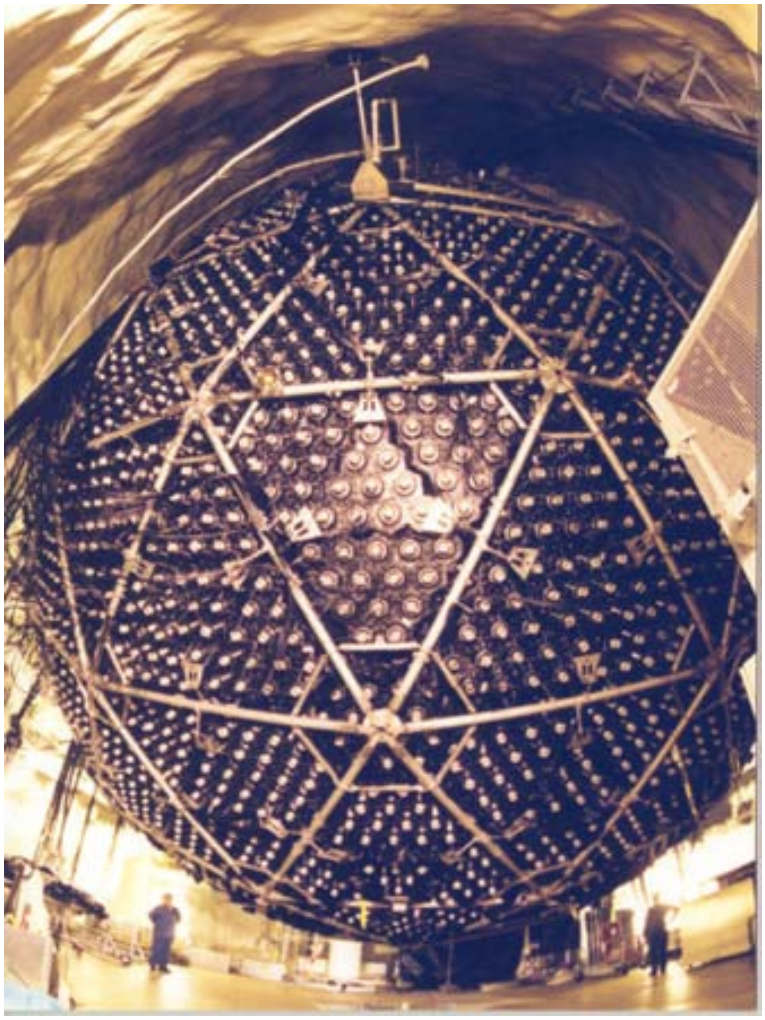

Figure 2.3: Picture of the SNO detector.

where E_i and p_i are the energy and momentum of ν_i in the laboratory frame. The neutrino is highly relativistic, and therefore we can make the approximation, $t \approx L$, giving

$$|\nu_i(L)\rangle = e^{-i(E_i - p_i)L}|\nu_i\rangle \tag{2.4}$$

Let's assume that ν_α is produced with definite momentum p, so that all of the mass eigenstate components of ν_α have a common momentum, $p_i = p$. Also, we can assume that the neutrino masses m_i are sufficiently small compared with the momentum so that we can make the approximation $E_i = \sqrt{p^2 + m_i^2} \approx p + \frac{m_i^2}{2p}$. Then the equation for ν_i evolution becomes

$$\begin{aligned} |\nu_i(L)\rangle &= e^{-i(p+\frac{m_i^2}{2p}-p)L}|\nu_i\rangle \\ &= e^{-i(\frac{m_i^2}{2p})L}|\nu_i\rangle \end{aligned} \tag{2.5}$$

Finally, let's $E \simeq p$ be the average energy of all the mass eigenstate components of the neutrino.

$$|\nu_i(L)\rangle = e^{-i(\frac{m_i^2 L}{2E})}|\nu_i\rangle \tag{2.6}$$

Thus the evolution of a neutrino born as a ν_α is:

$$\begin{aligned} |\nu_\alpha(L)\rangle &= \sum_i \mathbb{U}^*_{\alpha i}|\nu_i(L)\rangle \\ &= \sum_i \mathbb{U}^*_{\alpha i} e^{-i(\frac{m_i^2 L}{2E})}|\nu_i\rangle \end{aligned} \tag{2.7}$$

If we observe this neutrino at a later time via a weak interaction, what flavor eigenstate will we observe?

The probability of observing a β flavour neutrino when the created α flavour neutrino has flight a distance L is:

$$\begin{aligned} P(\nu_\alpha \to \nu_\beta) &= |\langle \nu_\beta|\nu_\alpha(L)\rangle|^2 \\ &= \left|\sum_i \mathbb{U}^*_{\alpha i} e^{-i(\frac{m_i^2 L}{2E})}\mathbb{U}_{i\beta}\right|^2 \end{aligned} \tag{2.8}$$

In the two-flavor approximation, where we assume there are only two flavor states and two mass states, the mixing matrix $\mathbb{U}$ can be written

$$\mathbb{U} = \begin{pmatrix} \cos\theta & \sin\theta \\ -\sin\theta & \cos\theta \end{pmatrix} \tag{2.9}$$

where the mixing angle θ is the only parameter needed to describe the mixing. In this case, the probability of flavor change becomes

$$P(\nu_\alpha \to \nu_\beta) = \sin^2 2\theta \sin^2 \frac{\Delta m^2 L}{4E} \tag{2.10}$$

For the case of three neutrinos, a common way to write the mixing matrix is

$$\mathbb{U} = \begin{pmatrix} c_{12}c_{13} & s_{12}c_{13} & s_{13}e^{-i\delta} \\ -s_{12}c_{23} - c_{12}s_{23}s_{13}e^{i\delta} & c_{12}c_{23} - s_{12}s_{23}s_{13}e^{i\delta} & s_{23}c_{13} \\ s_{12}s_{23} - c_{12}c_{23}s_{13}e^{i\delta} & -c_{12}s_{23} - s_{12}c_{23}s_{13}e^{i\delta} & c_{23}c_{13} \end{pmatrix} \tag{2.11}$$

where $c_{ij} = \cos\theta_{ij}$ and $s_{ij} = \sin\theta_{ij}$. In this case, there are four parameters to describe the mixing: three mixing angles θ_{12}, θ_{13}, and θ_{23} and a CP-violating phase δ.

The Super-Kamiokande collaboration announced in 1998 the first compelling evidence for oscillations of neutrinos produced in the upper atmosphere [F$^+$98]. The observation of neutrino oscillations has proven indirectly that neutrinos have non-zero mass by showing that Δm^2 is non-zero. The most recent result from Super-Kamiokande for the $\nu_\mu \rightarrow \nu_\tau$ oscillation parameters is $\sin^2 2\theta_{23} > 0.92$ and $1.5 \times 10^{-3} < \Delta m^2_{23} < 3.4 \times 10^{-3}(eV/c^2)^2$ at the 90% confidence level [A$^+$05].

2.3 Motivation for neutrino cross section measurements

These days the study of neutrino oscillation, its nature and properties is a hot topic on particle physics. The knowledge of neutrino cross sections for this and further experiments is very important to understand event rates and identify backgrounds.

For example, in K2K the neutrino spectrum measurement is based on the assumption that the muon measured in the Čerenkov detector comes from a quasi-elastic (QE) interaction. As explained in section 3.2, different neutrino interactions may produce the muon and therefore one has to know in detail their relative cross sections.

For future high precision neutrino experiments it will be very useful to know in detail neutrino-nucleon interactions. For example, the NOνA experimental proposal at Fermilab expect to operate at a mean neutrino energy of about 2 GeV and the T2K experiment has neutrino energy tails at few-GeV that will be a background to the signal. Prior to the result presented in this dissertation, there are only few multi-pion production cross section measurements in the few-GeV neutrino energy region. These measurements were published in the 80's and were made with deuterium bubble chambers. Contribute in the knowledge of these interactions is the main motivation of this study.

Chapter 3

K2K experiment

KEK to Kamioka experiment (K2K) is the first long-baseline neutrino oscillation experiment ever done that uses a neutrino beam. The main purpose of the experiment is to measure the neutrino oscillation in the ν_μ disappearance channel. To do that a neutrino beam is produced at KEK[1] and it's spectrum is measured on site and at the far detector Super-Kamiokande (SK). Comparing both spectrum allows one to infer if the neutrinos oscillate and how.

The K2K data acquisition is divided in two periods: K2K-I from June 1999 until July 2001 and K2K-II from January 2003 until November 2004. In between, on the 12th of November 2001, during the SK refilling, one of the photomultiplier tubes (PMTs) broke down producing a chain reaction of implosions that destroy over half of the detector PMTs. Between both periods the SK PMTs where redistributed as well as other changes took place in the near detector.

Figure 3.1: Map of Japan and an schematic view of K2K experiment placement.

[1]Kō Enerugī Kasokuki Kenkyū Kikō , Tsukuba, Ibaraki Prefecture, Japan

3.1 K2K experimental setup

The ν_μ beam is produced at KEK with a 12 GeV proton synchrotron. The protons hit an aluminium rod producing mainly pions, the pions are focused with two magnetic horns and are left to decay to muons and muon neutrinos in a 200 m long tunnel. Because of the relativistic boost, the ν_μ produced in the decay are focused in the pion direction, pointing to Super-Kamiokande.

The KEK ν_μ spectrum is measured with a set of near detectors, 300 m away from the proton target. The near detector set is composed of a 1 Kton water Čerenkov detector (1KT), a scintillating fibers detector (SciFi), a scintillating bars detector (SciBar) and a muon range detector (MRD). These detectors are described below.

Super-Kamiokande (SK) is a 50 Kton water Čerenkov detector 250 km away from KEK. It is build in a mine near Kamioka, 1000 m below the peak of the mountain Ikeno-yama. This allows to use the mountain as a cosmic ray shield. Some of the ν_μ produced at KEK interacts with nuclei in the SK water producing a muon. Relativistic muons flying at higher velocities than light velocity in water produce Čerenkov light and this light is measured with the photomultiplier detectors in the water tank. The kinematics of the muon is measured from the Čerenkov light reconstructed images and the ν_μ energy is calculated assuming a charged current quasi-elastic (CCQE) process. In this way one measures the KEK ν_μ spectrum after a distance of 250 km.

3.1.1 Neutrino Beam

The primary proton beam is a 12 GeV proton synchrotron (KEK-PS) which provides $\sim 6 \times 10^{12}$ protons per extraction every 2.2 seconds. Each extraction or "spill" lasts 1.1 μs and consists of 9 bunches with 125 ns between them. The protons are are then transported with a 85% efficiency to the target hall pointing to SK. In this path the beam intensity in monitored with current transformers (CT) and the spatial profile with segmented planes ionization chambers (SPIC) (Fig. 3.2). The last CT, just in-front of the target, is used to estimated the total number of protons on target (POT). Figure 3.3 shows the acumulated number of POT from March 1999 to November 2004. In total 104.9×10^{18} POT were delivered until November 2004.

The target is a 66 cm long and 3 cm thick rod made of aluminium alloy 6061-T. It is placed at the central opening of the first horn magnet. Positive pions produced in the rod are focused with the horn magnets pair (Fig. 3.4). The first is 70 cm in diameter and 237 cm log. The second magnet is 10.5 m downstream and is 165 cm in diameter and 276 cm long. Both are supplied with pulsed current of 250 kA intensity and 2 ms duration, every 2.2 second and synchronized with the proton extraction. The maximum magnetic field in the magnets is 33 kG at the surface of the target. Detailed

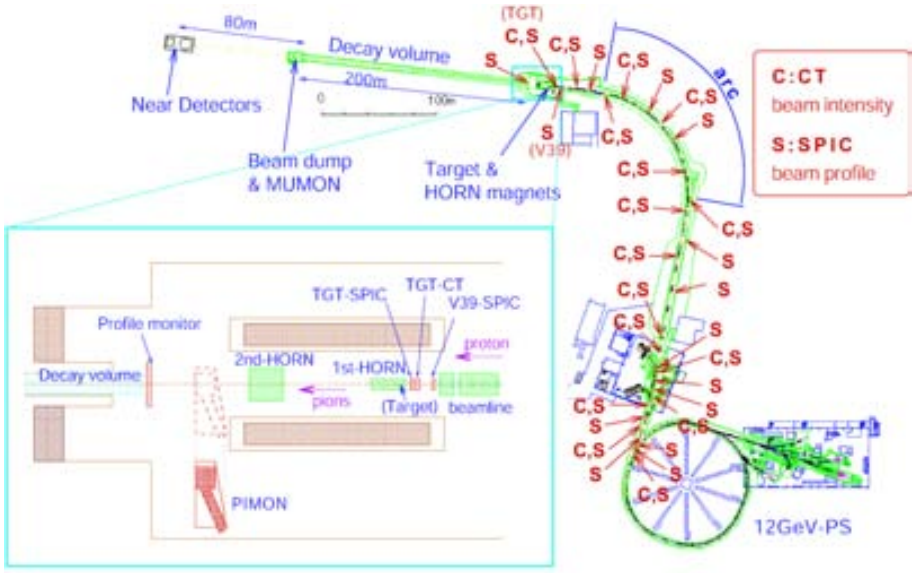

Figure 3.2: KEK-PS and neutrino beam line.

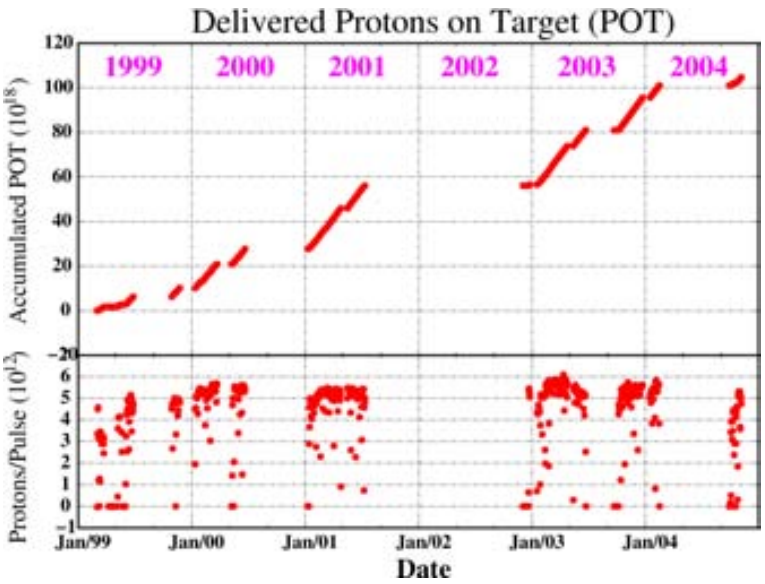

Figure 3.3: Protons on target accumulated (upper plot) and beam intensity (lower plot) from March 1999 to November 2004.

description of the horn magnets are found in [Y$^+$97, Y$^+$99].

The typical momentum of focused pions is around 2-3 GeV/c, which lead to neutrinos that decay in the forward direction with an energy of about 1.0 - 1.5 GeV. These pions enter in a 200 m long decay volume 19 m downstream of the target. It is a

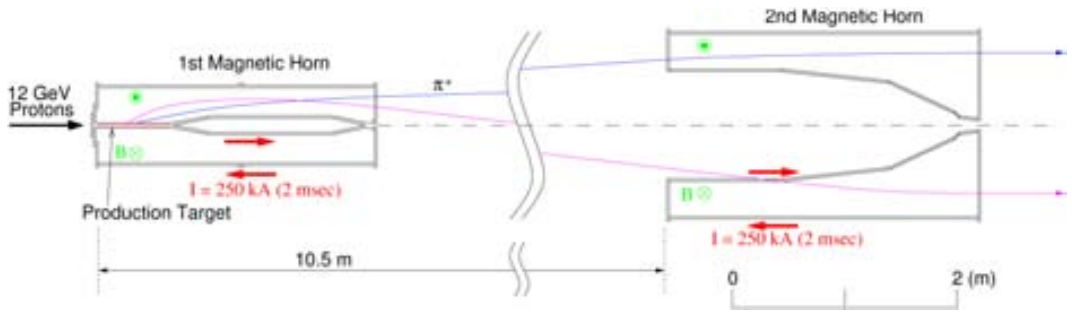

Figure 3.4: Schematic view of the horn magnets.

pipe of 1.5 m diameter in the first 10 m, 2 m diameter in the following 90 m and 3 m diameter in the last 100 m. It is filled with helium gas at 1 atm to reduce the loss of pions by absorption and scattering. Most pions flying in this volume disintegrates in $\pi^+ \rightarrow \mu^+\nu_\mu$, producing a neutrino beam 98% pure ν_μ acording to simulations.

To do neutrino flux measurements the pion monitor (PIMON) can be placed just downstream of the horns. By measuring the pion angle and energy spectrum one can calculate the produced neutrino flux. PIMON is a gas Čerenkov imaging detector which consists of a freon (C_4F_8) gas vessel, a spherical mirror section in it and an array of 20 photomultiplier tubes (PMT) in the mirror focal plane (Fig. 3.5). When pions cross through the gas vessel, they produce Čerenkov light rings. This light is reflected by the mirror in such way that the size of the ring image produced in the focal plane depends on the pion energy and the ring vertical position depends on the pion angle. To disentangle pions of different energies, the energy threshold of ring production is changed by changing the gas pressure.

At the end of the decay volume, the beam dump consist of 3.5 m of iron, 2 m of concrete and 60 m of soil. Just after the 2m of concrete there is a pit with two muon monitors (MUMON) to control the neutrino beam direction. One is an ionization chamber (ICH) and the other is a silicon pad detector array (SPD). Muons with momentum greater than 5.5 GeV/c can reach these detectors. Since neutrinos and muons are produced in the same direction because of the Lorentz boost, measuring the muon flux profile allows to infer the neutrino pointing direction. This monitoring is very important because a change in the beam direction by 3 mrad corresponds to a change in the neutrino flux of about 1%. As seen in figure 3.6 the beam direction is very stable, remaining all the triggered good extractions within a variation < 1 mrad.

3.1.2 Near Detectors

300 m downstream of the target is the near detector pit. The near detector set for the K2K-I period consist of the one kiloton water Čerenkov detector (1KT), the scintillat-

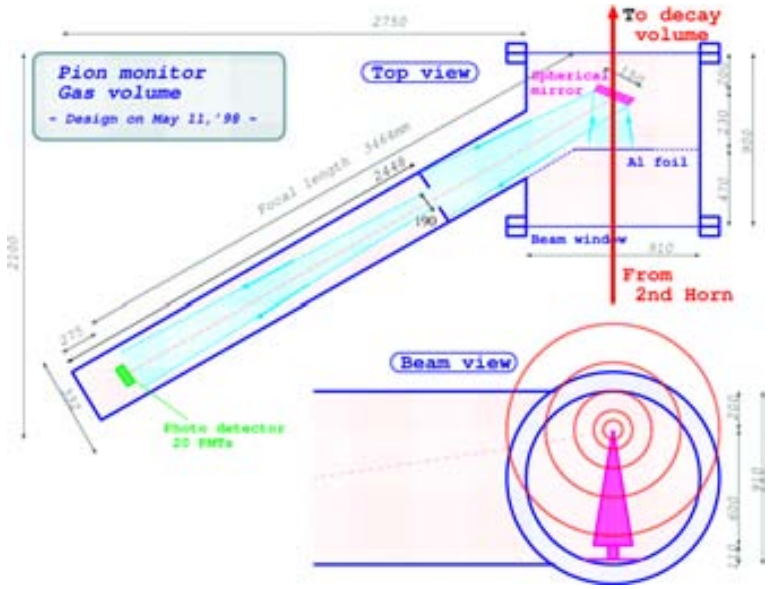

Figure 3.5: Schematic view of the pion monitor.

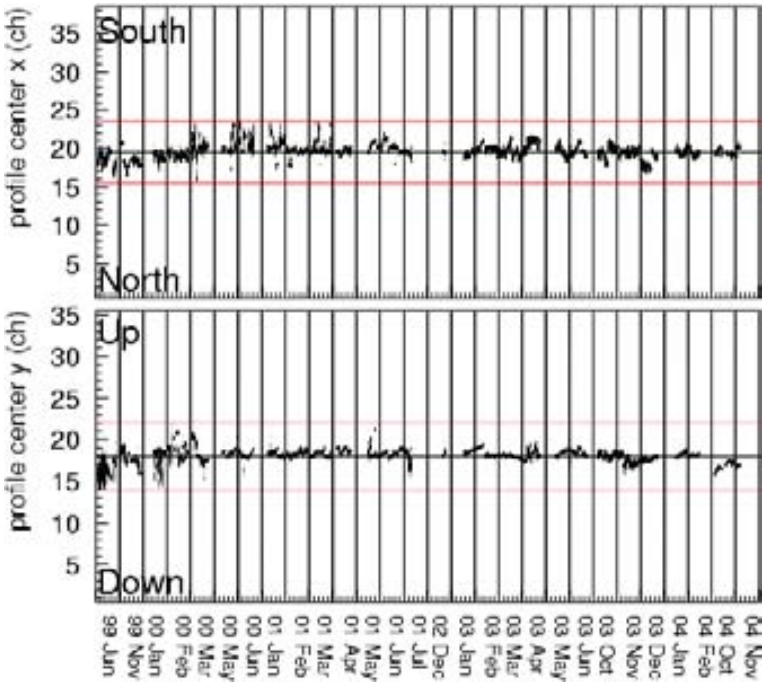

Figure 3.6: Stability of the neutrino beam pointing direction measured by the ionization chamber in MUMON for triggered good extractions. The red lines show a variation of $\pm$ 1 mrad in the pointing direction.

ing fiber detector (SciFi), the lead glass calorimeter (LG) and the muon range detector (MRD). For the K2K-II period the LG calorimeter was replaced by the scintillation bars detector (SciBar) (Fig. 3.7).

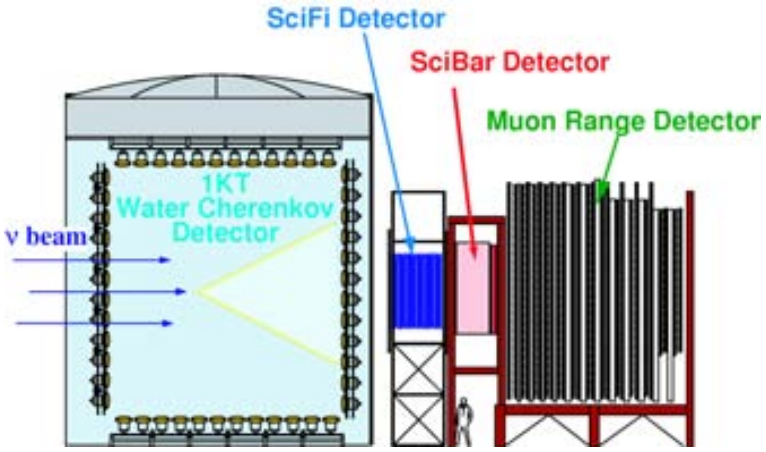

Figure 3.7: Schematic view of the near detector for the K2K-II period.

The 1KT Čerenkov detector is a miniature version of the far detector SK and uses the same neutrino interaction target, instrumentation and reconstruction algorithms (Fig. 3.8). The main purpose of the 1KT is to measure the ν_μ interaction rate and energy spectrum. It reach an angular resolution for muons of 1.05° and the momentum resolution is estimated to be better than 2.5%. It also provides high statistics measurement of neutrino-water interactions. The center of the detector is placed 294 m downstream of the pion production target. It consist of a cylindrical tank of 10.8 m diameter and 10.8 m height that holds approximately 1000 tons of pure water.

The water is optically separated into the inner detector (ID) and the outer detector (OD) by opaque black sheets and reflective Tyvek® sheets. The ID is a cylindrical volume of 8.6 m height and 8.6 m diameter. This volume is viewed by 680 PMTs, giving a 40% photocathode coverage. The OD is viewed by 68 PMTs facing outward to veto incoming particles and trigger cosmic ray muons.

The SciFi detector is a 6 ton tracking detector consisting on a sandwich of 20 tracking modules and 19 water targets (Fig. 3.9). The main purpose of the SciFi detector is to measure the neutrino spectrum and neutrino interactions in water using tracking techniques. Each of the tracking modules has a surface of 2.6×2.6 m and are made of two layers of scintillating fibers; one horizontally and the other vertically oriented. The fibers are 0.692 mm in diameter and are coupled in bunches to an image intensifier tube coupled to a CCD. Reading the CCD image one recovers the hit position. The targets are aluminium studded tanks filled with water. This gives a fiducial volume of 5590 Kg, 70% H2O, 22% Al and 8% HC. More details of the SciFi design and performance

can be found in [S+00].

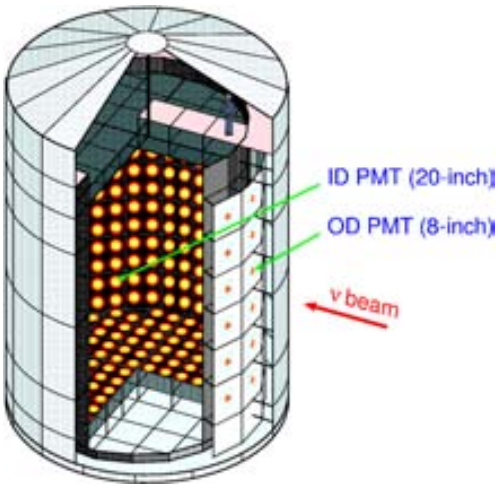

Figure 3.8: Schematic view of the 1KT detector.

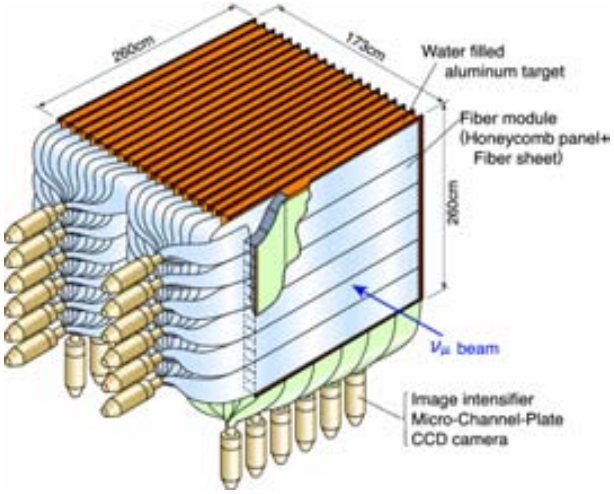

Figure 3.9: Schematic view of the SciFi detector.

The lead glass (LG) calorimeter was only used in the K2K-I period. Is was placed between SciFi and MRD to distinguish between electrons and muons by the energy deposition. It consists of 600 LG scintillators of $12 \times 12 \times 34$ cm^3 read by a PMT through a cylindrical LG light guide.

In the K2K-II period, the LG calorimeter was substituted by the SciBar detector in order to have a fine tracker detector and a better calorimeter. SciBar is a carbon fully-active tracker and an electromagnetic calorimeter (EC). Because the importance of this detector for this thesis, it will be described in detail in chapter 4.

MRD is the last detector downstream. It has two purposes. One is to monitor the stability of the neutrino beam direction, profile and spectrum by detecting muons produced in charged current (CC) interactions in iron. The other purpose is to identify those muons produced by CC interactions in the other upstream detectors and to measure accurately its energy.

The MRD consists of 12 iron layers instrumentalized with 13 layers of drift tubes (DT). The surface of the DT layer is 7.6×7.6 m^2. Each DT layer consists of 2 DT planes, one horizontal and one vertical. And each DT plane is made of DT modules (Fig. 3.10). Each module has eight aluminium DT with a cross section of 70×50 mm^2. They are filled with P10 gas (Ar : CH_4 = 90%:10%). The iron layers are 20 cm thick except the first four, which are 10 cm thick to increase the low energy resolution. The total iron thickness is 2.00 m covering the muon energy from 0.3 to 2.8 GeV with an energy resolution of 0.12 GeV for forward-going muons.

The relationship between muon momentum and range is based on a GEANT3 simulation. In data, the muon momentum is re-weighted with a fit parameter p_{scale}. This

fit parameter is crucial for a good energy reconstruction and was evaluated in the K2K full analysis [A$^+$06] with a value of $p_{\rm scale} = 0.976 \pm 0.004$. The tracking efficiency is 66%, 95% and 97% for tracks that traverse one, two and three iron layers respectively; and up to 99% for longer tracks. The angular resolution is about 5°. More details of the MRD construction and performance can be found in [I$^+$02].

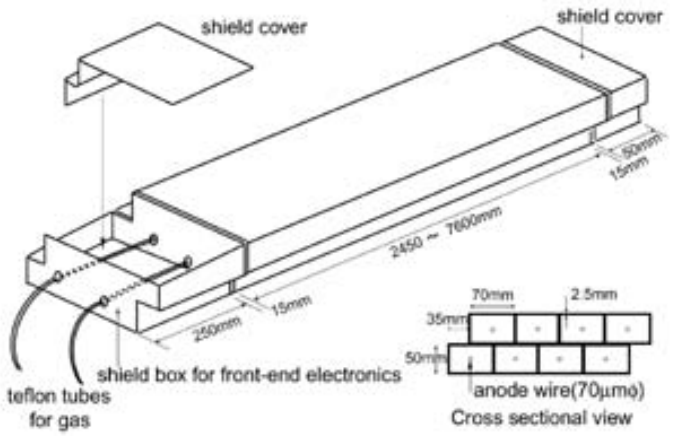

Figure 3.10: Schematic view of an MRD module.

3.2 K2K experimental technique for neutrino oscillation measurements

The main purpose of the K2K experiment is to measure the neutrino oscillation via the ν_μ disappearance. The probability of this process depends on $\sin^2 2\theta$, Δm^2 and the ration E/L (Eq. 2.10). Since $\sin^2 2\theta$ and Δm^2 are physical parameters and L is fixed by the distance between the near and far detector, the neutrino oscillation is only energy dependent. Therefore, the signature of the process would be a decrease of the number of neutrinos and a deformation of the energy spectrum of neutrinos traveling from near to far detector. To illustrate this, figure 3.11 shows the predicted energy spectrum distortion at SK for $\sin^2 2\theta = 1.0$ and $\Delta m^2 = 3 \times 10^{-3}(\ {\rm eV}/c^2)^2$.

In order to observe this signature, one has to calculate the neutrino flux ratio between near and far detector to make the extrapolation, and to measure simultaneously the neutrino event rates and energy spectrum at the near and far detectors. The neutrino flux ratio is calculated with beam MC (see section 5). The event rates are measured with the 1KT detector and in SK by measuring the number CC events. In the near detector the flux is so high that multiple interactions per spill may occur in the 1KT. The MC shows a 2.3% underestimation of multi-interactions in the 1KT fiducial volume, wich is corrected in the near detector event rate. To identify the neutrinos comming

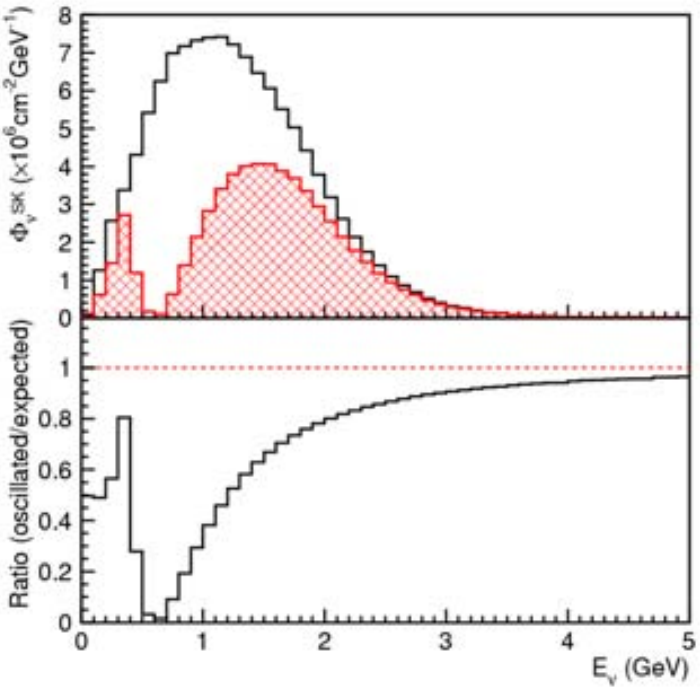

Figure 3.11: Expected neutrino energy spectrum distortion at SK due to neutrino oscillation. Blank histogram shows the case of no oscillation and red hatched histogram shows the case of two neutrino oscillation. The lower histogram shows the ratio.

from KEK in the far detector, SK is sincronized with KEK via GPS and only neutrino measurements with the righ arrival time are used for the measurement. In the wole data adquisition SK measured 112 full contained events on-time.

The measurement of the neutrino energy spectrum is done with CC quasi-elastic (CCQE) events. In CCQE interactions one can reconstruct the neutrino energy from muon momentum and angle as

$$E_{\nu}^{\mathrm{rec}} = \frac{m_N E_{\mu} - m_{\mu}^2/2}{m_N - E_{\mu} + P_{\mu}\cos\theta_{\mu}} \tag{3.1}$$

neglecting Fermi motion and where m_N is the nucleon mass, E_{μ} is the muon energy, m_{μ} is the muon mass, P_{μ} is muon momentum and θ_{μ} is the muon scattering angle respect to the beam direction. However not all muon events are CCQE and the Čerenkov detector can not distinguish them properly. Figure 3.12 shows that the neutrino energy is well reconstructed for CCQE events, but it is lower than true energy for non-CCQE events. Therefore one has to measure the other CC interactions to evaluate the fraction of non-CCQE interactions and to ensure that the MC is well reproducing all the involved neutrino interactions.

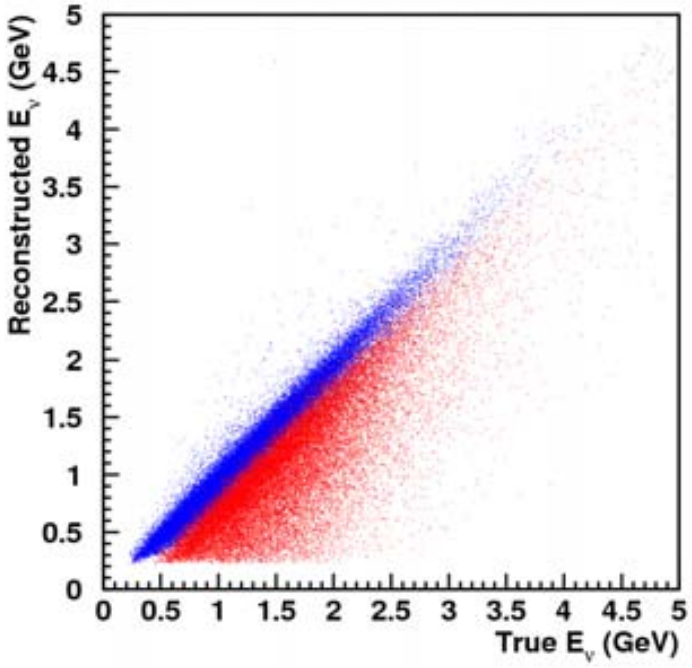

Figure 3.12: Reconstructed neutrino energy versus true neutrino energy for CCQE events (blue) and CC non-QE events (red).

In SK one selects CC events with one muon ring ($1R_\mu$) as CCQE events and measure the muon direction and energy to calculate the neutrino energy. In the whole data acquisition SK measured 58 $1R_\mu$ events. In the near detector, 1KT can not measure with enough precision the whole neutrino energy spectrum. Therefore, the neutrino spectrum is obtained by fitting the (p_μ, θ_μ) MC distributions to CC data from 1KT, SciFi and SciBar detectors. Four different fits has been done, three using data from a single detector and one combining data from all three detectors. The fitting factors are eight energy bins (f_i ; $i = 1 \ldots 8$), the relative weight of non-QE respect to QE (R_{nQE}), and the systematic effects on each detector (see table 3.1). The peak bin f_4 is fixed to one ($\equiv \mathbf{1}$) for the normalization. In single detector fits other energy bins has been fixed to one when fit is not sensitive to variations in that been. The results of the fit are summarized in tables 3.1 and 3.2.

In order to get the neutrino oscillation parameters one compares with a likelihood $\mathcal{L}$ the SK number of events and energy spectrum with the one extrapolated from the near detector. This extrapolation uses HARP π^+ data for the neutrino flux shape and applies the neutrino oscillation theory (Sec. 2.2) for the spectrum deformation.

Finally, to obtain the oscillation parameters $(\sin^2 2\theta, \Delta m^2)$, one maximizes $\mathcal{L}$ leaving

parameter	**Combined**	1KT only	SciFi only	SciBar only
f_1 (0.00-0.50 GeV)	$\mathbf{1.657 \pm 0.437}$	2.372 ± 0.383	$\equiv 1$	$\equiv 1$
f_2 (0.50-0.75 GeV)	$\mathbf{1.107 \pm 0.075}$	1.169 ± 0.072	0.882 ± 0.317	1.166 ± 0.251
f_3 (0.75-1.00 GeV)	$\mathbf{1.154 \pm 0.061}$	1.061 ± 0.065	1.157 ± 0.201	1.145 ± 0.134
f_4 (1.00-1.50 GeV)	$\equiv \mathbf{1}$	$\equiv 1$	$\equiv 1$	$\equiv 1$
f_5 (1.50-2.00 GeV)	$\mathbf{0.911 \pm 0.044}$	0.709 ± 0.151	0.980 ± 0.107	0.963 ± 0.070
f_6 (2.00-2.50 GeV)	$\mathbf{1.069 \pm 0.059}$	$\equiv \mathbf{1}$	1.188 ± 0.096	0.985 ± 0.086
f_7 (2.50-3.00 GeV)	$\mathbf{1.152 \pm 0.142}$	$\equiv \mathbf{1}$	1.062 ± 0.230	1.291 ± 0.283
f_8 (3.00- GeV)	$\mathbf{1.260 \pm 0.184}$	$\equiv 1$	1.323 ± 0.203	1.606 ± 0.749
R_{nQE}	$\mathbf{0.964 \pm 0.035}$	0.589 ± 0.071	1.069 ± 0.060	1.194 ± 0.092
$\mathrm{P}^{\mathrm{1kt}}_{\mathrm{Norm}}$	$\mathbf{0.948 \pm 0.024}$	1.172 ± 0.046	—	—
$\mathrm{P}^{\mathrm{1kt}}_{\mathrm{energy}}$	$\mathbf{0.984 \pm 0.004}$	0.993 ± 0.007	—	—
$\mathrm{P}^{\mathrm{SF}}_{\mathrm{Norm}}$	$\mathbf{1.009 \pm 0.029}$	—	0.925 ± 0.058	—
$\mathrm{P}^{\mathrm{SF}}_{\mathrm{Escale}}$	$\mathbf{0.980 \pm 0.006}$	—	0.980 ± 0.007	—
$\mathrm{P}^{\mathrm{SF}}_{\mathrm{LG-density}}$	$\mathbf{0.929 \pm 0.012}$	—	0.928 ± 0.012	—
$\mathrm{P}^{\mathrm{SF}}_{\mathrm{LG-cluster}}$ [GeV]	$\mathbf{-0.001 \pm 0.002}$	—	-0.002 ± 0.003	—
$\mathrm{P}^{\mathrm{SF}}_{\mathrm{2nd-track-eff}}$	$\mathbf{0.959 \pm 0.014}$	—	0.932 ± 0.017	—
$\mathrm{P}^{\mathrm{SF}}_{\mathrm{rescattering}}$	$\mathbf{1.048 \pm 0.055}$	—	0.993 ± 0.062	—
$\mathrm{P}^{\mathrm{SB}}_{\mathrm{Norm}}$	$\mathbf{0.998 \pm 0.010}$	—	—	1.003 ± 0.011
$\mathrm{P}^{\mathrm{SB}}_{\mathrm{p-scale}}$	$\mathbf{0.976 \pm 0.004}$	—	—	0.972 ± 0.004
$\mathrm{P}^{\mathrm{SB}}_{\mathrm{2trk/1trk}}$	$\mathbf{0.953 \pm 0.021}$	—	—	0.961 ± 0.023
$\mathrm{P}^{\mathrm{SB}}_{\mathrm{nonQE/QE}}$	$\mathbf{1.066 \pm 0.032}$	—	—	0.978 ± 0.040
$\chi^2_{\mathrm{total}}/\mathrm{DOF}$	**687.2 / 585**	46.8 / 73	328.7 / 273	253.3 / 228
$\chi^2_{\mathrm{1kt}}/\mathrm{N_{bin}}$	**85.4 / 80**	47.7 / 80	—	—
$\chi^2_{\mathrm{SciFi}}/\mathrm{N_{bin}}$	**335.6 / 286**	—	328.7 / 286	—
$\chi^2_{\mathrm{SciBar}}/\mathrm{N_{bin}}$	**266.1 / 239**	—	—	253.3 / 239

Table 3.1: Results of the spectrum measurement. The best fit value of each parameter is listed for the fits with all the detectors' data, with the 1KT data, with the SciFi data and with the SciBar data, respectively.

	f_1	f_2	f_3	f_5	f_6	f_7	f_8	R_{nQE}
f_1	43.86	-3.16	7.28	-2.21	-0.76	-3.48	0.81	-8.62
f_2	-3.16	7.51	1.97	1.90	0.62	1.29	2.43	-5.68
f_3	7.28	1.97	6.00	3.38	1.63	3.44	1.71	-2.99
f_5	-2.21	1.90	3.38	4.04	-1.86	4.53	2.20	1.65
f_6	-0.76	0.62	1.63	-1.86	5.28	-5.85	5.11	0.94
f_7	-3.48	1.29	3.44	4.53	-5.85	13.67	-10.14	4.09
f_8	0.81	2.43	1.71	2.20	5.11	-10.14	18.35	-11.77
R_{nQE}	-8.62	-5.68	-2.99	1.65	0.94	4.09	-11.77	20.30

Table 3.2: The error matrix for f_{i} and R_{nQE}. The square root of error matrix (sign $[M_{ij}] \cdot \sqrt{|M_{ij}|}$) is shown here in the unit of %.

free these parameters in the extrapolation. The likelihood is made of three terms, the normalization, the energy shape and the systematics term. The normalization term is defined as the Poisson probability to observe the 112 CC events in SK for the given extrapolation of the number events measured in 1KT. The energy shape term is defined as the product of the probability for each $1R_\mu$ event to be observed at the given neutrino energy, according to the re-weighted MC. The systematic term treat the systematic parameters as fit parameters that behave like Gaussian distributions.

The final result, where the likelihood maximizes, is for $(\sin^2 2\theta, \Delta m^2) = (1.0, 2.8 \times 10^{-3}\ \mathrm{eV}^2)$. Figure 3.13 shows the allowed regions of oscillation parameters found in the K2K experiment together with the SK result [A$^+$04b].

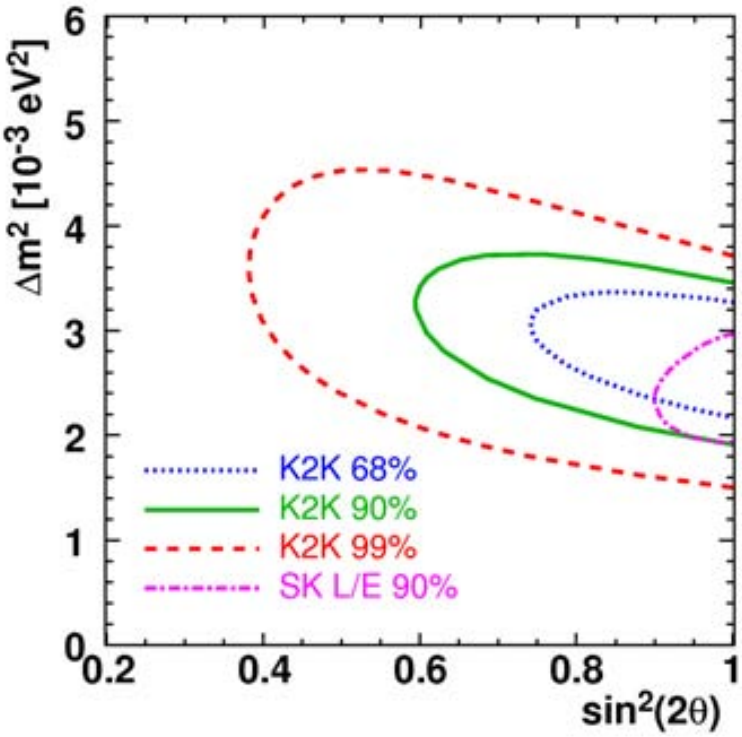

Figure 3.13: Comparison of K2K results with the SK atmospheric neutrino measurement [A$^+$04b]. Dotted, solid, dashed and dash-dotted lines represent 68%, 90%, 99% C.L. allowed regions of K2K and 90% C.L. allowed region from SK atmospheric neutrino, respectively.

Chapter 4

SciBar

The purpose of the SciBar detector is to measure the neutrino energy spectrum and to study neutrino interactions with high reconstruction efficiency even for low momentum particles.

In this chapter the Scibar detector is described in detail as well as its tracking method. More detailed descriptions can be found in [N$^+$04], [Y$^+$05] and [Has06].

4.1 Detector components

SciBar is made of a carbon full-active tracker and an electromagnetic calorimeter (EC).

The tracker consists of 14 848 scintillating bars. They are organized in planes made out of 116 bars glued together. One vertical and one horizontal plane creates one layer. SciBar has 64 layers with a total volume of $1.7 \times 3 \times 3$ m^3 and a weight of about 15 tons of full active material (Fig. 4.1).

Each bar has a wavelength shifting (WLS) fiber in the middle. When a particle pass through the bar producing light, the WLS fiber guides the light to a multi-anode photomultiplier tube (MAPMT). Each MAPMT has 64 channels in an 8×8 array and is connected to a front-end electronics board (FEB). Signals coming from every 8 FEB are read with one VME board and sent to the event builder computer.

4.1.1 Scintillating Bars

The extruded scintillator used in SciBar is made of Dow STYRON 663 polystyrene (C_8H_8) pallets doped with PPO[1] (1% by weight) and POPOP[2] (0.03% by weight). The bars are $302\pm1cm$ long and have a rectangular cross section of $12.9\pm0.3\times25.0\pm0.2$ mm^2 with a $\varnothing1.8mm$ hole in the middle (Fig. 4.2). The bars have a 0.25 mm reflective coating made of 85% C_8H_8 and 15% TiO_2 . The emission spectrum is shown in Fig. 4.3.

[1] 2,5-diphenyloxazole

[2] 1,4-bis(5-Phenyloxazole-2-yl)benzene

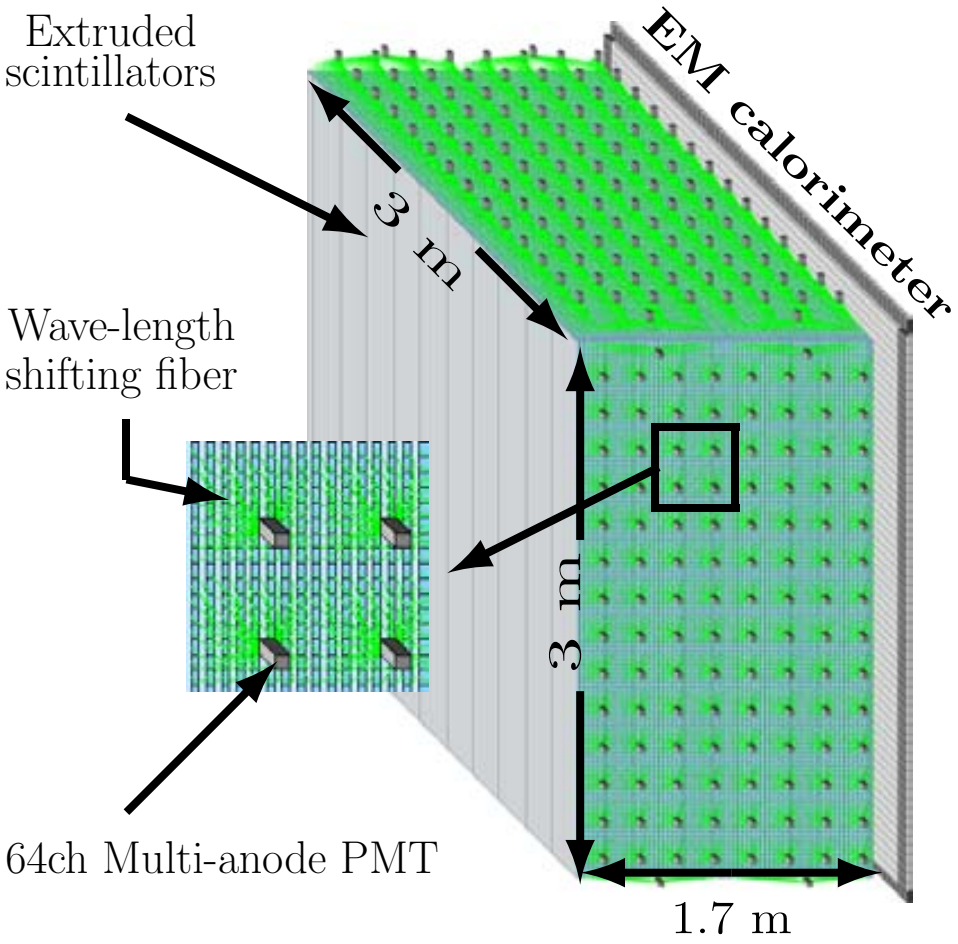

Figure 4.1: Schematic view of the SciBar detector.

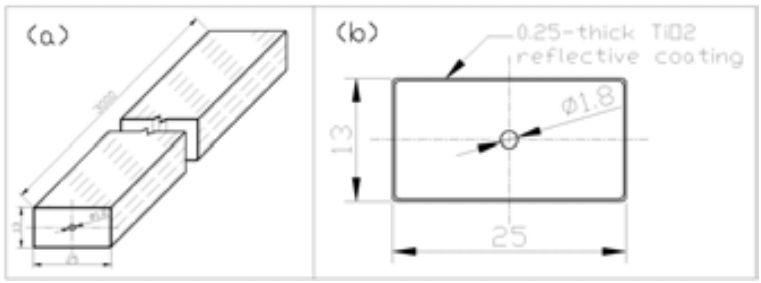

Figure 4.2: Scintillating bar design drawing.

4.1.2 WLS Fibers

Because the attenuation length of the scintillation light in the bar is less than 10 cm, one would loss all the scintillation light before reaching the bar edge. Therefore, WLS fibers (Kuraray Y11 (200) MS) are installed in the center of each bar. The WLS fibers

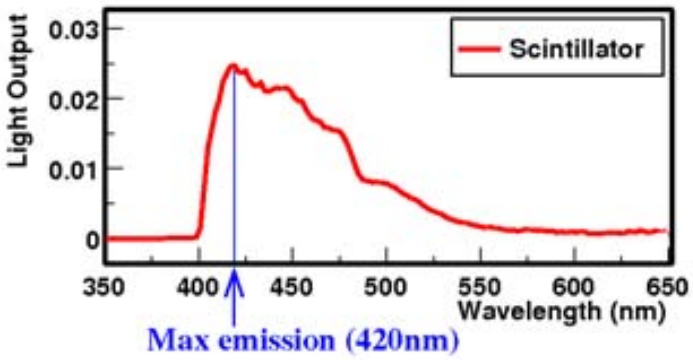

Figure 4.3: Emission spectrum for scintillating bars.

have an attenuation length of 350 cm, allowing that a large fraction of the scintillating bar light arrives to the MAPMT.

The WLS fibers (1.5 mm in diameter) has a polystyrene core with 200 ppm of WLS fluor, an acrylic inner clad and polyfluor outer clad (Fig. 4.4). These fiber components have refraction indexes 1.59, 1.49 and 1.42 working as a light guide for emitted photons with angles lower than 26.7 degree. Scintillating light absorbed by the fiber is re-emitted in the fiber with a different wave length. The fraction of this light that is emitted at low angles is trapped by the refraction index structure and guided to the MAPMT. The absorption and emission wavelength spectrum of the fiber are shown in Figure 4.5. Comparing the absorption spectrum with the scintillating bar spectrum (Fig. 4.4) one can see that the regions of maximal emision amb maximal absorption overlaps.

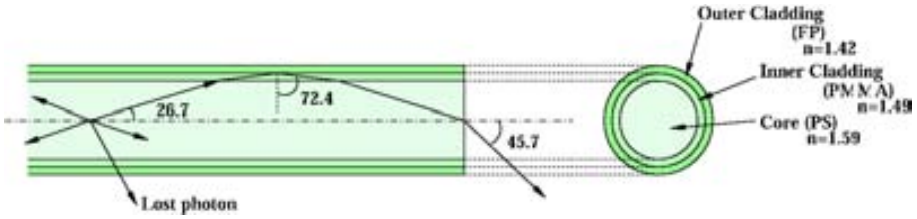

Figure 4.4: WLS fiber Kuraray Y11 (200) MS.

4.1.3 MAPMTs

The fiber light is detected by Hamamatsu H8804 MAPMTs. One MAPMT has 64 channels arranged in an 8×8 array. Each channel is 2×2 mm^2 and have a separation of 0.3 mm between them (Fig. 4.6).

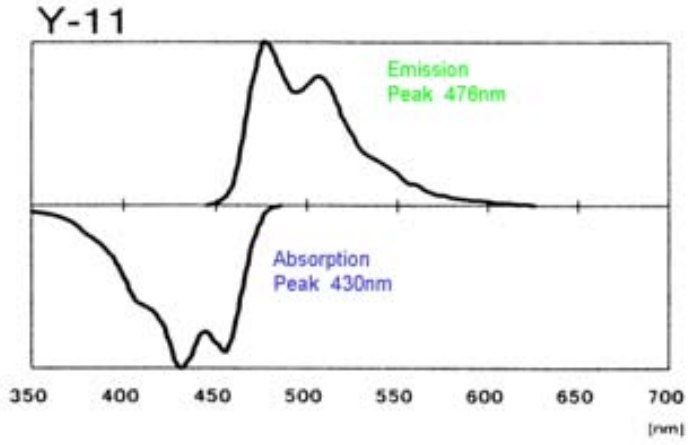

Figure 4.5: Absorption and emission spectra for WLS fibers.

Groups of 64 fibers are bundled together with a fixture that keep them exactly spaced allowing a precise alignment with the MAPMT channels. The light going from the fiber to the cathode disperses, illuminating neighboring channels. Due to this crosstalk effect, neighbour channels get about 3% of central channel light. This effect has been parametrized and is corrected event by event [Whi07].

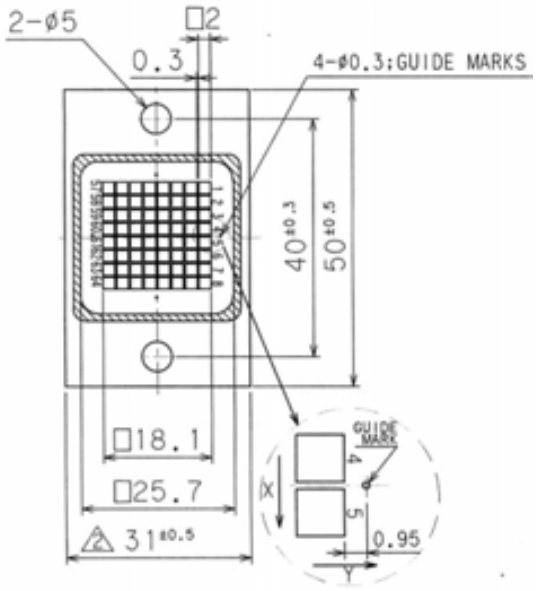

Figure 4.6: Schematic drawing of Hamamatsu H8804 MAPMT.

The MAPMT photocathode is coated with a bialkali (Sb-K-Cs) material providing a wavelength coverage from 300 to 650 nm. The highest quantum efficiency is 21% for 390 nm photons and 12% for 500 nm wavelengh photons at the WLS fiber emision peak.

The typical channel gain is 3×10^5 with a voltage supply of 800 V and the response linearity is kept within 10% for up to 200 photo-electrons (p.e.). The gain and linearity of each channel was measured before intallation. Gain variations are monitored each spill as explained in next subsection. Gain variations are take into account to correct the p.e. per channel.

The energy calibration for each channel is made after each beam spill by measuring the light yield by cosmic-ray muons. In this measurement one corrects for the attenuation effect in the WLS fiber. This shows that minimal ionizing particles yield about 20 p.e. in average per bar width (1.3 cm) (Fig. 4.7). The distribution of calibration constants inferred from the measurement of all bars are shown in Figure 4.8. The calibration constants are found to be stable within 1% for the whole period of operation.

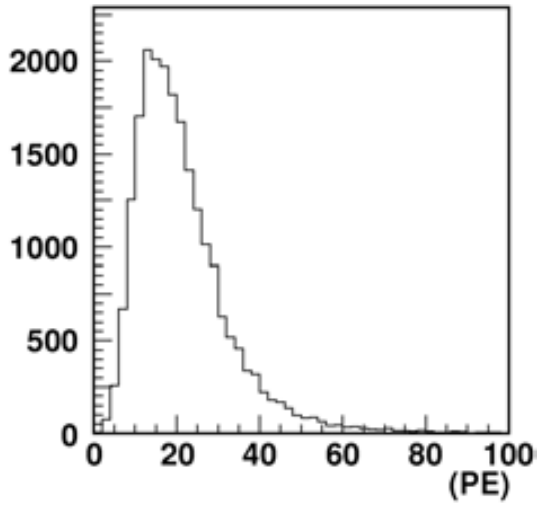

Figure 4.7: Number of photo-electrons yield in a typical scintillator bar width (1.3 cm) by cosmic-ray muons.

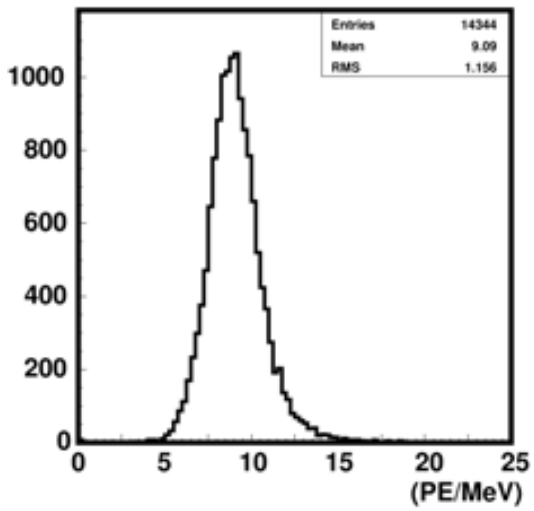

Figure 4.8: Energy calibration constant distribution.

4.1.4 Gain monitor

The gain of each MAPMT channel is also monitored after each spill. This is done by illuminating uniformly all detector channels. The light source is a blue LED which intensity is monitored with one pin photo-diode and a calibrated PMT. Each bundle of 64 fibers has a light injection module and the LED light is guided into these modules

with a clear fiber. The light injection module is a cylindrical box that all 64 WLS fibers pass trough (Fig. 4.9). Comparing the MAPMT measurements with the pin diode or the calibrated PMT one can measure relative gain variations with 0.1% precision.

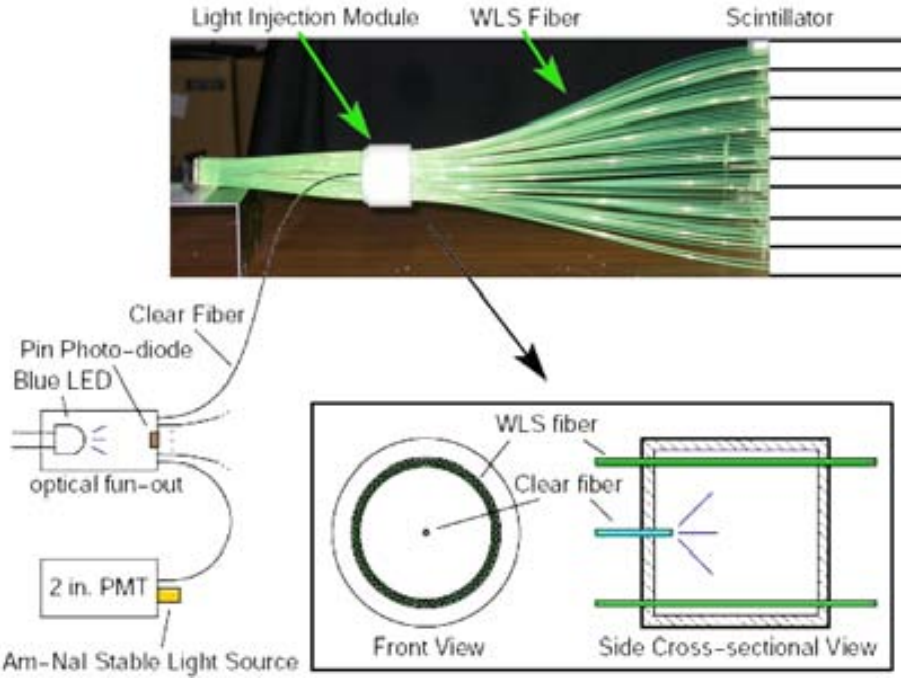

Figure 4.9: Picture of a fiber bundle and the gain monitor system.

4.1.5 Readout

Signals from each MAPMT are read with custom made front-end electronics boards (FEB) and a back-end VME module. The FEB has two ASICs[3], each reading 32 MAPMT channels. In the ASIC the signal is procesed by two modules VA and TA. The VA processing does the pre-amplification, shape the signal and multiplex the result. The TA makes a fast shaping and an OR of the pre-amplified signals. VA and TA pulses are send to the VME module, where the VA charge information is digitalized with a 12 bit FADC, and the TA time information is digitalized with a multi-hit TDC[4]. The VA pedestal width is about 0.3 p.e. and the TA timing resolution is found to be 1.3 ns. A detailed description can be found in [Y+04].

[3]Application-specific integrated circuit
[4]Time to digital converter

4.1.6 Trigger

Every 2.2 seconds one neutrino beam spill is delivered. The peak of the first bunch in the spill is take as 0 ns and this generates a beam trigger that opens a gate from -100 ns to 1200 ns for data collection. Then the LED trigger starts the gain monitor system. After that the LED light is switched off and all PMT are read in the dark to measure the dark noise pedestals. At last the cosmic ray trigger is enabled for calibration data acquisition. Figure 4.10 shows the timing diagram of data acquisition.

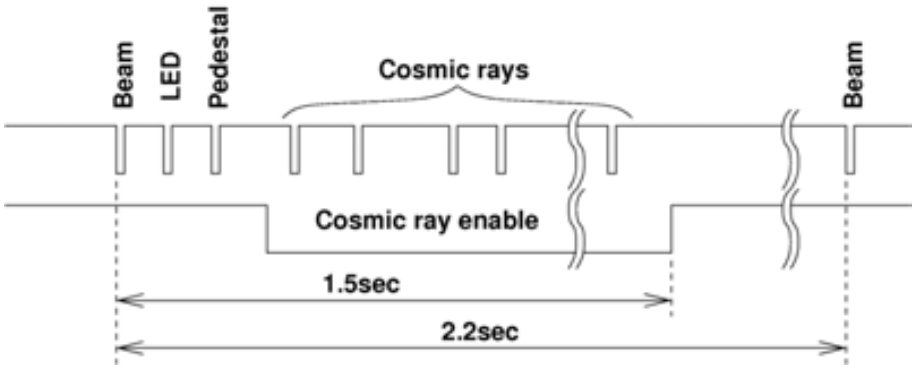

Figure 4.10: Timing structure of data acquisition.

4.1.7 Electromagnetic Calorimeter

Since the SciBar tracker is only about four radiation lengths thick, an electromagnetic calorimeter called Electron Catcher (EC) is installed just downstream from the tracker. The EC adds 11 radiation lengths and its main purpose is to measure the ν_e contamination in the beam and π^0 production in neutrino interactions.

The EC consist of one plane of 30 horizontal modules and one plane with 32 vertical modules. The modules are reused from the CHORUS experiment [E$^+$97]. Each module has two lead cells of $4 \times 4 \times 262$ cm^3 instrumented with scintillating fibers. The scintillating fibers are bundled at the cell edges and read with PMTs at both edges. By measuring the light yield on both edges one can reconstruct the hit position in the cell and get better energy resolution. The measured energy resolution for electrons is $14\%/\sqrt{E(\text{ GeV})}$.

4.2 Tracking

SciBar raw data is a list of hits with its charge, geometrical and time information. In order to get reconstructed tracks out of the list of hits a cellular automaton has been developed. Cellular automata are discrete models where dynamical cell systems evolve according to a set of local rules. The state of each cell changes depending on the state

of neighbour cells.

Because of the detector geometry, the hits from vertical and horizontal planes are used independently for 2D track reconstruction. In a later step 2D tracks from both views are matched to produce 3D tracks and then one looks for 3D tracks matching MRD tracks.

In the tracking process, one performs first a hit selection. Then the hits are grouped in clusters and clusters are connected with a set of initial conditions. Next the connections are let to evolve under cellular automata rules. Surviving connections are the ones composing the track.

Hits and tracks are the basic elements that are used in the analysis as shown in chapter 6.

4.2.1 Clustering

For the clustering one selects hits with more than 2.0 p.e. in order to reject noise hits which are not well reproduced in MC (Fig. 4.11). The next step is to group hits in clusters and connect them with segments. This process is done independently with hits at each view. Clusters are made of contiguous hits in one scintillator plane.

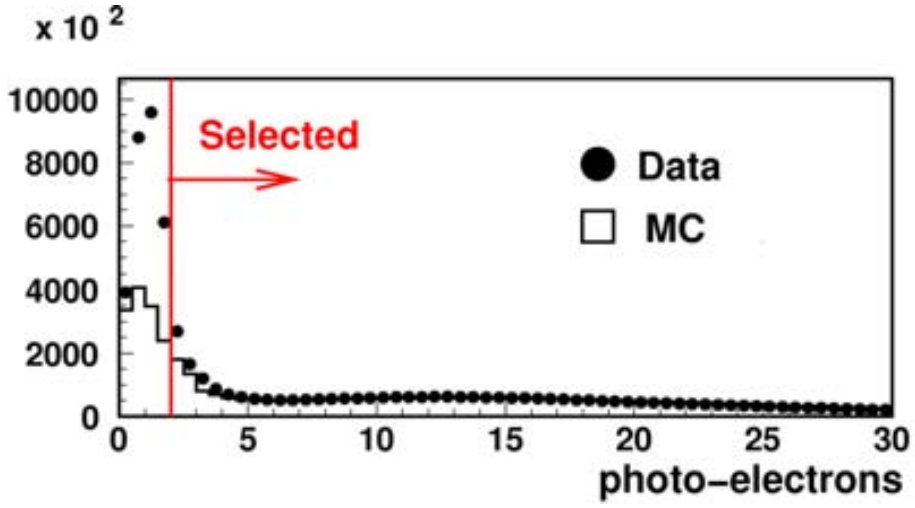

Figure 4.11: Distribution of p.e. per hit for data and MC. The distribution is normalized by the number of entries with more than 5 p.e.

Then clusters are connected with segments when fullfilling the following requirements:

- Clusters are in the same view.

- The clusters are in consecutive planes or with one plane between them.
- Cluster's times are within a 100ns time window. In that way connections to noise hits are reduced.
- If the segment angle is bigger than 1.1 radians then the cluster must have more than 2 hits. 1.1 radians is the diagonal angle of the bar section. Therefore if the segment angle in that view is higher than 1.1 radians then it will geometrically cross more than one bar.

In order to connect segments between them they must be aligned. One evaluates if two segments are aligned by calculating the χ^2 of fitting the segment pair to a straight line. If the χ^2 is below a tuned value, the segments are connected. Segments without connections are deleted.

This process makes a mesh where each segment may have many connected segments upstream and downstream.

4.2.2 Track finding

2D Tracks are extracted from a mesh of linked clusters using a cellular automata. Its purpose is to find the longest path of linked segments and all its possible splits.

The process starts giving a sort index 1 to segments without upstream connections. Then, all segments look for the highest index of its upstream neighbours and get assigned the next index value. In that way one gets a path tree of increasing index values starting from the most upstream segment (Fig. 4.12).

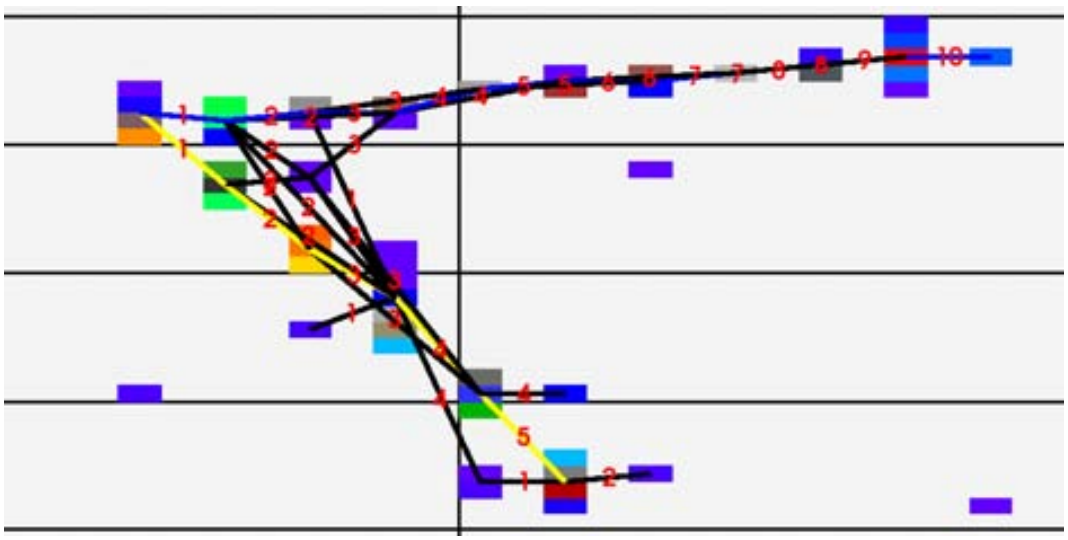

Figure 4.12: Example of section indexing.

From the path tree one keeps the longest path and those path splits that have more than 3 non common segments. In that way one avoid short track splits due to delta

rays but one allows that close tracks share the firsts segments. The result is a list of track candidates (Fig. 4.13).

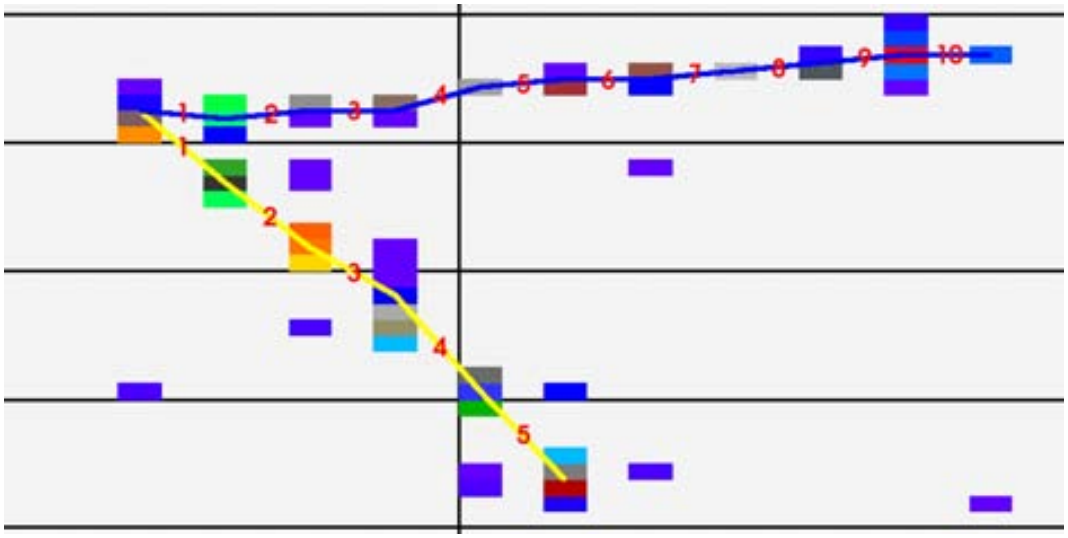

Figure 4.13: Track reconstructed from the mesh of segments.

Tracks candidates are then checked. A time clean up checks and fix hit time deviations above 100ns. A topological clean up removes hits separated from the track direction and then recovers those hits that the track pass through and were not included in the track, like hits with wrong time information or energy below threshold. The track clean up breaks long tracks if they have a kink of more than 0.2 radians, join tracks if they are straight and separated by just one segment and clean edge hits produced by interaction vertex activity if the next plane has no cluster. At the end of the process, tracks with less than 3 planes are rejected.

4.2.3 2D track matching

Once one has the list of tracks for each view one looks for matching track pairs to produce a 3D track. Three methods has been used and are sorted in such way that tracks used in one method are not used in next ones.

The first method relies on MRD matching. One looks for 2D tracks leaving SciBar and matching a 3D MRD track that starts in the first MRD layer. The matching criteria is based on a likelihood function that takes into account the multiple scattering produced in the EC. This function evaluates the energy of each MRD track, the angle difference between the SciBar and the MRD track in each view, and the distance between the intersection point of the SciBar and MRD track in a defined plane between both detectors. One combines the pair of 2D tracks that has the best

likelihood to match the 3D MRD track if the likelihood is better than a threshold value.

The second and third methods are based on the edge position of both views. Since the top and side view have the beam direction as a common axis (Z axis), one asks that the position of track edges in both views must be close in Z.

In case that in one view the track escapes from one side of the detector, one has to extrapolate the track by two cells since the two first and two last cells of each plane veto bars and are not readed because high noise levels.

The second method asks that both edges, upstream and downstream edges, match in Z position. Three different matching conditions are allowed depending on the allowed discrepancy on Z position for both views (Fig. 4.14). 2D tracks matched with a more restrictive condition are not used later in a more relaxed one.

The first matching class requires that distances in Z between both views must be less than 1.4 cm. This would be an optimal matching, since 1.3 cm is the distance between one plane and the next one plus 0.1 cm to allow alignment deviations.

The second class allows the Z distance between both views to be 4.0 cm. This distance corresponds to one plane plus one layer plus the 0.1 cm for possible deviations. This selection recover those tracks that have one cross talk hit at an edge, producing the 1 layer discrepancy.

The third class allows a Z distance of 6.6 cm. This distance corresponds to one plane plus two layers plus the 0.1 cm for possible deviations. This case recovers tracks that have one extended edge because of not cleaned vertex activity hits. These activity hits are produced around the interaction vertex by particles that do not travel enough to produce a track.

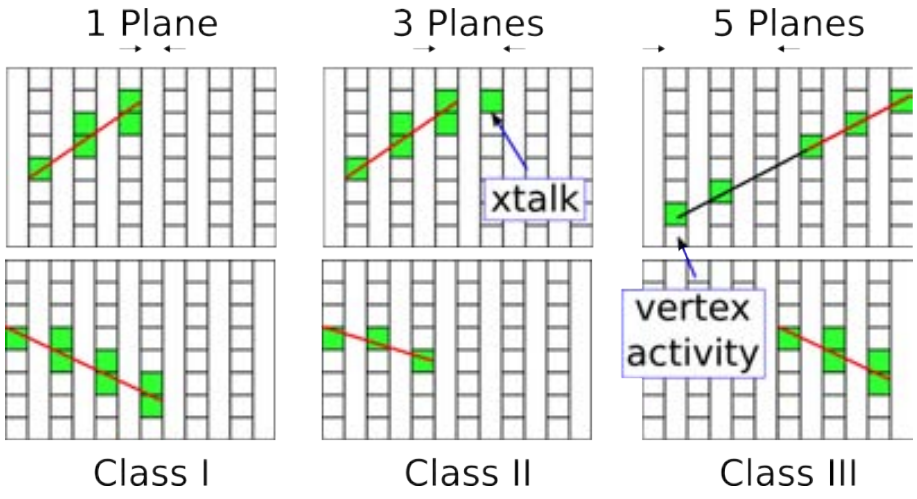

Figure 4.14: Classification of the three conditions used in the matching method based on edge position. For each class a top and side view example is shown. The horizontal axis is Z.

The third method ask that one of both edges match in the Z position. Then one looks for another track that could be joined to the shortest one in order to get a two edge matching of 4.0 cm. In that way one recovers tracks where one view had a broken 2D track.

Once 2D tracks from both views are paired, the 3D track is reconstructed. With the 3D track information one can infer at which point the track pass through each bar. Then one know how long the light has traveled in the fiber and the energy deposition can be corrected for the attenuationYielding an improvement at the track energy reconstruction.

4.2.4 MRD matching

For every SciBar 3D track one looks if it matches with an MRD track. If the 3D track does not match an MRD 3D track, then one checks if it matches with an MRD hit in the first layer.

Matching MRD track candidates must start from the first MRD chamber plane and stop inside MRD in order to reconstruct the muon energy using the range information. The matching condition is that the residual distance between the extrapolation of the SciBar track and the start point of the MRD track in each view is less than 20 cm, and that the angle between both tracks in each view is less than 0.5 radians. If many MRD tracks fit this conditions, the most energetic one is selected.

The matching condition to match an MRD hit on the first layer is the same, but one just looks at the residual distance between the extrapolation of the SciBar track and the MRD hit position.

Chapter 5

Monte Carlo Simulation

The Monte Carlo simulation used by the K2K collaboration is produced in three steps: neutrino beam, neutrino interactions and detector simulations.

The neutrino beam and the detector simulation are based on GEANT 3 and the neutrino interactions are generated with NEUT [Hay02], the program library used in the SK experiment.

5.1 Neutrino beam simulation

The neutrino beam simulation provides the neutrino flux, flavor and neutrino energy spectrum. The beam line geometry and particle tracking in materials has been implemented in GEANT 3 [GD94]. The proton beam profile and divergence is assumed to be gaussian-like and its intensity is the one measured with the SPICs[1] in front of the target. The pion production in the target has been calculated with the Cho-CERN [C$^+$71] model and using the HARP experimental results [C$^+$06] as an input. The HARP results are very important for the simulation since it measures the pion production with the same beam and target properties as at K2K.

The final neutrino flux is then weighted by the factors determined with a spectrum fit described in [A$^+$06]. Table 5.1 gives the weighting factors.

5.2 Neutrino interaction simulation

Neutrino nuclear interactions are simulated with the NEUT program library [Hay02]. Different target materials can be simulated, as HO_2 for Čerenkov detectors and $(CH)_n$ for SciBar. The following neutrino-nucleus interactions are implemented in this package:

[1] Segmented Planes Ionization Chambers

$\mathbf{E_\nu}$ **(GeV)**	**Weighting factor**	σ^2
0.00-0.50	1.657	0.437
0.50-0.75	1.107	0.075
0.75-1.00	1.154	0.061
1.00-1.50	$\equiv 1$	
1.50-2.00	0.911	0.044
2.00-2.50	1.069	0.059
2.50-3.00	1.152	0.142
> 3.00	1.260	0.184

Table 5.1: Neutrino flux weighting from reference [A$^+$06]

CC/NC (quasi-) elastic scattering	$\nu\ N$	$\rightarrow l + N'$
CC/NC single meson production	$\nu\ N$	$\rightarrow l + N' + meson$
CC/NC coherent pion production	$\nu\ ^{16}O\ (^{12}C)$	$\rightarrow l + ^{16}O\ (^{12}C) + \pi$
CC/NC deep inelastic scattering (Nπ)	$\nu\ N$	$\rightarrow l + N' + hadrons$

where ν is the neutrino, N and N' are nucleons (proton or neutron) and l is a lepton.

To calculate the cross sections of these interactions NEUT uses different models.

- Elastic and quasi-elastic scattering are simulated with the Lewellyn Smith model [LS72].
- Single pion production is simulated with the Rein-Sehgal model [RS81] [Rei87] based on neutrino production of resonances and limiting the production of just one pion.
- Charged current coherent pion production is suppressed in the analysis according to previous K2K result [H$^+$05] and the original neutral current coherent pion interaction cross section given by NEUT is corrected by a function of the true neutrino energy. This correction is based on the Marteau model [MDE00].

$$\begin{aligned} weight &= -0.00483E_\nu^4 + 0.08058E_\nu^3 - 0.4838E_\nu^2 \\ &\quad +1.247E_\nu - 0.2149 \end{aligned} \tag{5.1}$$

  were E_ν is the neutrino energy in GeV.

  These interactions use the dipole formula of the nucleon form factor with an axial vector mass of 1.1 GeV/c^2.

- The interaction measured in this study, commonly known as multi-pion, is the low energy deep inelastic scattering (DIS). DIS cross section has been calculated by integrating the following deep inelastic equation [AJ75]:

$$\begin{aligned}
\frac{d^2\sigma}{dxdy} &= \frac{G_F^2 m_N E_\nu}{\pi} \cdot \left[(1 - y + \frac{1}{2}y^2 + C_1)F_2(x) + y(1 - \frac{1}{2}y + C_2)(xF_3(x)) \right] \\
C_1 &= \frac{m_l^2(y-2)}{4m_N E_\nu x} - \frac{m_N xy}{2E_\nu} - \frac{m_l^2}{4E_\nu^2} \\
C_2 &= -\frac{m_l^2}{4m_N E_\nu x}
\end{aligned} \tag{5.2}$$

where $x = Q^2/(2m_N(E_\nu - E_l))$, $y = (E_\nu - E_l)/E_\nu$, G_F is the Fermi constant, m_N is the nucleon mass, m_l is the lepton mass, E_ν is the neutrino energy, E_l is the final lepton energy and $F_2(x)$ and $F_3(x)$ are the parton distribution. In this simulation the parton distributions from reference [GRV95] has been used.

The kinematics of deep inelastic scattering production are divided in two hadronic invariant mass (W) regions. For $1.3 < W < 2.0\ GeV/c^2$ the interaction is named multi-pion (Nπ). In this region Nπ overlaps with the single-pion simulated events and therefore, to avoid double counting, Nπ simulated events are required to have more than one pion. For Nπ a K2K custom-made library has been used to simulate the kinematics [Hay02, N$^+$86] while for $W > 2.0\ GeV/c^2$ (named DIS) the events has been generated with PYTHIA/JETSET [Sjo94].

Neutral current (NC) DIS cross sections are calculated using the following relations based on experimental results [MV78, KLLW81]:

$$\begin{aligned}
\frac{\sigma(\nu_\mu N \to \nu_\mu X)}{\sigma(\nu_\mu N \to \mu^- X)} &= 0.26 \quad (E_\nu \leq 3 \text{ GeV}) \\
&= 0.26 + 0.04 \times \frac{E_\nu(\text{ GeV}) - 3}{3} \quad (3 \text{ GeV} < E_\nu < 6 \text{ GeV}) \\
&= 0.30 \quad (E_\nu \geq 3 \text{ GeV})
\end{aligned} \tag{5.3}$$

$$\begin{aligned}
\frac{\sigma(\bar{\nu}_\mu N \to \bar{\nu}_\mu X)}{\sigma(\bar{\nu}_\mu N \to \mu^+ X)} &= 0.39 \quad (E_\nu \leq 3 \text{ GeV}) \\
&= 0.39 - 0.02 \times \frac{E_\nu(\text{ GeV}) - 3}{3} \quad (3 \text{ GeV} < E_\nu < 6 \text{ GeV}) \\
&= 0.37 \quad (E_\nu \geq 3 \text{ GeV})
\end{aligned} \tag{5.4}$$

5.2.1 Bodek correction

In 2002 Bodek and Yang proposed a correction on the parton distributions $F_2(x)$ and $F_3(x)$ for DIS [BY02]. These corrections improved the agreement of $F_2(x)$ at low Q^2

for lepton scattering data but did not show much improvement on the agreement with neutrino cross section data [BY02].

At first order, the effect of this correction is a reduction of the Nπ+DIS cross section for low Q^2, which is equivalent to apply the weight factor:

$$weight = \frac{Q^2}{Q^2 + 0.188} \qquad (Q^2 \text{ in GeV}^2) \tag{5.5}$$

Even though Bodek correction has been applied in previous K2K measurements, it is not applied in this analysis to avoid biased measurement since the Bodek correction has a big effect on the amount of Nπ. Afterwards, to evaluate the effects of this correction, the result of the analysis applying the Bodek correction is presented in chapter 6.6.

5.2.2 Nuclear effects

Hadrons produced in nucleus as ^{16}O or ^{12}C, have restricted kinematics due to Fermi motion and Pauli blocking. Hadrons may also interact with the nuclear medium in different ways. These bindings are the so called "nuclear effects".

For the Fermi motion simulation the relativistic Fermi gas model of Smith and Moriz [SM72] has been used. The nucleon momentum distribution is assumed to be flat up to the Fermi surface momentum p_F, and it is set to 225 MeV/c for oxygen and carbon and 250 MeV/c for iron. Pauli blocking restricts interactions that has a fermion in the final state with and occupied energy level. This is taken into account by requiring the momentum of the outgoing nucleon to be higher than p_F.

Hadron interactions within the nucleus are of capital importance for this study since in first order one would expect many hadrons mainly pions produced. The Woods-Saxon nucleon density [WS54] is used to set the position of the pion in the nucleus. Then, pion interactions are calculated with the L.L. Salcedo *et al* model [SOVVGR88]. If charge exchange or inelastic scattering occurs, the momentum and direction of the pion are determined based on experimental results of pion-nucleon scattering [RSL78]. The Pauli blocking effect is taken into account in pion scattering by requiring the nucleon momentum after the scattering to be larger than the Fermi surface momentum at the interaction point. The simulation of pion nuclear effects is evaluated by comparison with data (Fig. 5.1).

Kaon and eta interactions in the nucleus are also considered using similar methods as with pions. The simulation of K cross section and kinematics is based on KN and $K\bar{N}$ scattering experiments [MP77a, MP77b, HARW92]. Eta absorption is also considered [Spa84].

The nucleon re-scattering simulation is also based on experimental data [Ber72]. Elastic scattering and delta productions has been considered. For delta production the isobar model has been used [LS57].

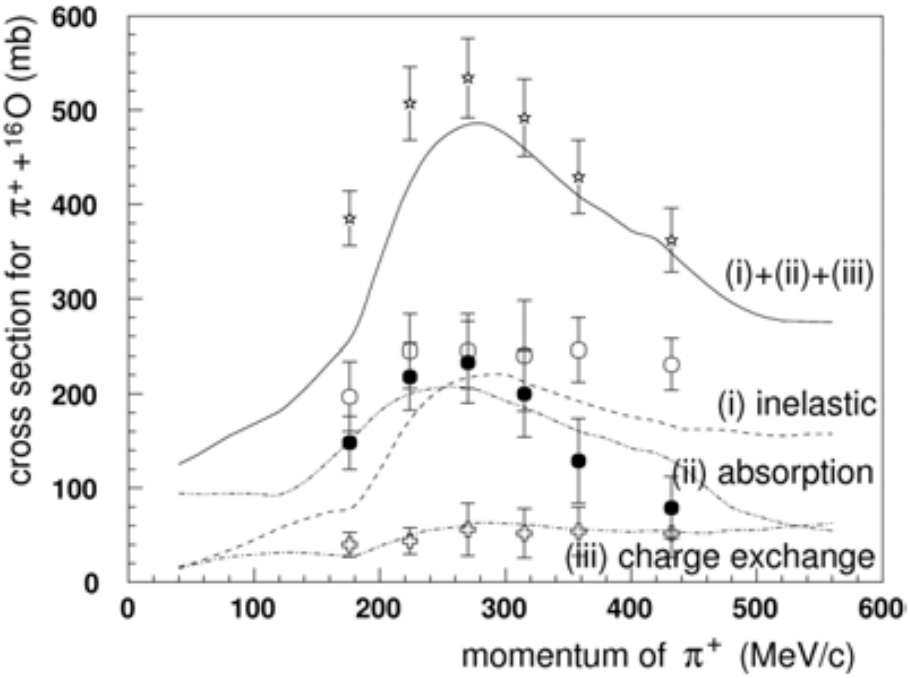

Figure 5.1: $pi^+ + {}^{16}O$ scattering cross sections calculated with NEUT (lines) compared with experimental data [A$^+$81] (points). Data comes from $\pi^+ + {}^{12}C$ scattering and has been re-weighted by 16/12 for the comparison.

5.3 Detector simulation

The detector simulation is based on GEANT3. The particle type and momentum are read from the interaction simulation. The interaction vertex position is randomly distributed in SciBar according to the simulated neutrino beam shape and the event time are randomly generated according to the measured bunch structure. Then GEANT simulate the passage of these particles through the detector using the CALOR program library [ZG94]. For pions below 0.5 GeV/c CALOR does not reproduce properly the data. In such cases a custom library is used [N$^+$86].

The energy deposited in each bar is calculated in terms of photo-electrons. This amount of photo-electrons is corrected first by scintillator quenching effects. This effect was measured in the lab and parametrized with the Birks formula. Figure 5.2 shows the parametrization and the result of the measurement done in a proton beam.

This light is then corrected by the light attenuation in the fiber. This parameter has been measured for each fiber and is used in the simulation. The light from the fibers produces cross talk[2] which is simulated with the parametrization obtained from data cross talk correction [Whi07]. According to this parametrization (Fig. 5.3), the frac-

[2]See section 4.1.3.

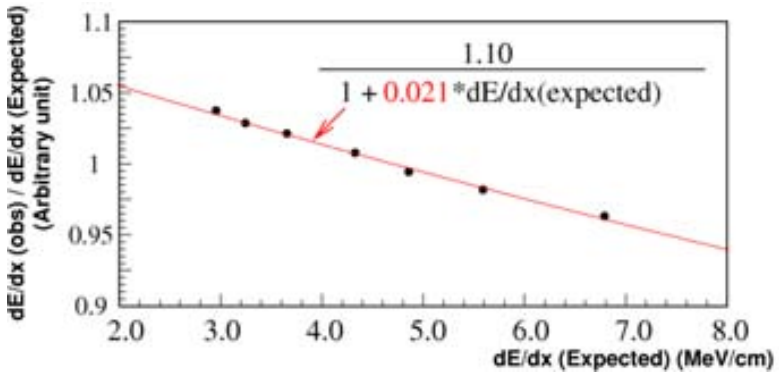

Figure 5.2: Ratio of visible to expected energy loss as function of expected dE/dx.

tion of light in the adjacent channel is $n = 3.25\% \pm 0.25\%$ of the central channel light. The amount of light arriving at each channel is then smeared by Poisson statistics. The PMT charge resolution is simulated by applying a Gaussian smearing to the number of photo-electrons. This MC parameter was evaluated to be $40\% \pm 10\%$ by tuning in MC the dE/dx distribution per plane to match with the cosmic ray data. The front-end electronics noise is also take into account as well as time dependent shaper effects.

The hit time is calculated taking into account the particle time of flight up to the bar and the light propagation through the fiber from the bar up to the PMT. Then this time is smeared by the detector time resolution.

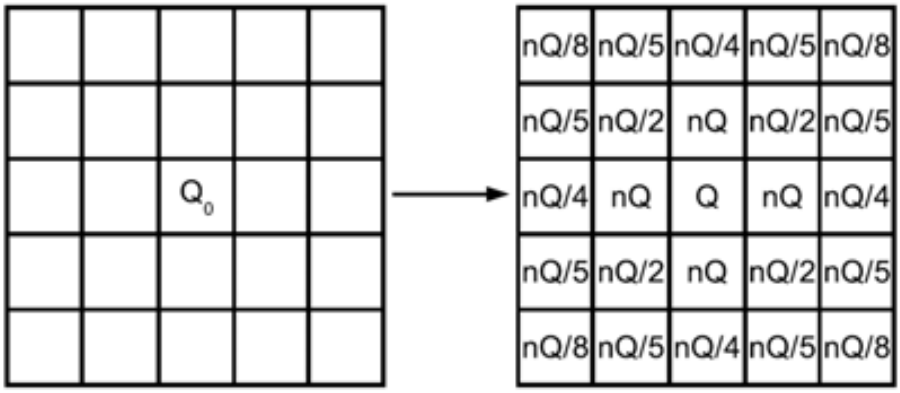

Figure 5.3: Cross talk light distribution model for a given input light Q_0 and an incident light $n \cdot Q$ on the adjacent channel. The light on the central channel is $Q = Q_0/(1 + 9.1 \cdot n)$.

Chapter 6

Analysis

In this chapter we present the method used to analyse data for the measurement of the ratio of the multi-pion to quasi-elastic cross section $(\nu\ N \rightarrow \mu\ N\ \pi\pi(\pi\ldots))\,/(\nu\ n \rightarrow \mu\ p)$. Due to the high uncertainties on the K2K absolute neutrino flux[1], we have choosen to present a relative cross section measurement instead of an absolute cross section measurement.

6.1 Data Selection

For the analysis we use events with at least one muon starting in the fiducial volume. The upstream edge of the muon track is consider as the starting point. To reduce background tracks created by particles coming from outside SciBar, the fiducial volume is defined as a box of 260 cm height and 260 cm width centered in the detector longitudinal axis, that extends from the second to the 53rd layer of scintillator.In figures 6.1 to 6.3 one can see the fiducial cuts and the excess of events in data produced by particles coming from outside SciBar. Figures 6.4 to 6.6 show the data - MC agreement after the fiducial cut.

A muon is identified as a track consistent with the spill time window and matching with an MRD track. The matching can be with an MRD 3D track and with an MRD first-layer hit (see section 4.2.4). In case of many candidates, the most energetic track in MRD is assumed to be the muon. This event selection based on muon detection is dominated by CCQE interactions as shown in Table 6.1. 13% of the events in the selection are Nπ+DIS, the ones which are the goal of this analysis.

SciBar tracks that do not have a starting point in the fiducial volume or are outside a 100 ns time window with respect to the muon are not used in the analysis in order to reduce background tracks. After this selection 10 583 data and 409 555 MC events are kept. These number of events are used to normalize MC in all plots presented in this chapter. No additional cuts are applied.

[1]The uncertainties on the K2K neutrino flux come from the difficulties on the estimation of the primary proton beam intensity and proton targeting efficiency.

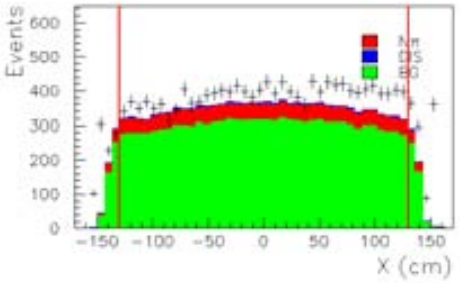

Figure 6.1: X position distribution of muon starting point. Red lines show the fiducial cut.

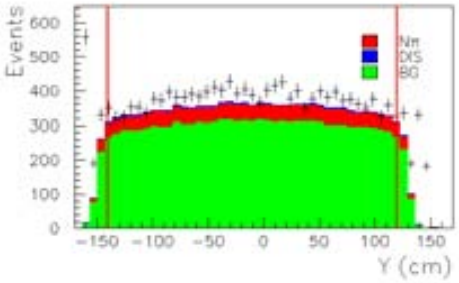

Figure 6.2: Y position distribution of muon starting point. Red lines show the fiducial cut.

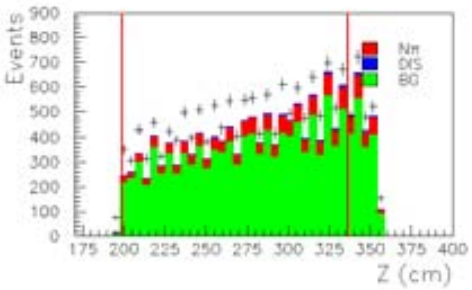

Figure 6.3: Z position distribution of muon starting point. Red lines show the fiducial cut.

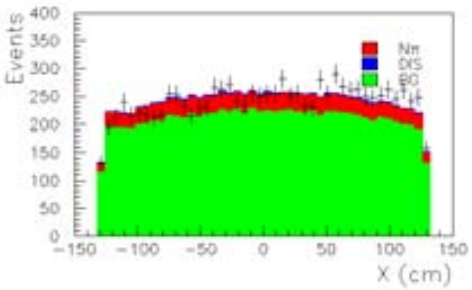

Figure 6.4: X position distribution of muon starting point after the fiducial cut.

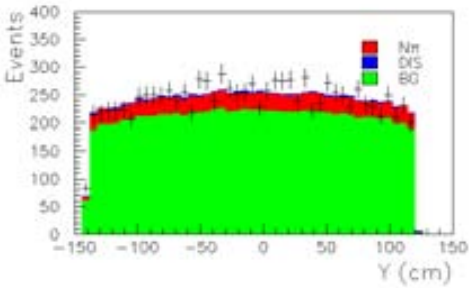

Figure 6.5: Y position distribution of muon starting point after the fiducial cut.

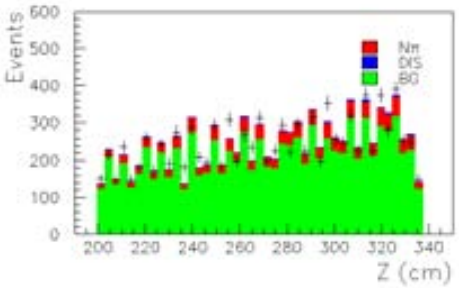

Figure 6.6: Z position distribution of muon starting point after the fiducial cut.

Interaction	% in the sample
CC QE	51%
CC 1π	33%
CC Nπ+DIS	13%
CC η,K	1%
NC	2%

Table 6.1: Data sample composition based on NEUT.

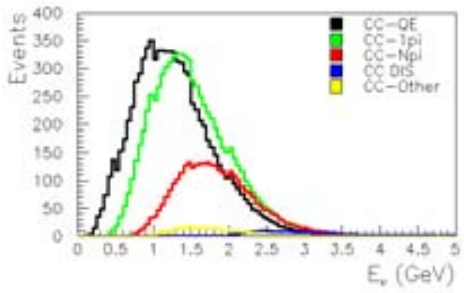

Figure 6.7: Simulated neutrino energy distributions for the different CC interactions.

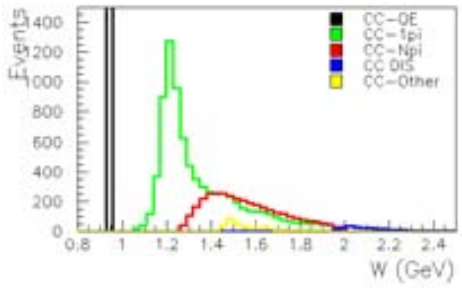

Figure 6.8: Simulated hadronic mass (W) distributions for the different CC interactions.

Based on the NEUT MC, 99.5% of Nπ interactions are produced at energies above 0.9 GeV (Fig. 6.7). The hadronic mass distribution (Fig. 6.8) shows how this interaction overlaps with single pion making it difficult to disentangle each reaction by simple muon kinematics. One can see how single pion and multi-pion also overlaps in other kinematic distributions as the Bjorken $x = -q^2/(P_p \cdot q)$ and $y = (P_p \cdot q)/(P_p \cdot P_\nu)$ variables, where q is the transfer four-momentum, P_p is the nucleon four-momentum and P_ν is the neutrino four-momentum (Figs. 6.9 and 6.10).

After selecting those events with a muon (Figs. 6.11 and 6.12), the statistics is reduced to about a half, loosing mainly low neutrino energy events (Figs. 6.13 and 6.14). Observables such as the energy and angle of the muon do not show a clear region where to disentangle Nπs from the other CC interactions (Fig. 6.15), but there is a tendency of producing muons of low energy and high angle. This information will be used later in this chapter to identify Nπ events.

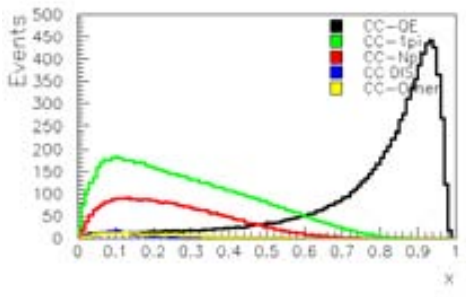

Figure 6.9: Simulated Bjorken x distributions for the different CC interactions.

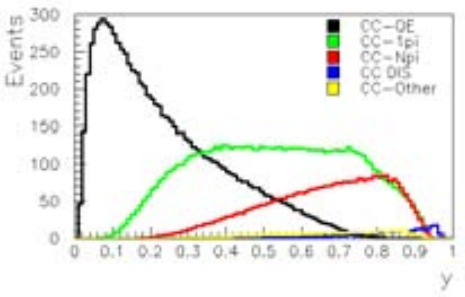

Figure 6.10: Simulated Bjorken y distributions for the different CC interactions.

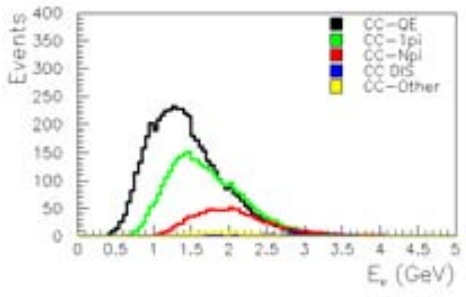

Figure 6.11: Neutrino energy distributions for events with a reconstructed muon in MRD.

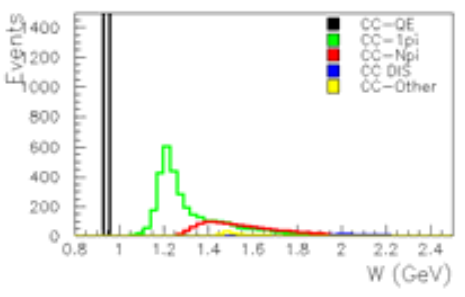

Figure 6.12: Hadronic mass distributions for events with a reconstructed muon in MRD.

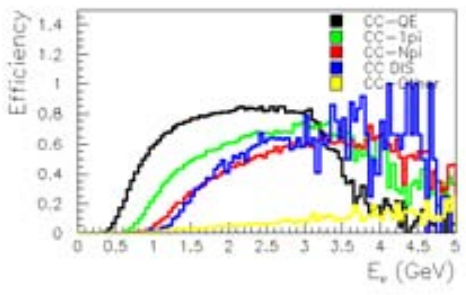

Figure 6.13: Efficiency of selecting events with a reconstructed muon in MRD as function of the neutrino energy.

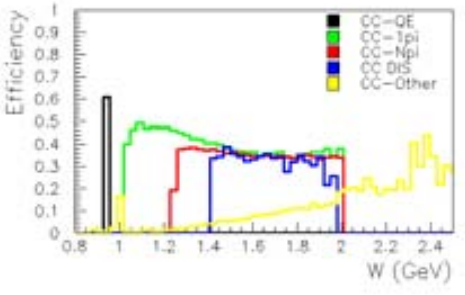

Figure 6.14: Efficiency of selecting events with a reconstructed muon in MRD as function of the hadronic mass.

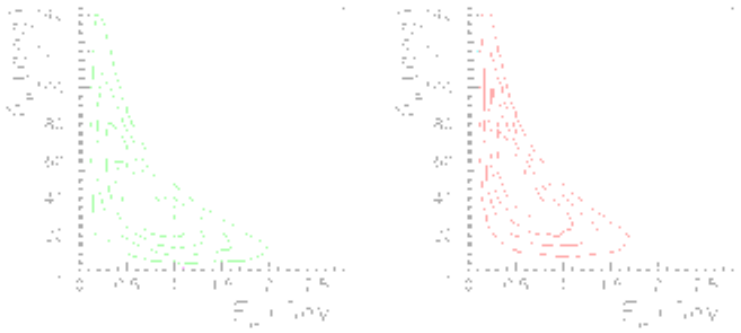

Figure 6.15: Energy versus angle of muon producing a track in MRD. From left to right: quasi-elastic, single-pion and Nπ.

6.2 Observables

The sensitivity of several observables to distinguish signal (Nπ+DIS) from background has been investigated. The observables used for events with more than one track are:

- The number of tracks on time with the muon and starting in the fiducial volume (Fig. 6.16).

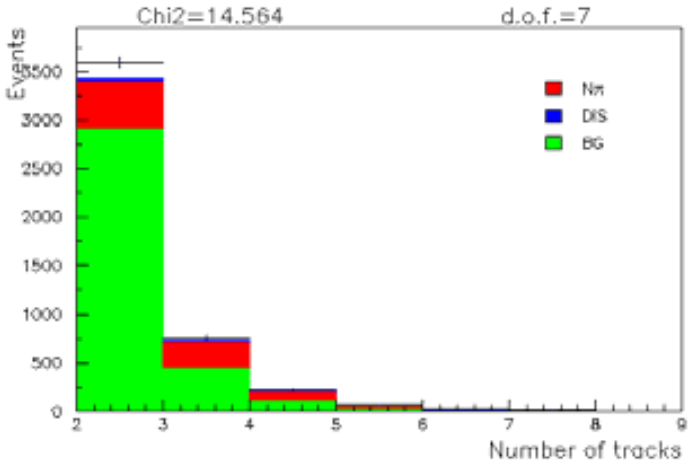

Figure 6.16: Number of tracks starting in the fiducial volume.

- The hit energy deposited in SciBar calculated by adding all hits in the fiducial volume in a 100 ns time window coincidence with respect to the muon (Fig. 6.17).

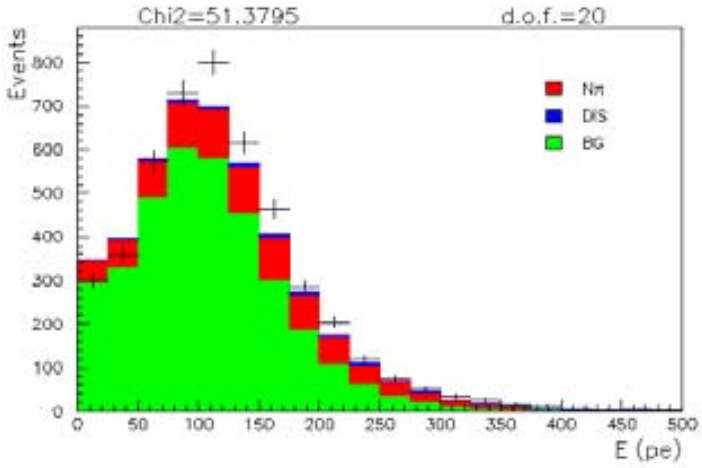

Figure 6.17: Sum of hits energy in the fiducial volume on time with the muon.

- The muon energy and angle to get kinematic information of the interaction (Figs. 6.18 and 6.19).

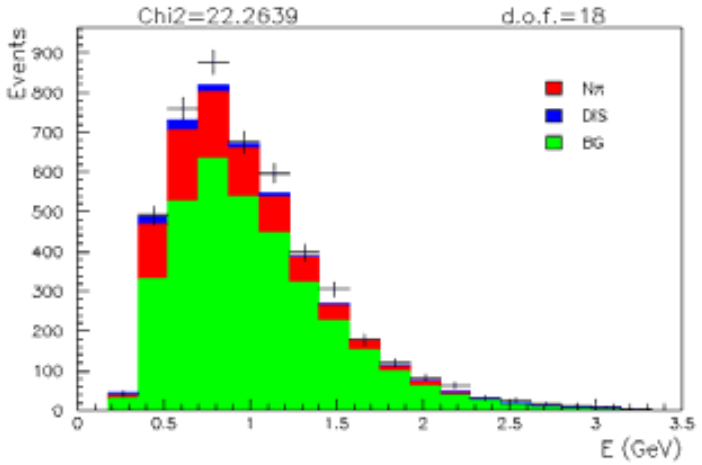

Figure 6.18: Muon energy.

- The hadronic energy as the sum of the energy of all tracks in the hadronic region (Fig. 6.20). In a reference system where the neutrino defines the z direction and the muon is in the xz plane with positive x, one defines the hadronic region as that with negative x (Fig. 6.21). This variable has an intrinsic cut since

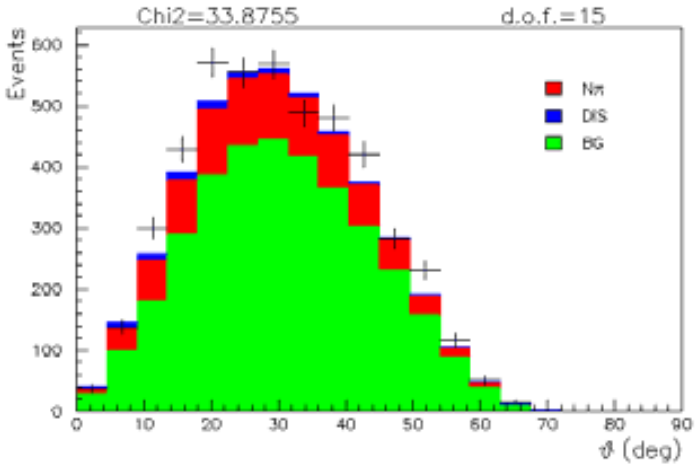

Figure 6.19: Muon angle.

one needs at least another particle apart of the muon to calculate the hadronic energy.

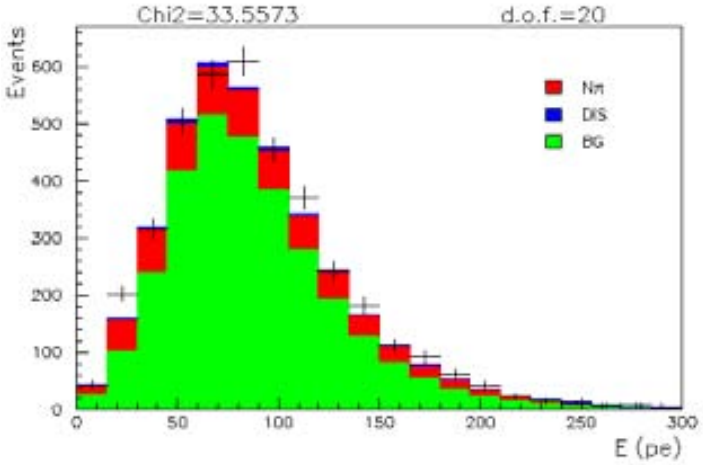

Figure 6.20: Hadronic energy.

- The angle ($\Delta\theta_p$) between the predicted proton for a CCQE interaction and the observed one (Fig. 6.22). The observed proton is taken as the longest track with common vertex with the muon. The angle $\Delta\theta_p$ is calculated as:

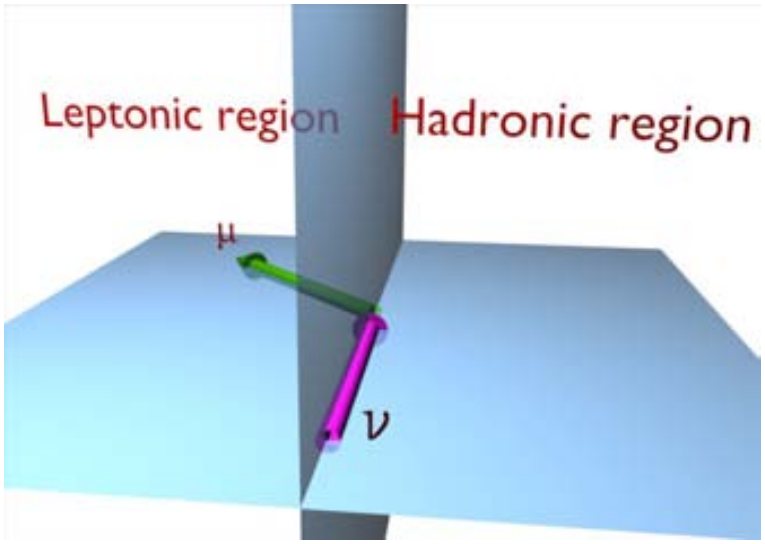

Figure 6.21: Hadronic region.

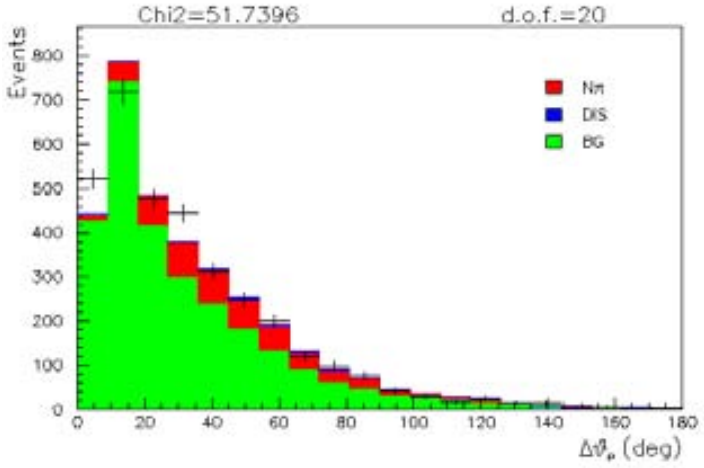

Figure 6.22: Angle between predicted CCQE proton and longest track with common vertex with the muon.

$$\Delta\theta_p = \arccos\left(\frac{\vec{P}_{expected}\cdot\vec{P}_{observed}}{|\vec{P}_{expected}|\cdot|\vec{P}_{observed}|}\right) \tag{6.1}$$

were the momentum of the predicted proton $\vec{P}_{expected}$ for a CCQE interaction can be calculated as

$$\vec{P}_{expected} = (-P_{\mu x}, -P_{\mu y}, E_{\nu}^{reco} - P_{\mu z}\cos(\theta_{\mu})) \tag{6.2}$$

where $P_{\mu x}$, $P_{\mu y}$ and $P_{\mu z}$ are the muon momentum components and θ_{μ} is the muon angle respect to the Z axis. The neutrino energy is calculated as

$$E_{\nu}^{reco} = \frac{m_n E_{\mu} - (m_n^2 - m_p^2 + m_{\mu}^2)/2}{m_n - E_{\mu} + |\vec{P}_{\mu}|\cos(\theta_{\mu\nu})} \tag{6.3}$$

where m_n, m_p and m_{μ} are the neutron, proton and muon mass, E_{μ} and p_{μ} are the muon energy and momentum and $\theta_{\mu\nu}$ is the angle between the muon and the neutrino.

The observable used for events with just one track is the reconstructed neutrino energy assuming a CCQE interaction (see Eqn. 6.3 and Fig. 6.23). This distribution has some sensitivity to signal in a sample that is 62.7% QE.

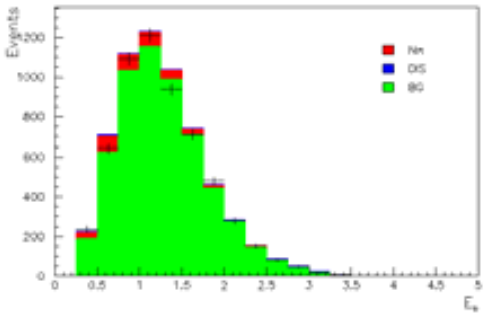

Figure 6.23: Reconstructed neutrino energy assuming CCQE for one track events.

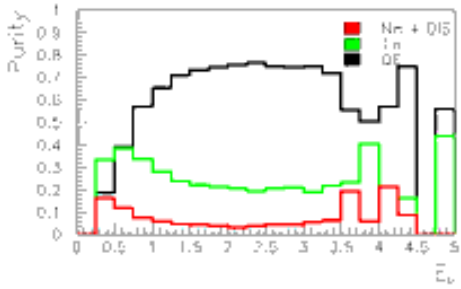

Figure 6.24: Main interaction purities in the CCQE reconstructed neutrino energy distribution for one track events.

The purity of the main CC interactions for each distribution mentioned above are shown in figures from 6.24 to 6.31. The purities from the number of tracks distribution (Fig. 6.26) shows how the more tracks has the event, the more probable is that the event is signal. The purity distribution from the sum of energy hits shows that signal events accumulate at high energies. The purity distribution from muon energy and angle shows that single pion and multi-pion events prefer low energy and forward muons to allow meson production. Even though high signal purities at high muon angles were expected according to MC, it is not seen since the detector is not sensitive enough to angles above 60°. The purity distribution from hadronic energy shows how signal has high hadronic energy depositions produced by charged pions, as well as very low hadronic energy depositions produced by neutral pions, which decay photons may scape from the detector or be detected in the leptonic region (see fig. 6.25). The purity

distribution from $\Delta\theta_p$ show how good is this distribution to identify CCQE events. Finally, the purity distribution from the reconstructed neutrino energy assuming CCQE has sensitivity to select signal events even though it shows that assuming CCQE for the energy reconstruction makes that signal fakes low energy neutrino (Fig. 6.24).

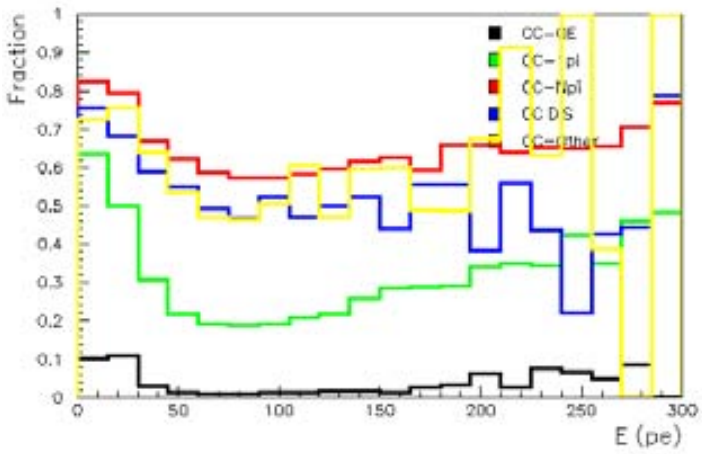

Figure 6.25: Fraction of events with at least one π^0 versus reconstructed hadronic energy. One can see how events with π^0 populate the low hadronic energy region.

6.3 Likelihood Asymmetry

To improve the signal sensitivity, we have constructed a likelihood asymmetry function ($\mathcal{A}$) to obtain a high sensitivity variable. $\mathcal{A}$ uses the energy deposited in SciBar, muon energy, muon angle, hadronic energy, number of tracks and $\Delta\theta_p$.

Because hadronic energy and $\Delta\theta_p$ need more than one track to be calculated and the one track sample is 62.7% QE and 6.6% signal, $\mathcal{A}$ will not use events with only one track. The one track sample will be used during the fitting procedure.

From the MC distributions of the observables the probability density functions (PDF, $\mathcal{P}$) of these variables are derived for signal (labeled as $N\pi$) and background (labeled as BG) events. The signal and BG likelihoods are obtained by multiplying the six PDF's

$$\mathcal{L}^{N\pi} = \mathcal{P}^{N\pi}_{Ntr} \cdot \mathcal{P}^{N\pi}_{Ehit} \cdot \mathcal{P}^{N\pi}_{E\mu} \cdot \mathcal{P}^{N\pi}_{\theta\mu} \cdot \mathcal{P}^{N\pi}_{Ehad} \cdot \mathcal{P}^{N\pi}_{\Delta\theta_p} \quad (6.4)$$

$$\mathcal{L}^{BG} = \mathcal{P}^{BG}_{Ntr} \cdot \mathcal{P}^{BG}_{Ehit} \cdot \mathcal{P}^{BG}_{E\mu} \cdot \mathcal{P}^{BG}_{\theta\mu} \cdot \mathcal{P}^{BG}_{Ehad} \cdot \mathcal{P}^{BG}_{\Delta\theta_p} \quad (6.5)$$

The likelihood asymmetry function ($\mathcal{A}$) for each event is constructed as:

$$\mathcal{A} = \frac{\mathcal{L}^{N\pi} - \mathcal{L}^{BG}}{\mathcal{L}^{N\pi} + \mathcal{L}^{BG}} \quad (6.6)$$

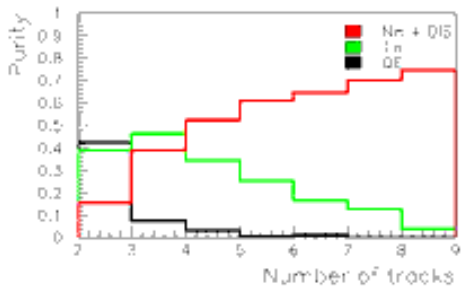

Figure 6.26: Main interaction purities in the number of tracks distribution.

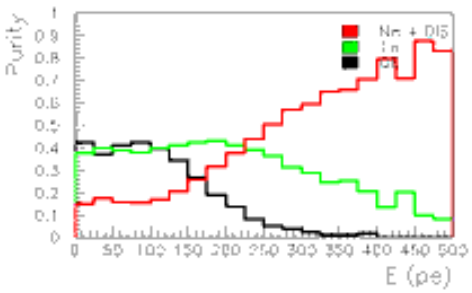

Figure 6.27: Main interaction purities in the sum of hits energy distribution.

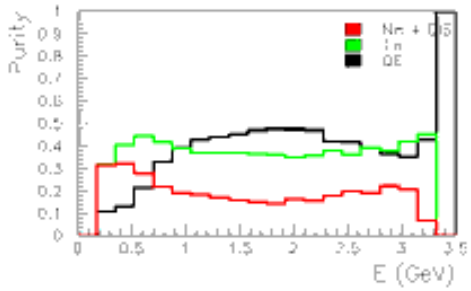

Figure 6.28: Main interaction purities in the muon energy distribution.

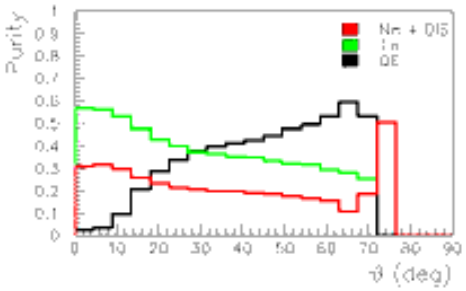

Figure 6.29: Main interaction purities in the muon angle distribution.

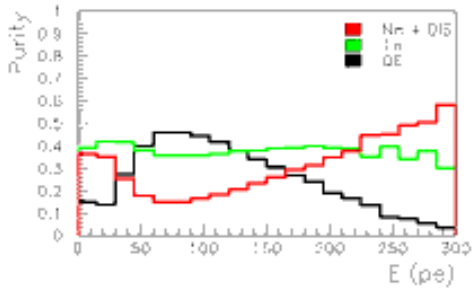

Figure 6.30: Main interaction purities in the hadronic energy distribution.

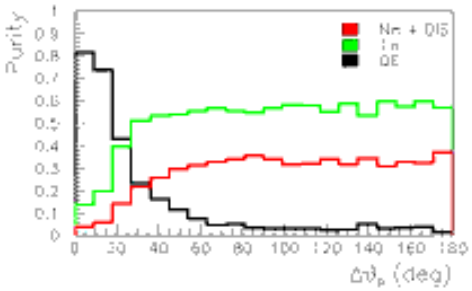

Figure 6.31: Main interaction purities in the $\Delta\theta_p$ distribution.

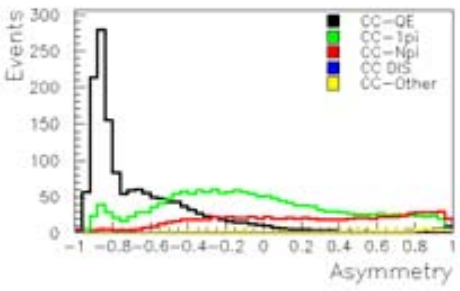

Figure 6.32: Asymmetry ($\mathcal{A}$) distribution.

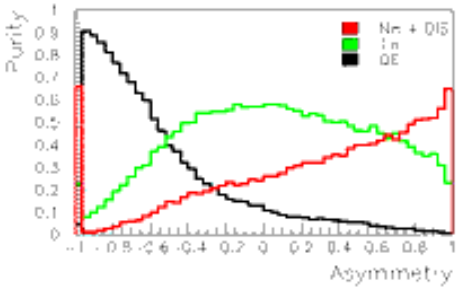

Figure 6.33: Main interaction purities in $\mathcal{A}$. Black is for QE, green for single pion and red for Nπ.

The $\mathcal{A}$ distribution (Fig. 6.32) and the purity of the main CC interactions (Fig. 6.33) show a good behavior. The CCNπ purity concentrates at high $\mathcal{A}$ values, CCQE at low $\mathcal{A}$ values and CC single pion events at middle $\mathcal{A}$ values.

6.3.1 E_ν binning

In order to make the measurement for two neutrino energy regions, an E_ν reconstruction method has been developed. Its purpose is just to divide events in two samples, one rich in signal events from high energetic neutrinos and another rich in signal events from low energetic neutrinos. The neutrino energy in GeV is calculated as $E_\nu^{reco} = E_\mu + f(E_{hits})$ where $f(E_{hits}) = (E_{hits} + 165)/260$ and E_{hits} is the energy sum up in photoelectrons of those hits not produced by the muon but are on-time with it in a 100 ns time window. To adjust this function the non-QE sample has been used (Fig. 6.34). This sample is defined as those events that has $\Delta\theta_p > 20°$. The empirical function has been adjusted to get the best energy resolution based on MC (Fig. 6.35).

E_ν^{reco} allows the division of reconstructed events sample with more than one track into low energy sample (Low) and high energy sample (High). It is also used to divide the MC true signal into a low energy signal ($N\pi_L$) and an high energy signal ($N\pi_H$). The $E_{\nu\text{reco}}$ value has been chosen to be 2.55 GeV to equalize the sensitivity in both samples, low and high. Figure 6.36 shows the significance difference between both samples

$$\Delta s = \frac{N\pi_{\text{High}}}{\sqrt{\text{All}_{\text{High}}}} - \frac{N\pi_{\text{Low}}}{\sqrt{\text{All}_{\text{Low}}}} \tag{6.7}$$

were $N\pi_{\text{High}}$ ($N\pi_{\text{Low}}$) and All_{High} (All_{Low}) are the signal and total number of events in the high (low) energy sample and in the MRD selection.

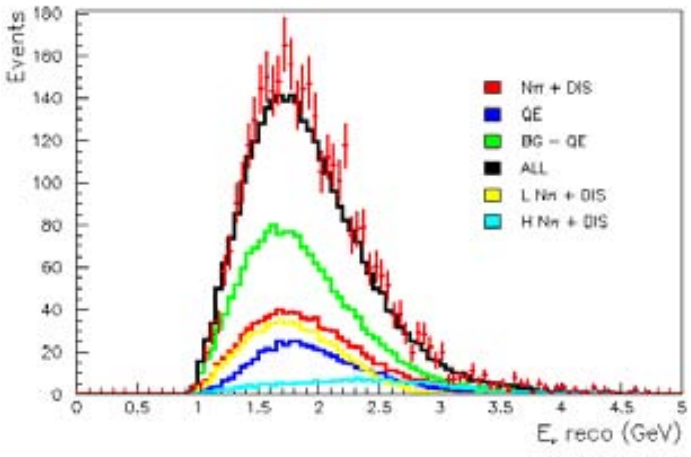

Figure 6.34: Neutrino energy reconstruction for non-QE events. The non-QE sample is defined as those events with $\Delta\theta_p > 20°$. Red points are data. Signal contribution is plot in red, QE is in blue and other background contributions are plot in green. High and low energy components of the signal are also drawn in light blue and yellow respectively.

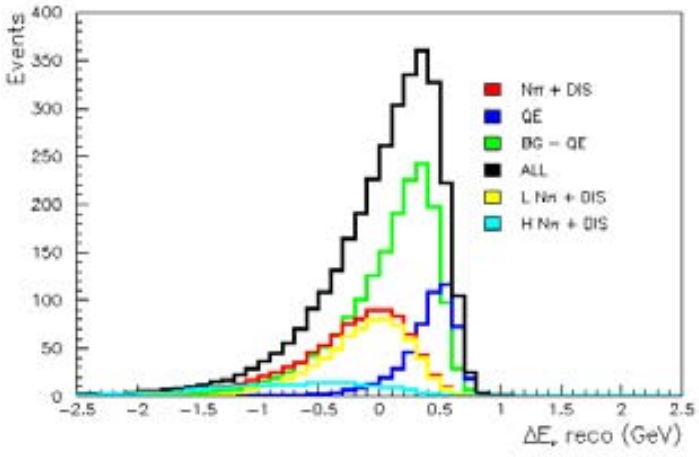

Figure 6.35: Neutrino energy reconstruction minus true energy for non-QE events.

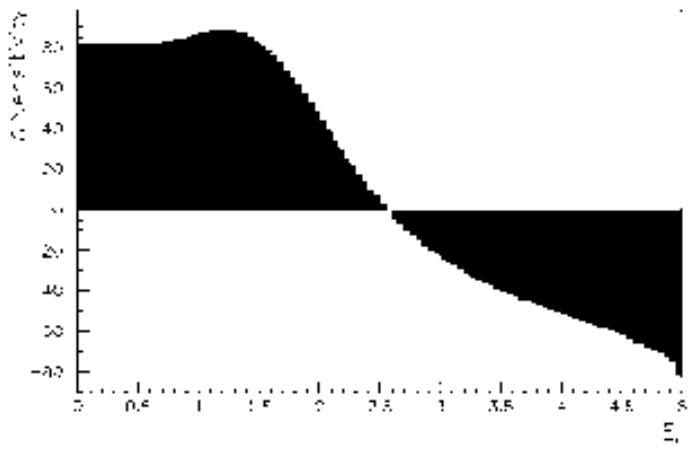

Figure 6.36: $\Delta Sensitivity$ distribution used to choose the $E_{\nu\text{reco}}$ cut value.

The contribution of each interaction in each sample is shown in table 6.2.

	1 track sample	**Low E sample**	**High E sample**
Number of expected events	5983	3868	477
QE	62.6%	33.9%	36.0%
Nπ_L	5.5%	17.7%	4.7%
Nπ_H	1.1%	3.8%	19.5%
Other	30.7%	44.6%	39.8%

Table 6.2: Composition of the three samples used in the fit according to MC.

For each selection we construct the probability distributions $\mathcal{P}_{\text{Low}}$ (Figs. 6.37 to 6.42) and $\mathcal{P}_{\text{High}}$ (Figs. 6.43 to 6.48), and with them one calculates the likelihood asymmetry distribution $\mathcal{A}_{\text{Low}}$ (Fig. 6.49) and $\mathcal{A}_{\text{High}}$ (Fig. 6.51). The asymmetries $\mathcal{A}_{\text{Low}}$ and $\mathcal{A}_{\text{High}}$ keep a good likelihood behavior (Figs. 6.50 and 6.52).

6.4 Fitting procedure

The complete MRD sample is used to fit MC to data. For one track events the neutrino energy distribution is used, and for events of more than one track $\mathcal{A}_{\text{Low}}$ and $\mathcal{A}_{\text{High}}$ distributions are used.

For the one track sample the neutrino energy distribution has been used in order to gain energy sensitivity for Nπ since $N\pi_L$ events accumulate at low energies unlike $N\pi_H$.

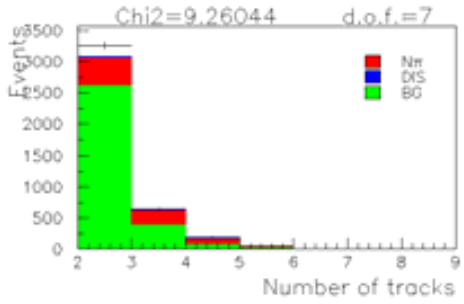

Figure 6.37: Number of tracks starting in the fiducial volume for the low E sample ($\mathcal{P}_{Ntr,L}$).

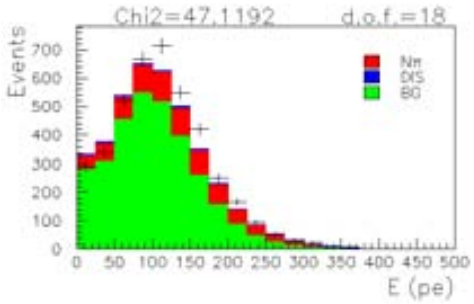

Figure 6.38: Sum of hits energy in the fiducial volume on time with the muon for the low E sample ($\mathcal{P}_{Ehit,L}$).

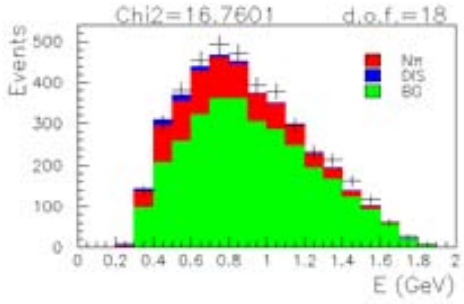

Figure 6.39: Muon energy for the low E sample ($\mathcal{P}_{E\mu,L}$).

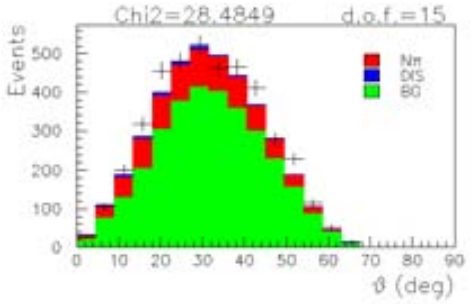

Figure 6.40: Muon angle for the low E sample ($\mathcal{P}_{\theta\mu,L}$).

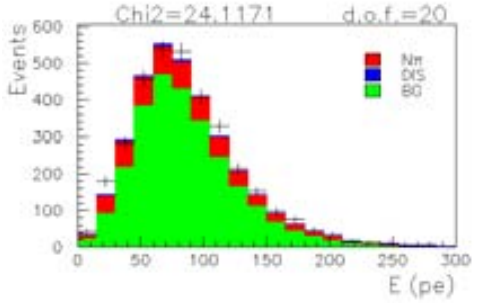

Figure 6.41: Hadronic energy for the low E sample ($\mathcal{P}_{Ehad,L}$).

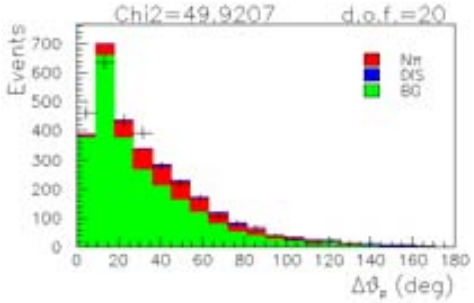

Figure 6.42: Angle between predicted QE proton and longest track with common vertex with the muon for the low E sample ($\mathcal{P}_{\Delta\theta_p,L}$).

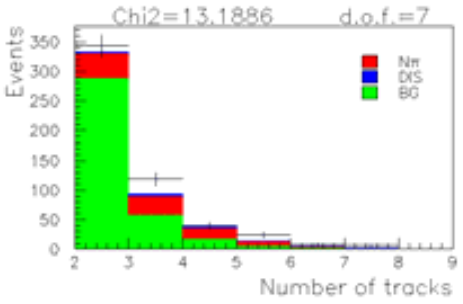

Figure 6.43: Number of tracks starting in the fiducial volume for the high E sample ($\mathcal{P}_{Ntr,H}$).

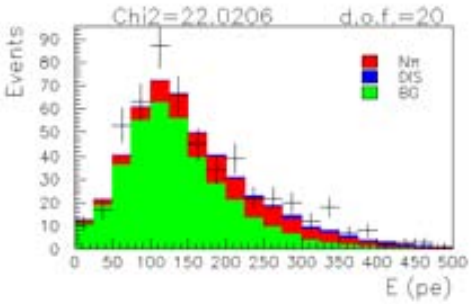

Figure 6.44: Sum of hits energy in the fiducial volume on time with the muon for the high E sample ($\mathcal{P}_{Ehit,H}$).

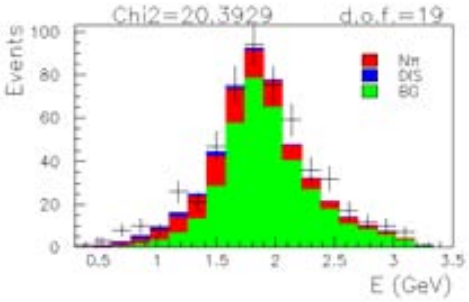

Figure 6.45: Muon energy for the high E sample ($\mathcal{P}_{E\mu,H}$).

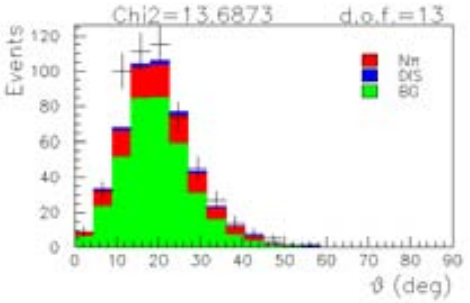

Figure 6.46: Muon angle for the high E sample ($\mathcal{P}_{\theta\mu,H}$).

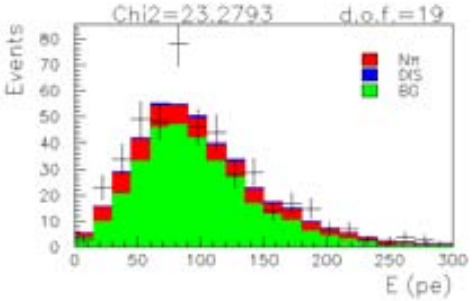

Figure 6.47: Hadronic energy for the high E sample ($\mathcal{P}_{Ehad,H}$).

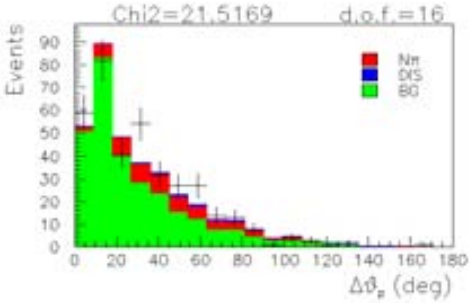

Figure 6.48: Angle between predicted QE proton and longest track with common vertex with the muon for the high E sample ($\mathcal{P}_{\Delta\theta_p,H}$).

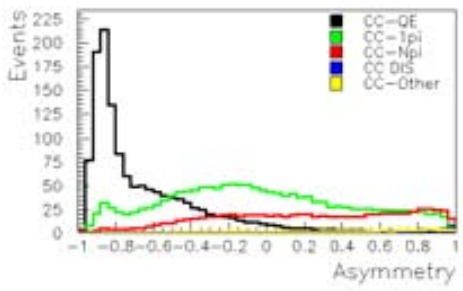

Figure 6.49: $\mathcal{A}$ distribution for low neutrino energies.

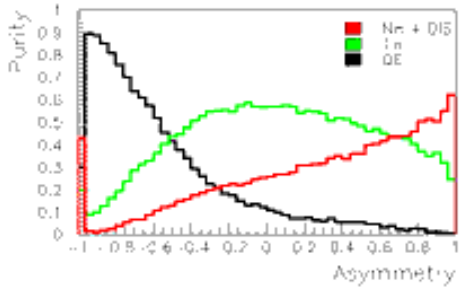

Figure 6.50: Main interaction purities in $\mathcal{A}$ distribution for low neutrino energies.

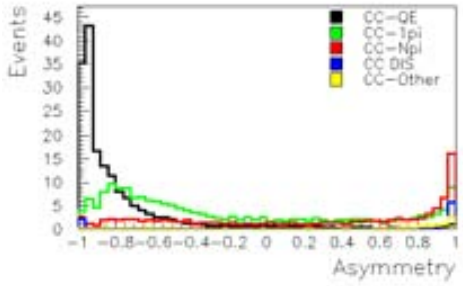

Figure 6.51: $\mathcal{A}$ distribution for high neutrino energies.

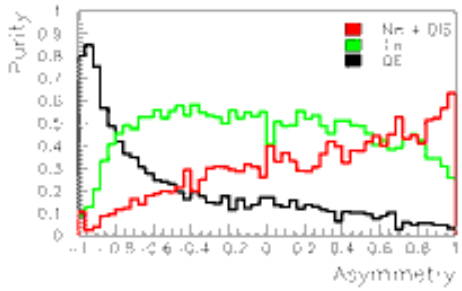

Figure 6.52: Main interaction purities in $\mathcal{A}$ distribution for high neutrino energies.

This neutrino energy has been calculated assuming CCQE kinematics as in section 6.2 equation 6.3:

$$E_\nu^{reco} = \frac{m_n E_\mu - (m_n^2 - m_p^2 + m_\mu^2)/2}{m_n - E_\mu + |\vec{P}_\mu| \cos(\theta_{\mu\nu})}$$

The three distributions are fitted simultaneously minimizing the value of χ^2 (Eq. 6.8 and 6.9). The χ^2 value is calculated from the Poisson distribution since there are many bins in the fit that have low statistics. On the other hand in order to calculate the DATA-MC agreement for observable plots the χ^2 value is calculated from the Gauss distribution since the statistics are higher (Eq. 6.10).

$$\chi^2 = \sum_i \chi^2_i(\mathcal{A}_{\rm Low}) + \sum_j \chi^2_j(\mathcal{A}_{\rm High}) + \sum_k \chi^2_k(E^{1T}_\nu) \tag{6.8}$$

$$\chi^2_{bin} = 2 \cdot (MC_{RW} - DATA + DATA \cdot \ln(DATA/MC_{RW}))|_{bin} \tag{6.9}$$

$$\chi^2 = \sum_{bin} \frac{(DATA - MC_{RW})^2}{\sigma^2_{DATA}}\Big|_{bin} \tag{6.10}$$

MC_{RW} is the re-weighted MC with the fit parameters:

$$\begin{aligned} MC_{RW} &= \text{Norm} \cdot (\text{QE} + f_{\text{N}\pi\text{L}} \cdot \text{N}\pi_{\text{L}} + f_{\text{N}\pi\text{H}} \cdot \text{N}\pi_{\text{H}} + f_{\text{OT}} \cdot \text{Other}) \\ QE &= QE^{+T} + f_{1T/+T} \cdot QE^{1T} \\ N\pi_L &= N\pi_L^{+T} + f_{1T/+T} \cdot N\pi_L^{1T} \\ N\pi_H &= N\pi_H^{+T} + f_{1T/+T} \cdot N\pi_H^{1T} \\ Other &= OT^{+T} + f_{1T/+T} \cdot OT^{1T} \end{aligned} \tag{6.11}$$

where Norm, $f_{N\pi L}$, $f_{N\pi H}$, f_{OT} and $f_{1T/+T}$ are the fit parameters. X^{1T} names the one track sample and X^{+T} names the sample with more than one track. After the one-track re-weighting, QE is defined as the number of MC CCQE reconstructed events. $N\pi_L$ is the number of MC signal reconstructed events with $E_{\nu\text{true}}$ under the $E_{\nu\text{reco}}$ cut. $N\pi_H$ is the number of MC signal reconstructed events with $E_{\nu\text{true}}$ over the $E_{\nu\text{reco}}$ cut. *Other* is the number of other MC reconstructed events. The *Other* events are 90.3% single pion, 5.0% single K or η and 4.7% neutral current interacions.

The fitting factor $f_{1T/+T}$ is applied to the one track sample as a method to propagate the error in tracking efficiencies in that particular sample. This method has been used in several other SciBar analysis and it is kept here also to maintain the compatibility of the results.

With the fit information and the amount of expected events by NEUT MC one can get the Nπ relative cross sections $\sigma_{N\pi}/\sigma_{QE}$ for neutrino energies above the kinematic threshold that allows the production of two or more pions. This energy is:

$$E_\nu^{\text{Thres.}} = \frac{m_N^2 - (m_N - m_\mu - 2 \cdot m_\pi)^2}{2 \cdot (m_N - m_\mu - 2 \cdot m_\pi)} = 0.50 \text{ GeV} \tag{6.12}$$

where m_N, m_μ and m_π are the nucleon, the muon and the pion masses respectively.

Applying this threshold and using the fit and NEUT information we calculate the $\sigma_{N\pi}/\sigma_{QE}$ relative cross sections as:

	$N\pi$		QE	
	Low E	**High E**	**Low E**	**High E**
1T	13074.	2604.	144694.	3945.
+T	28076.	9573.	56528.	2209.

Table 6.3: Number of MC events in the QE and Nπsamples used to calculate the weight factors.

$$\begin{aligned} \left.\frac{\sigma_{N\pi}}{\sigma_{QE}}\right|_{\text{Low}} &= f_{N\pi L}\left.\frac{N\pi_L}{QE_L}\right|^{\text{NEUT}}_{0.5-2.5\text{ GeV}}\frac{\mathcal{W}_{N\pi,L}}{\mathcal{W}_{QE,L}} \\ \left.\frac{\sigma_{N\pi}}{\sigma_{QE}}\right|_{\text{High}} &= f_{N\pi H}\left.\frac{N\pi_H}{QE_H}\right|^{\text{NEUT}}_{2.5-5\text{ GeV}}\frac{\mathcal{W}_{N\pi,H}}{\mathcal{W}_{QE,H}} \end{aligned} \tag{6.13}$$

where $f_{N\pi L}$ ($f_{N\pi H}$) is the fitting factor for low (high) energy signal events, $N\pi_L$ ($N\pi_H$) and QE_L (QE_H) are the number of signal and CCQE NEUT MC events with $E_{\nu\text{true}}$ under (over) the $E_{\nu\text{reco}}$ cut, and $\mathcal{W}_{N\pi L}$, $\mathcal{W}_{N\pi H}$, $\mathcal{W}_{QEL}$ and $\mathcal{W}_{QEH}$ are weight factors to take into account the one track fit parameter $f_{1T/+T}$. The weight factors are calculated as

$$\mathcal{W}_{X,i} = \frac{X_i^{+T} + f_{1T/+T}\cdot X_i^{1T}}{X_i^{+T} + X_i^{1T}} \qquad (X = N\pi, QE; i = L, H) \tag{6.14}$$

where $X = (N\pi, QE)$ is the number of signal and CCQE reconstructed events in the sample, $i = L, H$ states energy sample and $1T, +T$ states one track or many tracks sub-sample (Table 6.3).

6.5 Measurement of the Multi-pion cross section

Fitting MC to data as described in section 6.4, one obtain the fit parameters Norm, $f_{N\pi L}$, $f_{N\pi H}$, f_{OT} and $f_{1T/+T}$ (Table 6.4). Among these parameters, the value of Norm parameter has no physical information. It just shows the relation between data and MC statistics. On the other hand, $f_{N\pi L}$ and $f_{N\pi H}$ tells with which factor the amount of MC true signals (Nπ_L and Nπ_H) has to be multiplied to reproduce the data. f_{OT} is the re-weighting factor for other interactions apart of Nπ, DIS and QE. And $f_{1T/+T}$ take account of tracking efficiencies.

From the fit values one can see that the deviation between signal and MC is about 2σ without systematics and from the correlation matrix (Table 6.5) one can see that $f_{N\pi L}$ and $f_{N\pi H}$ have a 19% coorelation. That makes that the measurement of $\sigma_{N\pi}/\sigma_{QE}$

Fit factor	**Value**
Norm	0.0256 ± 0.0009
$f_{N\pi L}$	0.74 ± 0.18
$f_{N\pi H}$	1.47 ± 0.23
f_{OT}	1.17 ± 0.10
$f_{1T/+T}$	0.93 ± 0.02

Table 6.4: The fit with the three distributions has a $\chi^2 = 150$ for 110 degrees of freedom. Before the fit $\chi^2 = 178$.

Corr.	$f_{N\pi L}$	$f_{N\pi H}$	f_{OT}	$f_{1T/+T}$
Norm	19%	-30%	-70%	-60%
$f_{N\pi L}$		-19%	-73%	28%
$f_{N\pi H}$			9%	30%
f_{OT}				2%

Table 6.5: Fit correlation matrix.

for high and low neutrino energies are 35% correlated. On the other hand one can see that $f_{N\pi L}$ and f_{OT} are highly correlated, since f_{OT} weights mainly single pions and single pions are kinetically and topologically very similar to low energy Nπ.

$$\begin{aligned} \left.\frac{\sigma_{N\pi}}{\sigma_{QE}}\right|_{\text{Low}}^{\text{NEUT}} &= 0.3909 \pm 0.0013(\text{stat.}) \\ \left.\frac{\sigma_{N\pi}}{\sigma_{QE}}\right|_{\text{High}}^{\text{NEUT}} &= 2.57 \pm 0.03(\text{stat.}) \end{aligned} \tag{6.15}$$

With the fit parameters and the relative cross sections given by NEUT (Eq. 6.15) one can apply equation 6.13 to obtain the following relative cross sections measurement:

$$\begin{aligned} \left.\frac{\sigma_{N\pi}}{\sigma_{QE}}\right|_{\text{Low}} &= 0.30 \pm 0.07 \\ \left.\frac{\sigma_{N\pi}}{\sigma_{QE}}\right|_{\text{High}} &= 3.9 \pm 0.6 \end{aligned} \tag{6.16}$$

After the fit one can check the improvement on MC-Data agreement by looking how the χ^2 of the basic observables decreases (Tbl. 6.6). χ^2 is calculated as

$$\chi^2 = \sum_{bin} \left.\frac{(DATA - MC_{RW})^2}{\sigma^2_{DATA}}\right|_{bin} \tag{6.17}$$

Distribution	χ^2 **Before fit**	χ^2 **After fit**	**d.o.f**
Number of tracks	13.2	2.9	7
Hits energy	51.4	41.6	20
Muon energy	22.3	11.0	18
Muon angle	33.9	26.2	15
Hadronic energy	33.6	35.6	20
$\Delta\theta p$	51.7	63.9	20
Total	206.1	181.2	100

Table 6.6: Values of χ^2 for all studied distributions before and after the fit. These are not the fitted distributions but one can check the improvement on MC-Data agreement by looking how the χ^2 of these observables decreases. The χ^2 values are high because they do not include systematic errors.

6.6 Consistency check

The Bodek correction has not been applied to avoid a biased measurement in the previous results. As consistency check, the analysis has been repeated applying the Bodek correction.

Comparing the relative cross section given by NEUT with the Bodek correction (Eqn. 6.18) and without (Eqn. 6.15), one can see how this effect reduce the amount of signal in MC by a 33% in $\sigma_{N\pi}/\sigma_{QE}$ Low and a 24% in $\sigma_{N\pi}/\sigma_{QE}$ High.

$$\begin{aligned} \left.\frac{\sigma_{N\pi}}{\sigma_{QE}}\right|^{\text{NEUT}}_{\text{Low}} &= 0.2583 \pm 0.0010(\text{stat.}) \\ \left.\frac{\sigma_{N\pi}}{\sigma_{QE}}\right|^{\text{NEUT}}_{\text{High}} &= 1.97 \pm 0.03(\text{stat.}) \end{aligned} \tag{6.18}$$

The analysis performed including the Bodek correction gives higher values of the fitting parameters $f_{N\pi L}$ and $f_{N\pi H}$ (Table 6.7). This would mean that one has more Nπ in data than in MC but actually the fitting parameters are recovering the fraction of Nπ that the Bodek correction has reduce.

Therefore, the fit results leads to relative cross sections values (Eqn. 6.19) close to the standard measurement (Eqn. 6.16).

$$\begin{aligned} \left.\frac{\sigma_{N\pi}}{\sigma_{QE}}\right|_{\text{Low}} &= 0.30 \pm 0.07(\text{stat.}) \\ \left.\frac{\sigma_{N\pi}}{\sigma_{QE}}\right|_{\text{High}} &= 4.0 \pm 0.6(\text{stat.}) \end{aligned} \tag{6.19}$$

Fit factor	**Value**
Norm	0.0252 ± 0.0009
$f_{N\pi L}$	1.12 ± 0.28
$f_{N\pi H}$	2.00 ± 0.31
f_{OT}	1.22 ± 0.10
$f_{1T/+T}$	0.94 ± 0.02

Table 6.7: Fit result when including the Bodek correction. The fit with the three distributions gives a final χ^2 equal to 147 for 110 degrees of freedom.

Corr.	$f_{N\pi L}$	$f_{N\pi H}$	f_{OT}	$f_{1T/+T}$
Norm	15%	-30%	-69%	-60%
$f_{N\pi L}$		-24%	-71%	32%
$f_{N\pi H}$			11%	28%
f_{OT}				-0.6%

Table 6.8: Fit correlation matrix including the Bodek correction.

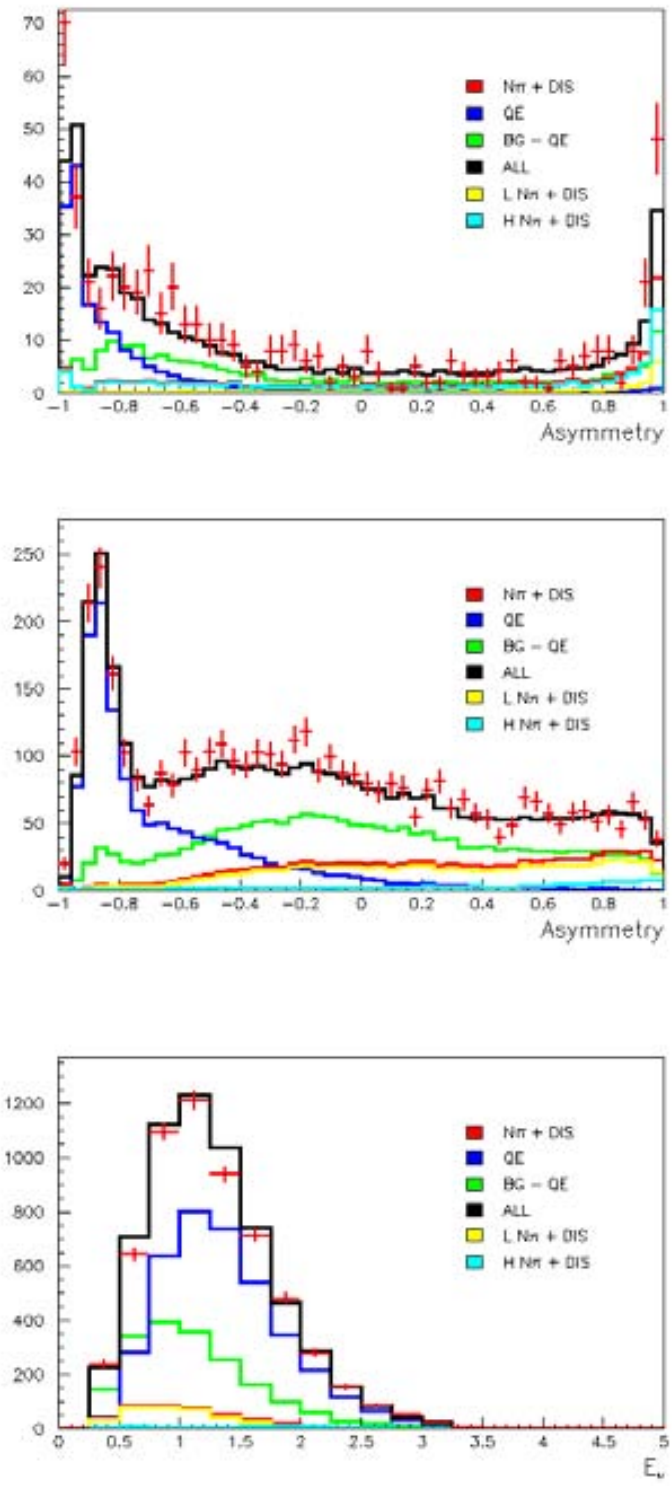

Figure 6.53: $\mathcal{A}_{\text{High}}$ (top), $\mathcal{A}_{\text{Low}}$ (middle) and E_ν^{1T} (bottom) distributions before the fit.

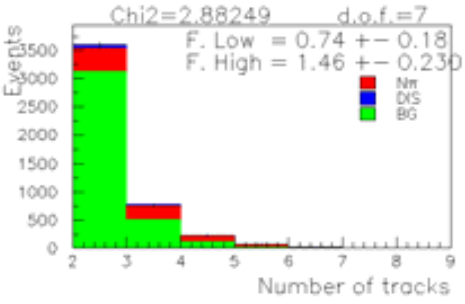

Figure 6.54: Number of tracks starting in the fiducial volume after the fit.

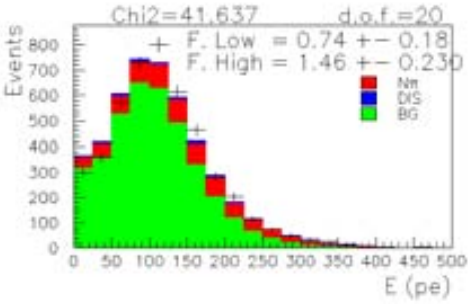

Figure 6.55: Sum of hits energy in the fiducial volume on time with the muon after the fit.

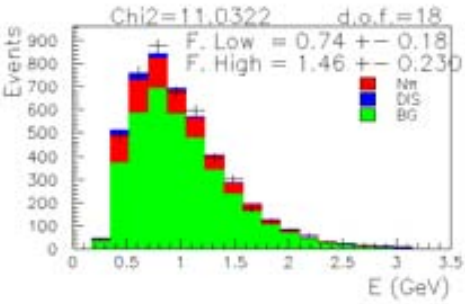

Figure 6.56: Muon energy after the fit.

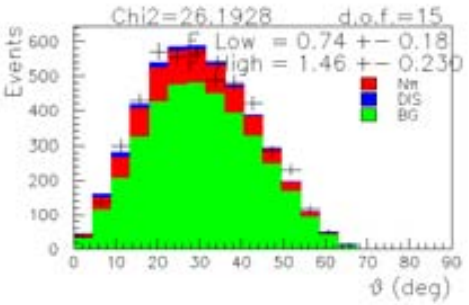

Figure 6.57: Muon angle after the fit.

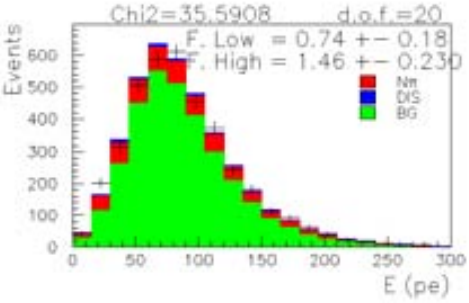

Figure 6.58: Hadronic energy after the fit.

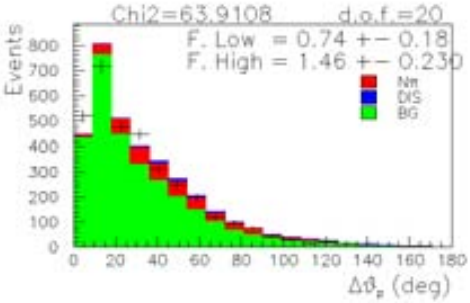

Figure 6.59: Angle between predicted QE proton and longest track with common vertex with the muon after the fit.

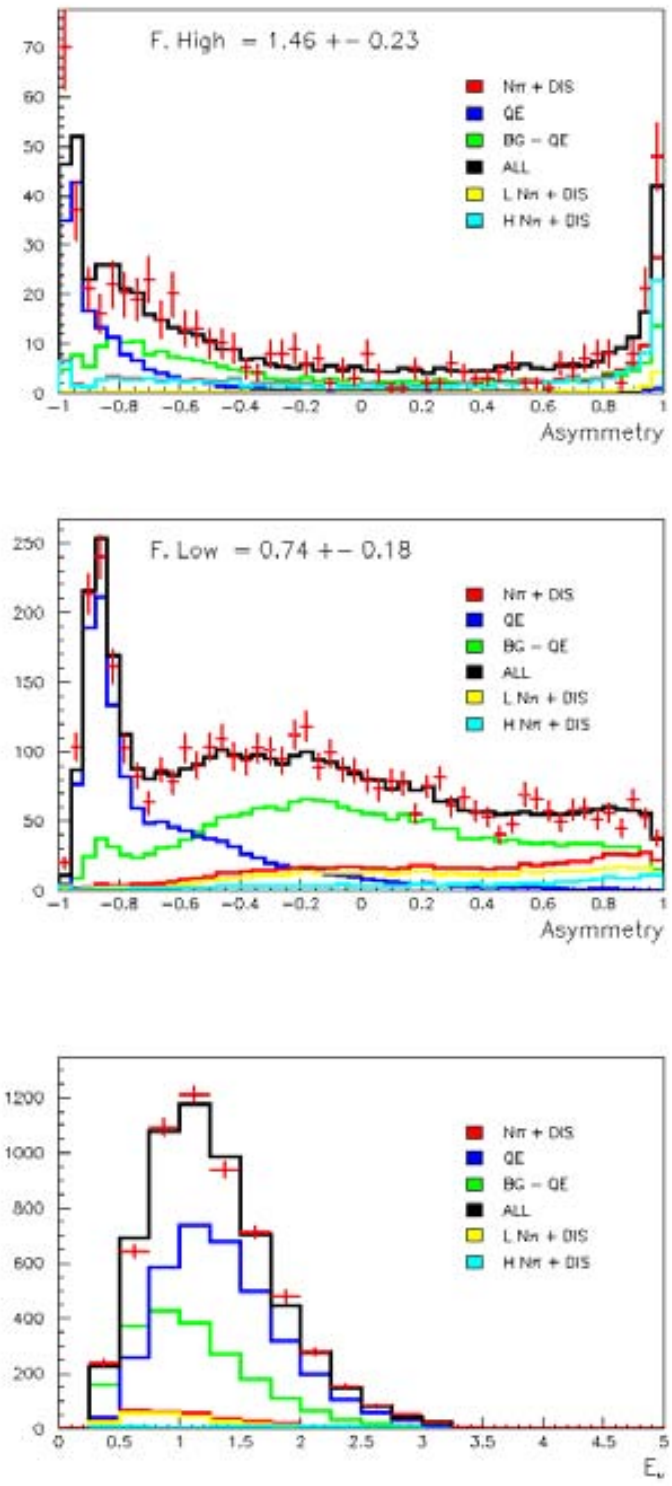

Figure 6.60: $\mathcal{A}_{\text{High}}$ (top), $\mathcal{A}_{\text{Low}}$ (middle) and E_ν^{1T} (bottom) distributions after the fit.

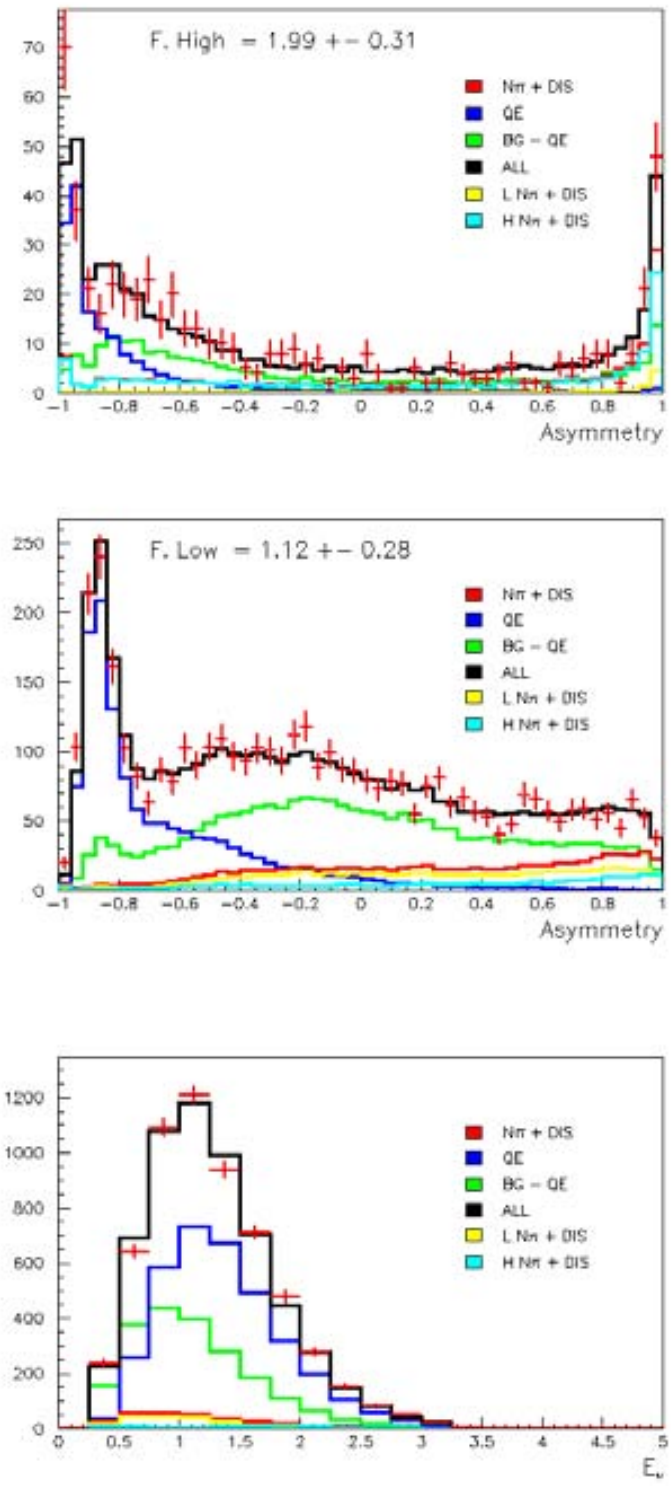

Figure 6.61: $\mathcal{A}_{\mathrm{High}}$ (top), $\mathcal{A}_{\mathrm{Low}}$ (middle) and E_ν^{1T} (bottom) distributions after the fit with Bodek correction.

Chapter 7

Systematic effects

In this chapter the study of systematic effects in the relative cross section measurement is presented and how the related systematic errors have been evaluated.

The systematic effects are grouped into neutrino flux, nuclear, detector and reconstruction effects, depending on the analysis step they are involved in.

In section 7.1 the evaluation method is presented, in sections 7.2 to 7.5 the different systematic effects are explained and in section 7.6 the value of the systematic error associated with each systematic effect is presented as well as the total systematic error and its effect on main distributions.

7.1 Evaluation method

Neutrino flux, nuclear, detector and reconstruction effects has been considered for the study of systematic errors.

Each source of systematic effects is related to a parameter with a high uncertainty. In order to evaluate the systematic error related to each of these parameters, two MC sets has been created for each parameter with $\pm$ one sigma deviation on the related parameter.

To calculate the positive and negative systematic error one repeats the analysis twice for each source of systematic effects, one using the + one sigma modified MC and the other using the - one sigma modified MC. The deviation of the $\sigma_{N\pi}/\sigma_{QE}$ results from the standard value is take as systematic error.

Usually for a systematic source one gets a positive and a negative deviation of $\sigma_{N\pi}/\sigma_{QE}$ and thus a positive and a negative systematic error. But for some systematic sources both deviations go in the same direction, positive or negative, being one of them compatible with the standard value within statistical error. In these cases the MC statistic error is taken as the systematic error for the other direction.

In other words, if one gets that both deviation are positive, then the statistic error is taken as the negative systematic error. On the other hand, if one gets that both

deviation are negative, then the statistic error is taken as the positive systematic error.

In the cases where the systematic parameter affects the data reconstruction process, one generates two data sets with ± one sigma deviation on the related parameter.The evaluation of these systematics are discussed in more detail in section 7.5.

7.2 Neutrino flux effects

As explained in section 3.2, the MC neutrino flux has eight correction factors to fit the real flux. One of them is fixed to one as reference and the other factors were measured in a global fit. One can get the uncertainty and correlations of these factors from table 3.2.

The uncertainty of the neutrino flux at different energies could change the relative amount of the different CC interactions. To evaluate the neutrino flux effects one has unfold the correlation matrix and has applied one sigma variations to each of the seven unfolded variables.

7.3 Nuclear effects

Systematic effects in neutrino interactions calculated with NEUT come from uncertainties in the pion absorption, pion inelastic and proton re-scattering cross section measurements. These nuclear effects can change the momentum and direction of particles in the event, thus changing the observed tracks and energy deposition.

In order to study the systematic effects due to these uncertainties, three modified MC has been created using NEUT vector sets with one standard deviation on the cross section.This variation is ±30% on pion absorbtion and pion inelastic cross section and ±10% on proton re-scattering cross section.

7.4 Detector effects

For detector response simulation SciBar PMT resolution and fiber quenching Birk's factor has been measured. PMT resolution has a ±10% uncertainty and Birks' parameter has a ±11% uncertainty (See chapter 5). These effects can change the amount of reconstructed energy.

SciBar PMT resolution and fiber quenching systematic effects has been studied by applying a one sigma variation on the detector simulation for these parameters.

7.5 Reconstruction effects

In the reconstruction process, several parameters has been used. Hit energy threshold, cross talk parameter, axial mass and p_{scale} has been take into account for the systematic effects evaluation.

Hit energy threshold is fixed experimentally in data to remove low energy noise hits (see Fig. 4.11). But in MC there are less low energy noise hits since the ambiental noise is not simulated. Based on the spread in the distribution of energy calibration constants for each bar the MC hit energy threshold uncertainty is evaluated to be $\pm 15\%$.

The cross talk parameter controls the simulation and reconstruction of the light spread in MAPMT channels neighbour to the central channel. This parameter, used both for MC and data, has an uncertainty of $\pm 7.7\%$ [Whi07]. To evaluate the systematic error due to this effect, two sets of data and MC has been produced with $\pm$ one sigma variation on this parameter. Then the analysis has been repeated with each of these data-MC sets and the deviation of the $\sigma_{N\pi}/\sigma_{QE}$ results from the standard value is taken as the systematic error. In the case that the deviations are both positive or both negative, the statistic error is taken as the systematic error for the other sign.

The axial mass (M_A) is a parameter of the CCQE and CC1π cross sections and has an uncertainty of $\pm 10\%$. To evaluate the systematic error the following reweightings to CCQE and CC1π has been aplyed to reproduce the effect on changing the value of M_A on the neutrino intraction cross section:

$$
\begin{aligned}
\mathcal{F}_{QE}^{+10\%} &= 1.00590 + 2.27484 \times 10^{-1} \cdot Q^2 - 7.16171 \times 10^{-2} \cdot Q^4 \\
\mathcal{F}_{QE}^{-10\%} &= 9.87832 \times 10^{-1} - 2.39031 \times 10^{-1} \cdot Q^2 + 1.00564 \times 10^{-1} \cdot Q^4 \\
\mathcal{F}_{1\pi}^{+10\%} &= 1.233 \cdot \left(0.8445 + 0.5174 \cdot Q^2 - 0.1875 \cdot Q^4\right) / \mathcal{F}_{1\pi}^{\text{std}} \qquad (Q^2 < 2.0 \text{ GeV}^2) \\
&= 1.392 / \mathcal{F}_{1\pi}^{\text{std}} \qquad (Q^2 \geq 2.0 \text{ GeV}^2) \\
\mathcal{F}_{1\pi}^{-10\%} &= 1 / \mathcal{F}_{1\pi}^{\text{std}} \\
\mathcal{F}_{1\pi}^{\text{std}} &= 1.1 \cdot \left(0.9399 + 0.1799 \cdot Q^2 - 0.03654 \cdot Q^4\right) \qquad (Q^2 < 2.0 \text{ GeV}^2) \\
&= 1.2 \qquad (Q^2 \geq 2.0 \text{ GeV}^2)
\end{aligned}
\tag{7.1}
$$

where Q^2 is in GeV^2.

p_{scale} is a factor to fix in data the muon momentum scale. It was measured with a 0.4% uncertainty, but this measurement did not include its dependency on M_A. This linear dependency [ES07] introduces a 1% error because of the M_A uncertainty. Adding quadratically this 1% uncertainty to the 0.4% uncertainty from p_{scale} measurement [A$^+$06] one gets an p_{scale} uncertainty of 1.1%. To evaluate the p_{scale} systematic effect,

the data set has been re-processed changing p_{scale} by $\pm$ 1.1% and the analysis has been repeated, as explained in section 7.1.

7.6 Systematic errors

The overall systematic error has been calculated by adding in quadrature the variations on each sign. This leads to a systematic error of $+0.15\ -0.14$ for $\sigma_{N\pi}/\sigma_{QE}$ Low and $+1.4\ -1.2$ for $\sigma_{N\pi}/\sigma_{QE}$ High. The contribution of each systematic effect is shown in table 7.1.

Source of systematic	**error**			
Sample	**Low E**		**High E**	
Neutrino flux effects				
Flux	0.019	-0.02	0.5	-0.5
Nuclear effects				
Pion absorption	0.06	-0.03	0.2	-0.5
Pion inelastic	0.07	-0.07	0.5	-0.4
Proton re-scattering	0.007	-0.07	0.19	-0.13
Detector effects				
PMT resolution	0.005	-0.006	0.6	-0.3
Quenching	0.07	-0.07	0.09	-0.3
Reconstruction effects				
Hit threshold	0.07	-0.03	0.3	-0.3
Cross talk	0.03	-0.07	0.4	-0.3
Axial mass	0.017	-0.016	0.6	-0.05
p_{scale}	0.05	-0.05	0.5	-0.6
Overall systematic error	**0.15**	**-0.15**	**1.4**	**-1.2**

Table 7.1: Estimation on systematic errors on $\sigma_{N\pi}/\sigma_{QE}$ measurement.

One can check the agreement between data and MC by looking the χ^2 of the basic observables with systematic errors. χ^2 is calculated taking into account the bin correlations for all systematic effects.

The variables used in the likelihood shows a good agreement between data and MC for the low and high energy samples if we take into account the systematic errors (Table 7.2 and figs. 7.1 to 7.13).

Distribution	**Low E**		**High E**	
	χ^2	**d.o.f**	χ^2	**d.o.f**
Number of tracks	1.0	7	3.9	7
Hits energy	18.1	20	16.5	20
Muon Energy	6.2	18	10.7	20
Muon angle	23.0	17	6.5	16
Hadronic energy	13.3	20	25.5	20
$\Delta\theta p$	34.9	20	24.7	20
Total	96.5	102	87.8	103

Table 7.2: Values of χ^2 for all studied distributions after the fit taking into account the systematic errors.

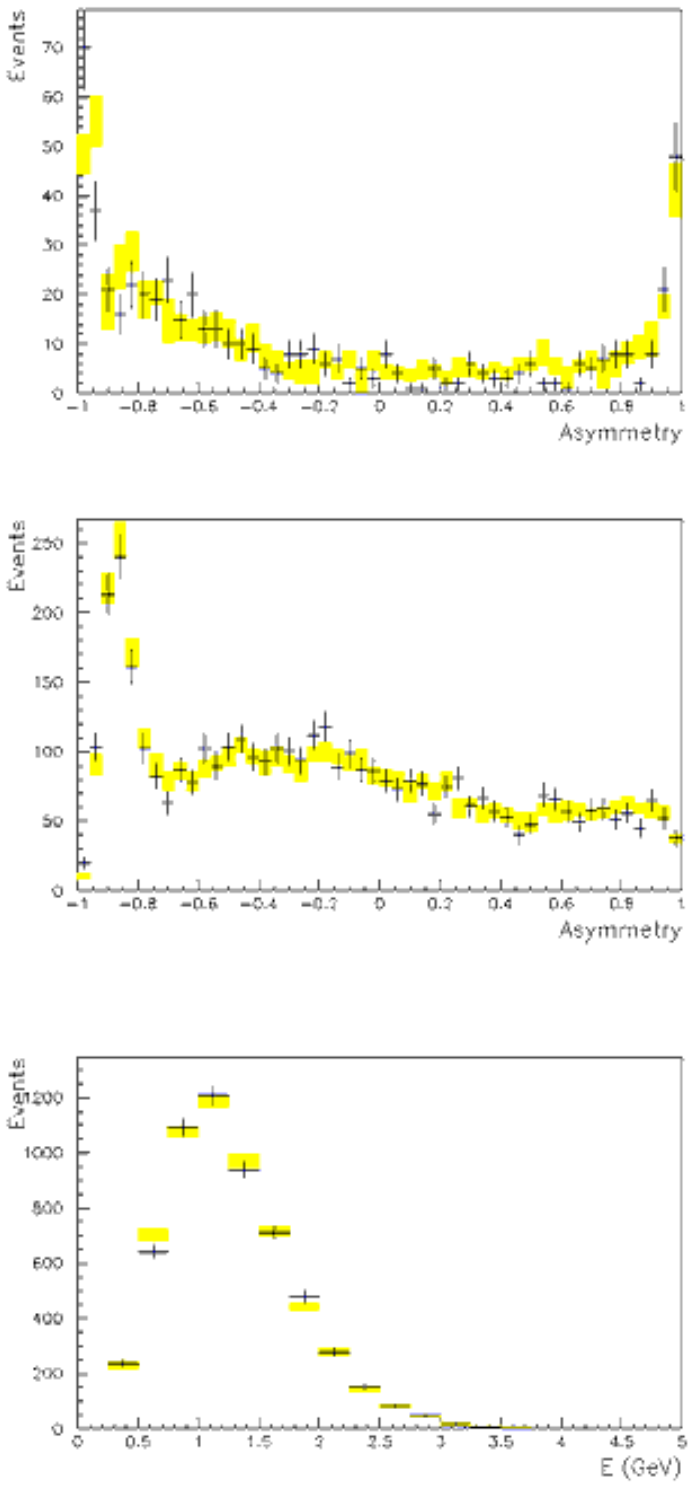

Figure 7.1: $\mathcal{A}_{\text{High}}$ (top), $\mathcal{A}_{\text{Low}}$ (middle) and E_ν^{1T} (bottom) distributions with systematic errors.

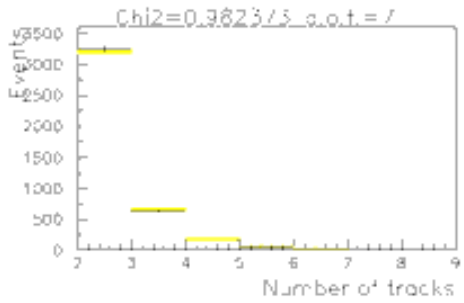

Figure 7.2: Number of tracks for the low E sample with systematic errors.

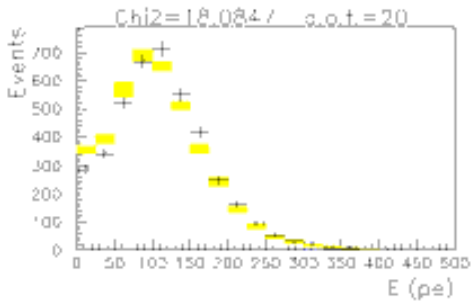

Figure 7.3: Sum of hits energy in the fiducial volume on time with the muon for the low E sample with systematic errors.

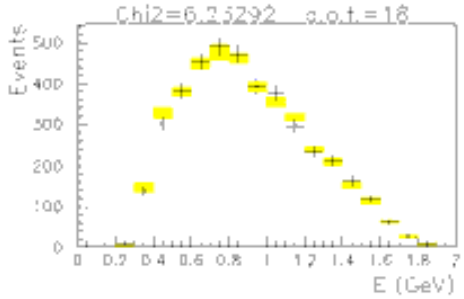

Figure 7.4: Muon energy for the low E sample with systematic errors.

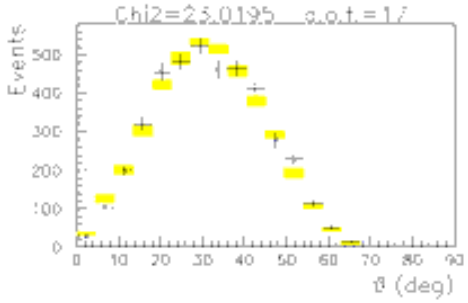

Figure 7.5: Muon angle for the low E sample with systematic errors.

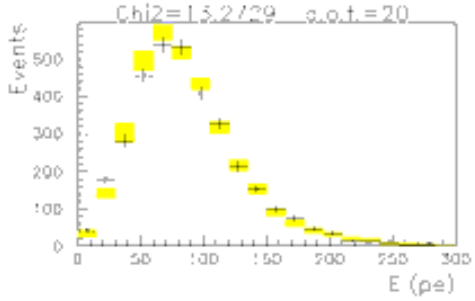

Figure 7.6: Hadronic energy for the low E sample with systematic errors.

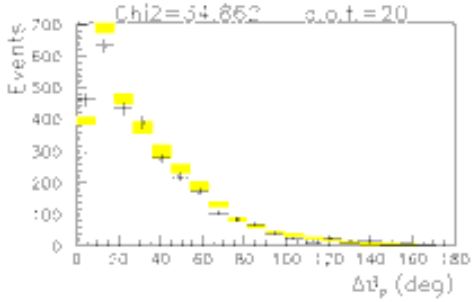

Figure 7.7: Angle between predicted QE proton and longest track with common vertex with the muon for the low E sample with systematic errors.

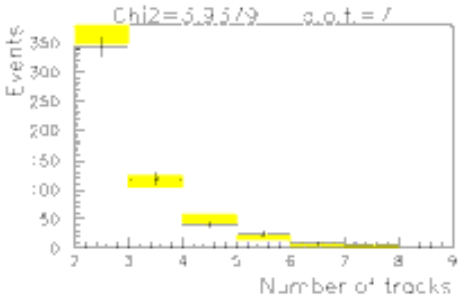

Figure 7.8: Number of tracks for the high E sample with systematic errors.

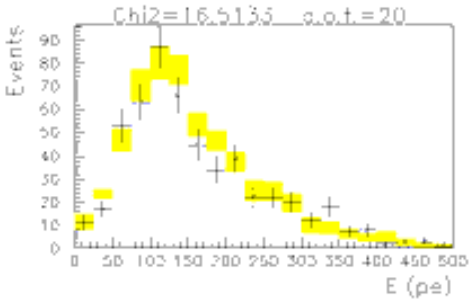

Figure 7.9: Sum of hits energy in the fiducial volume on time with the muon for the high E sample with systematic errors.

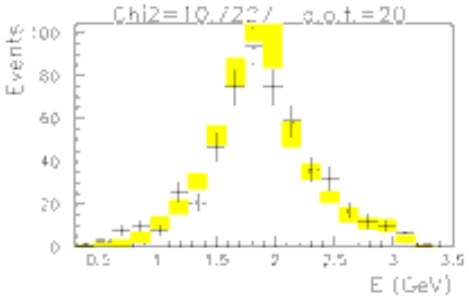

Figure 7.10: Muon energy for the high E sample with systematic errors.

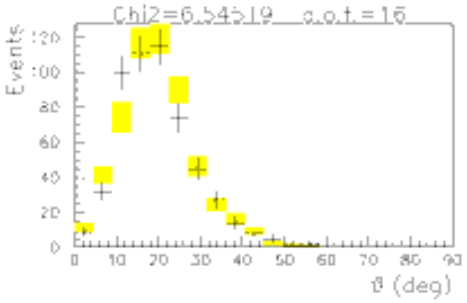

Figure 7.11: Muon angle for the high E sample with systematic errors.

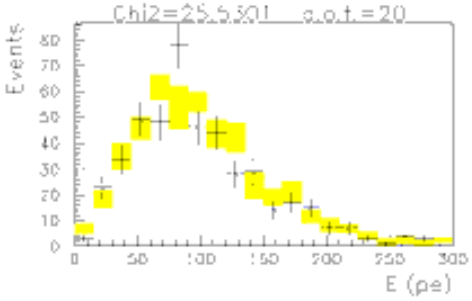

Figure 7.12: Hadronic energy for the high E sample with systematic errors.

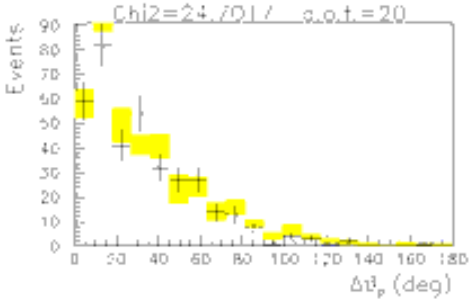

Figure 7.13: Angle between predicted QE proton and longest track with common vertex with the muon for the high E sample with systematic errors.

Chapter 8

Results and conclusions

Following the analysis method explained in chapter 6, the Nπ relative cross section respect to CCQE interactions $\sigma_{N\pi}/\sigma_{QE}$ has been measured for two energy regions. The results with the systematic errors calculated in chapter 7 are quoted in equation 8.1. These two values are 35% correlated. The expected value calculated with NEUT is quoted in equation 8.2 and in figure 8.1 one can compare the measurement result with the expected values.

$$\begin{aligned} \left.\frac{\sigma_{N\pi}}{\sigma_{QE}}\right|_{\text{Low}} &= 0.30 \pm 0.07(\text{stat.})^{+0.15}_{-0.15}(\text{sys.}) \\ \left.\frac{\sigma_{N\pi}}{\sigma_{QE}}\right|_{\text{High}} &= 3.9 \pm 0.6(\text{stat.})^{+1.4}_{-1.2}(\text{sys.}) \end{aligned} \tag{8.1}$$

$$\begin{aligned} \left.\frac{\sigma_{N\pi}}{\sigma_{QE}}\right|^{\text{NEUT}}_{\text{Low}} &= 0.3909 \pm 0.0013(\text{stat.}) \\ \left.\frac{\sigma_{N\pi}}{\sigma_{QE}}\right|^{\text{NEUT}}_{\text{High}} &= 2.57 \pm 0.03(\text{stat.}) \end{aligned} \tag{8.2}$$

In order to compare the result with previous ANL [D^+83] and BNL [K^+86] results some adjustments has been applied. The given multi-pion measurement is relative to CCQE while ANL and BNL results are absolute cross sections. Therefore the $\sigma_{N\pi}/\sigma_{QE}$ result has been multiplied by the mean QE cross section given by Barish [B^+77] for each energy bin.

The results published by ANL are for the two pion production with neutrino interaction on deuterium:

$$\begin{aligned} \nu_\mu d &\rightarrow \mu^-\pi^+\pi^- p p_s \\ \nu_\mu d &\rightarrow \mu^-\pi^+\pi^0 p n_s \\ \nu_\mu d &\rightarrow \mu^-\pi^+\pi^+ n n_s \end{aligned}$$

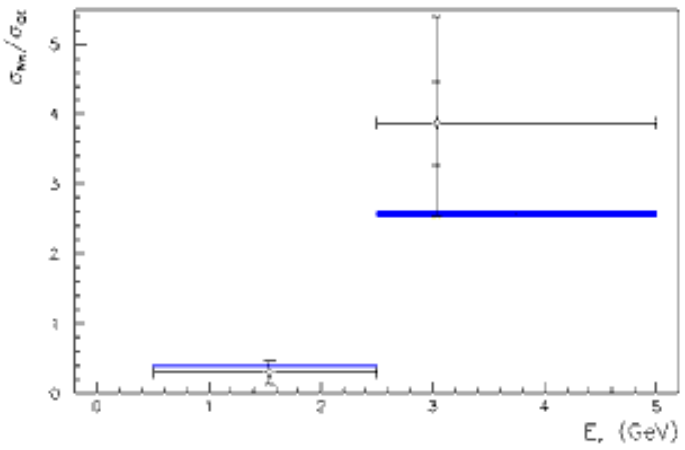

Figure 8.1: Nπ/QE relative cross section. The measurement result is plot in black. The error bars shows the statistic and total error, where the total error is the quadratic sum of the statistical and systematic error. The NEUT results are plot with a blue rectangle which height covers the statistical error.

To compare with our result, the three cross sections has been added. The results published by BNL are for the pion production with neutrino interaction on deuterium:

$$\begin{aligned}
\nu_\mu d &\rightarrow \mu^- \pi^+ \pi^- p p_s \\
\nu_\mu d &\rightarrow \mu^- \pi^+ \pi^+ \pi^- p n_s \\
\nu_\mu d &\rightarrow \mu^- \pi^+ \pi^+ \pi^- \pi^- p p_s \\
\nu_\mu d &\rightarrow \mu^- \pi^+ \pi^+ \pi^+ \pi^- \pi^- p n_s
\end{aligned}$$

and to compare with our result we also add the four cross sections.

Figure 8.2 shows how our results compare with previous ones, once the mentioned adjustments are applied. One can see that, as expected, the given inclusive cross section is higher than the sum of exclusive channel cross sections given by each experiment. At low neutrino energy one gets better agreement since mainly two pions are produced. For higher energies the agreement is worse since only few channels were measured previously with more than two pion. In addition, the results from BNL does not include channels with π^0 and according to the MC more than half of Nπ events have at least one π^0.

Performing the analysis with only one energy bin (see appendix A) we get:

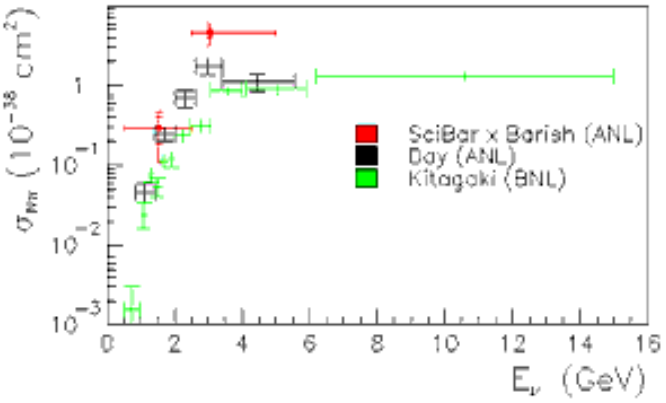

Figure 8.2: Nπ cross section compassion with previous results. Our measurement has been multiplied by the QE cross section gave by Barish *et al* [B$^+$77] and is plotted in black. The cross sections given by ANL [D$^+$83] for two pion production exclusive channels has been added and plotted in red. And the cross sections given by BNL [D$^+$83] for many pion production exclusive channels has been also added and plotted in blue.

$$\left.\frac{\sigma_{N\pi}}{\sigma_{QE}}\right|^{\mathrm{NEUT}} = 0.4486 \pm 0.0014(\mathrm{stat.}) \tag{8.3}$$

$$\frac{\sigma_{N\pi}}{\sigma_{QE}} = 0.48 \pm 0.06(\mathrm{stat.})^{+0.13}_{-0.12}(\mathrm{sys.}) \tag{8.4}$$

This result is close to $\sigma_{N\pi}/\sigma_{QE}$ Low because this sample has more statistics than the measurement of $\sigma_{N\pi}/\sigma_{QE}$ High.

For the measurement, the cross section correction suggested by Bodek [BY02] has not been used to avoid a biased measurement, since the effect of this correction is to reduce low Q^2 Nπ. The measurement shows a good agreement between data and MC without Bodek correction.

In order to cross check the analysis result it has been repeated using the Bodek correction. The result shows that the Nπ reduction produced by the Bodek correction is compensated in the analysis procedure when fitting MC to data. This sugest that in these energy regions one should not use this correction for neutrino Nπ interactions.

Previous K2K measurements used the Bodek correction. K2K measurements to be published as CC single-pion [W$^+$08] also shows that applying Bodek correction the Nπ

cross-section has to be increased by a factor 1.31 ± 0.12 to compensate the reduction produced by the Bodek correction.

Appendix A

Single energy bin analysis

Following a similar method to the one described in the chapters 6 and 7 one can make a $\sigma_{N\pi}/\sigma_{QE}$ measurement for a single neutrino energy bin ranging from 0 to 5 GeV. In this method one do not divide the data sample in high and low neutrino energy sub-samples. But one get the probability distributions $\mathcal{P}_{\text{Full}}$ out of all events in the data sample (Figs. A.1 to A.6).

With these probability distributions one constructs the asymmetry distribution $\mathcal{A}_{\text{Full}}$ (Fig. A.7). One can see that this likelihood also has a good behaviour (Fig. A.8). The CCNπ purity concentrates at high $\mathcal{A}$ values, CCQE at low $\mathcal{A}$ values and CC single pion events at middle $\mathcal{A}$ values.

In the fitting procedure the $\mathcal{A}_{\text{Full}}$ distribution is used for events with more than one track and the neutrino energy distribution is used for one track events. These two distributions are fitted simultaneously. The fit parametrization is the following:

$$\begin{aligned} MC_{RW} &= \text{Norm} \cdot (\text{QE} + f_{\text{N}\pi} \cdot \text{N}\pi + f_{\text{OT}} \cdot \text{Other}) \\ QE &= QE^{+T} + f_{1T/+T} \cdot QE^{1T} \\ N\pi &= N\pi^{+T} + f_{1T/+T} \cdot N\pi^{1T} \\ Other &= OT^{+T} + f_{1T/+T} \cdot OT^{1T} \end{aligned} \tag{A.1}$$

where Norm, $f_{N\pi}$ and f_{OT} and $f_{1T/+T}$ are the fit parameters. X^{1T} names the one track sample and X^{+T} names the sample with more than one track. After the one-track re-weighting, QE is defined as the number of MC CCQE reconstructed events. $N\pi$ is the number of MC signal reconstructed events. *Other* is the number of other MC reconstructed events.

The fitting parameter $f_{1T/+T}$ is applied to the one track sample as a method to propagate the error in tracking efficiencies in that particular sample. This method has been used in several other SciBar analysis and it is kept here also to maintain the compatibility of the results.

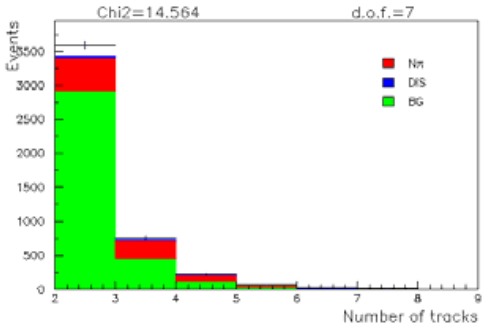

Figure A.1: Number of tracks starting in the fiducial volume for the full sample ($\mathcal{P}_{Ntr}$).

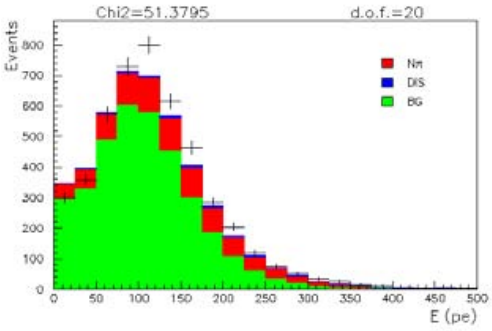

Figure A.2: Sum of hits energy in the fiducial volume on time with the muon for the full sample ($\mathcal{P}_{Ehit}$).

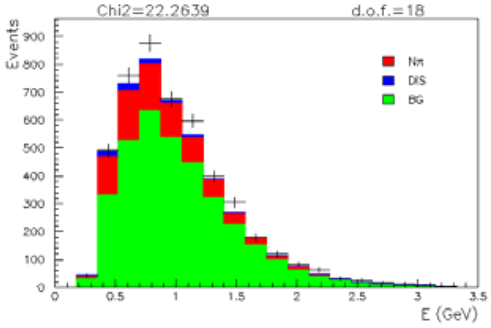

Figure A.3: Muon energy for the full sample ($\mathcal{P}_{E\mu}$).

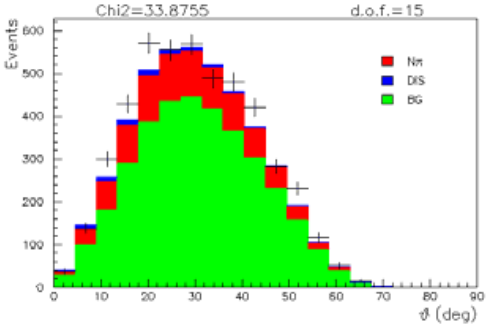

Figure A.4: Muon angle for the full sample ($\mathcal{P}_{\theta\mu}$).

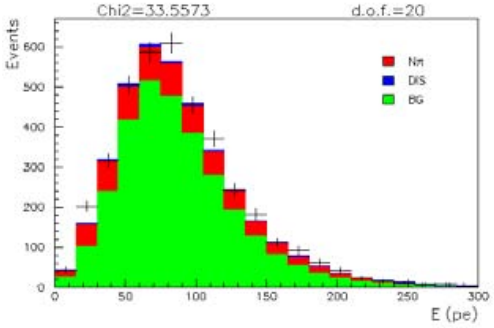

Figure A.5: Hadronic energy for the full sample ($\mathcal{P}_{Ehad}$).

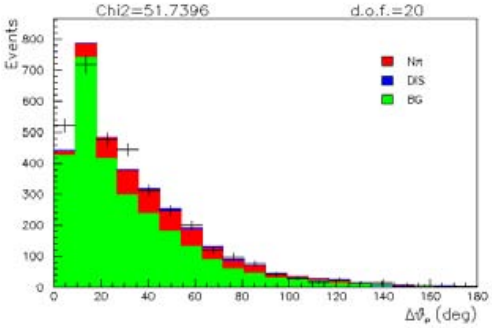

Figure A.6: Angle between predicted QE proton and longest track with common vertex with the muon for the full sample ($\mathcal{P}_{\Delta\theta_p}$).

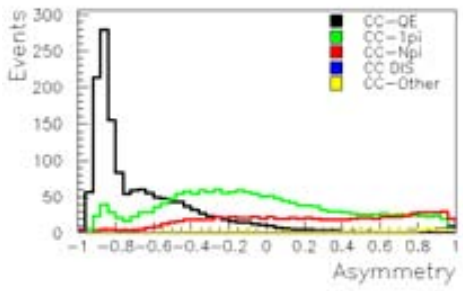

Figure A.7: $\mathcal{A}_{\text{Full}}$ distribution.

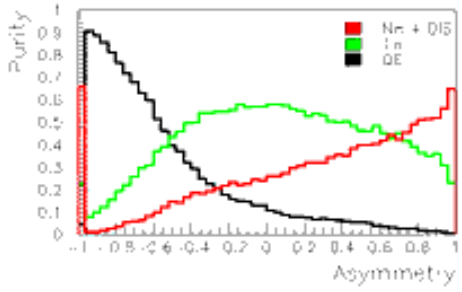

Figure A.8: Main interaction purities in $\mathcal{A}_{\text{Full}}$.

Weighting the MC result (Eq. A.2) with the fit results (Table A.1) as explained in section 6.4 one gets the measurement of the Nπ relative cross section for a single neutrino energy bin (Eq. A.3). The systematic errors summarized in table A.3 are calculated as explained in chapter 7.

$$\left.\frac{\sigma_{N\pi}}{\sigma_{QE}}\right|_{\text{Full}}^{\text{NEUT}} = 0.4486 \pm 0.0014(\text{stat.}) \tag{A.2}$$

$$\left.\frac{\sigma_{N\pi}}{\sigma_{QE}}\right|_{\text{Full}} = 0.48 \pm 0.06(\text{stat.})^{+0.13}_{-0.12}(\text{sys.}) \tag{A.3}$$

Fit factor	**Value**
Norm	0.0262 ± 0.0009
$f_{N\pi}$	1.04 ± 0.12
f_{OT}	1.07 ± 0.09
$f_{1T/+T}$	0.93 ± 0.02

Table A.1: Fit result for one energy bin analysis.

The result of this analysis is in good agreement with the two neutrino energy bin analysis reported in chapter 8. This result is closer to the low neutrino energy result because the high statistics of the low neutrino energy sub-sample.

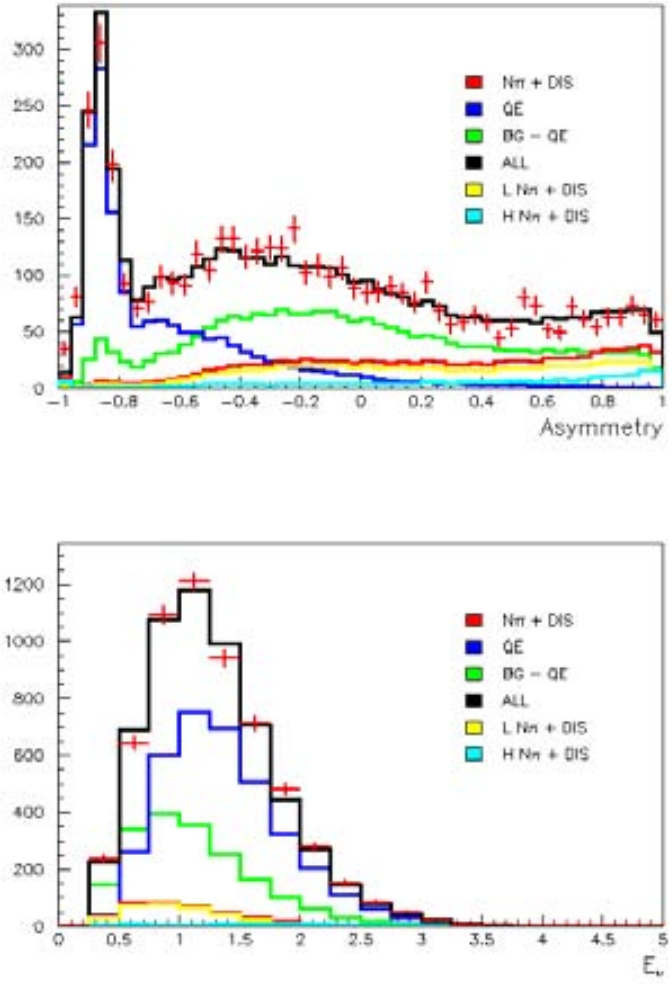

Figure A.9: $\mathcal{A}_{\text{Full}}$ (top) and E_ν^{1T} (bottom) distributions after the fit.

Corr.	$f_{N\pi}$	f_{OT}	$f_{1T/+T}$
Norm	-7%	-66%	-62%
$f_{N\pi}$		-62%	46%
f_{OT}			0.5%

Table A.2: Fit correlation matrix for one energy bin analysis.

Source of systematic	**error**	
Neutrino flux effects		
Flux	0.06	-0.06
Nuclear effects		
Pion absorption	0.05	-0.06
Pion inelastic	0.04	-0.01
Proton re-scattering	0.02	-0.06
Detector effects		
PMT resolution	0.06	-0.03
Quenching	0.05	-0.02
Reconstruction effects		
Hit threshold	0.02	-0.04
Cross talk	0.05	-0.011
Axial mass	0.009	-0.010
p_{scale}	0.0012	-0.008
Overall systematic error	**0.13**	**-0.12**

Table A.3: Estimation on systematic errors on $\sigma_{N\pi}/\sigma_{QE}$ measurement with one energy bin.

Agraïments

I would like to thank my advisor, Dr. Federico Sánchez, for the opportunity to work in this experiment with an excelent team. I am grateful for his advice, constructive discussions and criticism. I thank Prof. Enrique Fernandez for the opportunity to work in a leading research institute as IFAE and for his support and advice.

I would like to take this opportunity to thank all the members of the tribunal, who kindly accepted the revision of this work: professors Alain Blondel, Josep Antoni Grifols Gras, Michel Sorel, Juan M. Nieves Pamplona, Martine Bosman, Ramon Miquel Pascual and Mª Pilar Casado Lechuga.

I would like to thank the K2K Collaboration and especially everyone in the K2K-SciBar group. I thank Prof. Chang Kee Jung for his wise advices and the talks we had at Bercelona. I want to thank Dr. Tsuyoshi Nakaya, Dr. Masashi Yokoyama, Dr. Lucio Ludovici, Dr. Federico Sanchez, and Dr. Michel Sorel for their excellent leadership of the SciBar group. I also want to thank Dr. Yoshinari Hayato for all the NEUT vectors he provide to produce the different simulations needed in this analysis. I very appreciate the help of Lisa Whitehead in fixing the MC and data reconstruction used in this analysis.

I would like to thank the SciBooNE Collaboration. I thank Dr. Morgan Wascko and Dr. Tsuyoshi Nakaya for the great SciBooNE Social Club and their excellent leadership. I also want to thank Dr. Rick J. Tesarek and Dr. Robert A. Napora for they great managing. I specially thank Jose Luis Alcaraz Aunión and Joan Català Pérez for the great time we share at Fermilab and highly intense and effective team work we made.

Quiero agradecer especialmente toda la ayuda y apoyo que he recibido del grupo de neutrinos en el IFAE. Como he mencionado al principio, agradezco a Federico Sánchez Nieto su apoyo, consejo y discusión constructiva a lo largo de la tesis. Agradezco a Enrique Fernández Sánchez su apoyo y consejo. También doy las gracias a Xavi Espinal por su apoyo y por esas salidas de escalada, a Sofia Andringa por sus discusiones constructivas y sus esplicaciones, a Federico Nova por su su creatividad y su colaboración en incontables tareas, a Thorsten Lux por su ayuda en la corrección de la tesis y de forma muy especial quiero dar las gracias a Ana-Yaiza Rodríguez Marrero por su apoyo en todo momento, por su inestimable ayuda en todo el trabajo que he realizado en el IFAE y por lo maravillosa compañera que ha sido todos estos años. Ha sido un privilegio trabajar con todos ellos.

También ha sido un placer ir a comer durante estos años con Núria, Ana, Enol,

Carlos, Ester, Laia, Sígrid, Manel, Roger . . . charlar en la puerta de atrás del IFAE con Jaume, Josevi, Otger, Miquel, Pepe y Álex, ir a escalar con Xavi, Ester y Germano o ir a cenar en el "On the borders" con Paul, Jose y Joan. Por esos momentos tan agradables, gracias a todos.

I per últim però no per això menys important, vull agrair a Núria la meua dona, als meus pares Toni i Piedad, a la meua germana Clara i a la meua extensa família tota l'ajuda que m'han prestat, els ànims que m'han donat en tot moment i tot el seu amor sense els quals no hagera pogut fer aquesta tesis. Us vull molt!!.

Gabriel V. Jover Mañas

List of Figures

List of Tables

Bibliography

[A+81] D. Ashery et al. True absorption and scattering of pions on nuclei. *Phys. Rev.*, C23:2173–2185, 1981.

[A+02] Q. R. Ahmad et al. Direct evidence for neutrino flavor transformation from neutral-current interactions in the Sudbury Neutrino Observatory. *Phys. Rev. Lett.*, 89:011301, 2002.

[A+04a] S. N. Ahmed et al. Measurement of the total active B-8 solar neutrino flux at the Sudbury Neutrino Observatory with enhanced neutral current sensitivity. *Phys. Rev. Lett.*, 92:181301, 2004.

[A+04b] Y. Ashie et al. Evidence for an oscillatory signature in atmospheric neutrino oscillation. *Phys. Rev. Lett.*, 93:101801, 2004.

[A+05] Y. Ashie et al. A measurement of atmospheric neutrino oscillation parameters by super-kamiokande i. *Phys. Rev.*, D71:112005, 2005.

[A+06] M. H. Ahn et al. Measurement of neutrino oscillation by the k2k experiment. *Phys. Rev.*, D74:072003, 2006.

[AJ75] Carl H. Albright and C. Jarlskog. Neutrino production of m+ and e+ heavy leptons. 1. *Nucl. Phys.*, B84:467, 1975.

[B+77] S. J. Barish et al. Study of Neutrino Interactions in Hydrogen and Deuterium. 1. Description of the Experiment and Study of the Reaction Neutrino d → mu- p p(s). *Phys. Rev.*, D16:3103, 1977.

[Ber72] H. W. Bertini. Nonelastic interactions of nucleons and pi mesons with complex nuclei at energies below 3 gev. *Phys. Rev.*, C6:631–659, 1972.

[Bro99] Michael Browne. *Preparation for Deployment of the Neutral Current Detectors (NCDs) for the Sudbury Neutrino Observatory.* PhD thesis, North Carolina State University, 1999.

[BY02] A. Bodek and U. K. Yang. Modeling deep inelastic cross sections in the few gev region. *Nucl. Phys. Proc. Suppl.*, 112:70–76, 2002.

[C+71] Y. Cho et al. Pion production in proton-beryllium collisions at 12.4 gev/c. *Phys. Rev.*, D4:1967–1974, 1971.

[C+06] M. G. Catanesi et al. Measurement of the production cross-section of positive pions in p al collisions at 12.9-gev/c. *Nucl. Phys.*, B732:1–45, 2006.

[CRH+56] Jr. Cowan, C. L., F. Reines, F. B. Harrison, H. W. Kruse, and A. D. McGuire. Detection of the free neutrino: a confirmation. *Science*, 124(3212):103–104, 1956.

[D+62] G. Danby et al. Observation of high-energy neutrino reactions and the existence of two kinds of neutrinos. *Phys. Rev. Lett.*, 9:36–44, 1962.

[D+83] D. Day et al. STUDY OF neutrino D CHARGED CURRENT TWO PION PRODUCTION IN THE THRESHOLD REGION. *Phys. Rev.*, D28:2714–2720, 1983.

[D+89] D. Decamp et al. Determination of the Number of Light Neutrino Species. *Phys. Lett.*, B231:519, 1989.

[DHH68] Jr. Davis, Raymond, Don S. Harmer, and Kenneth C. Hoffman. Search for neutrinos from the sun. *Phys. Rev. Lett.*, 20:1205–1209, 1968.

[E+97] E. Eskut et al. The CHORUS experiment to search for nu/mu –¿ nu/tau oscillation. *Nucl. Instrum. Meth.*, A401:7–44, 1997.

[ES07] X. Espinal and F. Sánchez. Measurement of the axial vector mass in neutrino-carbon interactions at k2k. In Geralyn P. Zeller, Jorge G. Morfin, and Flavio Cavanna, editors, *NEUTRINO-NUCLEUS INTERACTIONS IN THE FEW-GEV REGION: NuInt07: The 5th International Workshop on Neutrino-Nucleus Interactions in the Few-GeV Region*, volume 967, pages 117–122. AIP, 2007.

[F+98] Y. Fukuda et al. Evidence for oscillation of atmospheric neutrinos. *Phys. Rev. Lett.*, 81:1562–1567, 1998.

[GD94] Computing GEANT, Application Software Group and Networks Division. *Detector Description and Simulation Tool*, volume CERN Program Libray Long Writeup W5013. CERN, CH-1211 Geneva 23, Switzerland, 1994.

[GP69] V. N. Gribov and B. Pontecorvo. Neutrino astronomy and lepton charge. *Phys. Lett.*, B28:493, 1969.

[GRV95] M. Gluck, E. Reya, and A. Vogt. Dynamical parton distributions of the proton and small x physics. *Z. Phys.*, C67:433–448, 1995.

[H+88] K. S. Hirata et al. Experimental Study of the Atmospheric Neutrino Flux. *Phys. Lett.*, B205:416, 1988.

[H+89] K. S. Hirata et al. Observation of B-8 Solar Neutrinos in the Kamiokande-II Detector. *Phys. Rev. Lett.*, 63:16, 1989.

[H+05] M. Hasegawa et al. Search for coherent charged pion production in neutrino carbon interactions. *Phys. Rev. Lett.*, 95:252301, 2005.

[HARW92] J. S. Hyslop, R. A. Arndt, L. D. Roper, and R. L. Workman. Partial wave analysis of k+ nucleon scattering. *Phys. Rev.*, D46:961–969, 1992.

[Has06] Masaya Hasegawa. *Measurement of Neutrino Oscillation Parameters with Neutrino-Nucleus Interaction Studies in the K2K Experiment.* PhD thesis, Kyoto University, January 2006.

[Hay02] Y. Hayato. Neut. *Nucl. Phys. Proc. Suppl.*, 112:171–176, 2002.

[I+02] T. Ishii et al. Near muon range detector for the k2k experiment: Construction and performance. *Nucl. Instrum. Meth.*, A482:244–253, 2002.

[K+86] T. Kitagaki et al. CHARGED CURRENT EXCLUSIVE PION PRODUCTION IN NEUTRINO DEUTERIUM INTERACTIONS. *Phys. Rev.*, D34:2554–2565, 1986.

[K+05] Ch. Kraus et al. Final results from phase ii of the mainz neutrino mass search in tritium beta decay. *Eur. Phys. J.*, C40:447–468, 2005.

[KLLW81] Jihn E. Kim, Paul Langacker, M. Levine, and H. H. Williams. A theoretical and experimental review of the weak neutral current: A determination of its structure and limits on deviations from the minimal su(2)-l x u(1) electroweak theory. *Rev. Mod. Phys.*, 53:211, 1981.

[LS57] S. J. Lindenbaum and R. M. Sternheimer. Isobaric nucleon model for pion production in nucleon- nucleon collisions. *Phys. Rev.*, 105:1874–1879, 1957.

[LS72] C. H. Llewellyn Smith. Neutrino reactions at accelerator energies. *Phys. Rept.*, 3:261, 1972.

[MDE00] J. Marteau, J. Delorme, and Magda Ericson. Nuclear effects in neutrino nucleus interactions. *Nucl. Instrum. Meth.*, A451:76–80, 2000.

[MP77a] B. R. Martin and M. K. Pidcock. Anti-k n interactions in the resonance region. 1. analysis of data. *Nucl. Phys.*, B126:266, 1977.

[MP77b] B. R. Martin and M. K. Pidcock. Anti-k n interactions in the resonance region. 2. amplitudes. *Nucl. Phys.*, B126:285, 1977.

[MV78] P. Musset and J. P. Vialle. Neutrino physics with gargamelle. *Phys. Rept.*, 39:1–130, 1978.

[N+86] Masayuki Nakahata et al. Atmospheric neutrino background and pion nuclear effect for kamioka nucleon decay experiment. *J. Phys. Soc. Jap.*, 55:3786, 1986.

[N+04] K. Nitta et al. The k2k scibar detector. *Nucl. Instrum. Meth.*, A535:147–151, 2004.

[RC59] F. Reines and C. L. Cowan. Free anti-neutrino absorption cross-section. 1: Measurement of the free anti-neutrino absorption cross-section by protons. *Phys. Rev.*, 113:273, 1959.

[Rei87] D. Rein. Angular distribution in neutrino induced single pion production processes. *Z. Phys.*, C35:43–64, 1987.

[RS81] Dieter Rein and Lalit M. Sehgal. Neutrino excitation of baryon resonances and single pion production. *Ann. Phys.*, 133:79, 1981.

[RSL78] Glenn Rowe, Martin Salomon, and Rubin H. Landau. Energy-dependent phase shift analysis of pion-nucleon scattering below 400 mev. *Phys. Rev. C*, 18(1):584–589, Jul 1978.

[S+00] A. Suzuki et al. Design, construction, and operation of scifi tracking detector for k2k experiment. *Nucl. Instrum. Meth.*, A453:165–176, 2000.

[Sjo94] Torbjorn Sjostrand. High-energy physics event generation with pythia 5.7 and jetset 7.4. *Comput. Phys. Commun.*, 82:74–90, 1994.

[SM72] R. A. Smith and E. J. Moniz. Neutrino reactions on nuclear targets. *Nucl. Phys.*, B43:605, 1972.

[SOVVGR88] L. L. Salcedo, E. Oset, M. J. Vicente-Vacas, and C. Garcia-Recio. Computer simulation of inclusive pion nuclear reactions. *Nucl. Phys.*, A484:557, 1988.

[Spa84] David A. Sparrow. Effects of the nuclear medium on the observation of baryon number violation. In Richard E. Mischke, editor, *Intersections between particle and nuclear physics (Steamboat Springs, 1984) : proceedings*, volume 123 of *AIP Conference Proceedings*, pages 1019–1025. American Institute of Physics, 1984.

[W+08] Lisa A. Whitehead et al. Measurement of the single charged pion production in charged-current neutrino-carbon interactions at the k2k experiment. Paper in preparation., 2008.

[Whi07] Lisa Angelika Whitehead. *Measurement of the Single Charged Pion Production Cross Section in Charged-Current Neutrino-Carbon Interactions*. PhD thesis, Stony Brook University, May 2007.

[Win91] K. Winter, editor. *Neutrino physics*. Cambridge monographs on particle physics, nuclear physics, and cosmology. Cambridge University Press, Cambridge, 1991.

[WS54] Roger D. Woods and David S. Saxon. Diffuse surface optical model for nucleon-nuclei scattering. *Phys. Rev.*, 95(2):577–578, Jul 1954.

[Y+97] Y. Yamanoi et al. Large horn magnets at the kek neutrino beam line. *KEK-PREPRINT*, 97-225, 1997.

[Y+99] Y. Yamanoi et al. Large horn magnets at the kek neutrino beam line. ii. *KEK-PREPRINT*, 99-178, 1999. Prepared for 16th International Conference on Magnet Technology (MT-16 1999), Tallahassee, Florida, 29 Sep - 1 Oct 1999.

[Y+04] M. Yoshida et al. Development of the readout system for the k2k scibar detector. *IEEE Trans. Nucl. Sci.*, 51:3043–3046, 2004.

[Y+05] S. Yamamoto et al. Design, construction, and initial performance of scibar detector in k2k experiment. *IEEE Trans. Nucl. Sci.*, 52:2992–2997, 2005.

[ZG94] C. Zeitnitz and T. A. Gabriel. The GEANT - CALOR interface and benchmark calculations of ZEUS test calorimeters. *Nucl. Instrum. Meth.*, A349:106–111, 1994.